

**STUDY OF SIMPLIFIED MODELS OF AIRCRAFT  
STRUCTURES SUBJECTED TO GENERALIZED  
EXPLOSIVE LOADING**

**BY JASON R. FLOREK**

A dissertation submitted to the  
Graduate School—New Brunswick  
Rutgers, The State University of New Jersey  
in partial fulfillment of the requirements  
for the degree of  
Doctor of Philosophy  
Graduate Program in Mechanical and Aerospace Engineering

Written under the direction of

Dr. Haym Benaroya

and approved by

---

---

---

---

New Brunswick, New Jersey

October, 2007

© 2007

Jason R. Florek

**ALL RIGHTS RESERVED**

## **ABSTRACT OF THE DISSERTATION**

# **Study of Simplified Models of Aircraft Structures Subjected to Generalized Explosive Loading**

**by Jason R. Florek**

**Dissertation Director: Dr. Haym Benaroya**

This dissertation develops a simple methodology for estimating the maximum elastic-plastic deformation of thin, rectangular plates due to an exponentially decaying pressure pulse. Initially, only small plates, representative of aircraft skin panels, and uniformly distributed pressures are examined. The deflections predicted by this procedure are compared with those attained from finite element analysis for various plate dimensions and blast intensities. Material properties and boundary conditions are also varied. It is found that the current, clamped single-degree-of-freedom model is generally a much better predictor of deflection than its simply supported counterpart, although both show average errors of less than 15% compared to finite element results. The deviations between all of the models tend to decrease as surface area decreases, or as plate thickness and aspect ratio increase. A means of approximating permanent plate deflection is also suggested, which favorably compares with previously published experimental results for square, aluminum plates.

The aforementioned procedure is then extended for use with larger geometries, namely a wider fuselage section and a panel of an onboard luggage container, and nonuniform pressures. A generalized distribution function is developed to account for nonuniformities consistent with detonations at a small standoff distance. Moreover, two normalized criteria are proposed to determine when these nonuniformities can be ignored. In addition, large

discrepancies are found in calculated deflections when incorporating the current structural model and the blast parameter data from two commonly used sources for both uniform and nonuniform loading cases. As a result, uncertainties in these data are thoroughly examined, which leads to confidence bounds being placed on all calculated deflections through a Monte Carlo scheme. This, in turn, allows for the generation of probability of failure curves.

Suggestions for improving the current loading and structural models are also discussed. Finally, the method of analysis for plates is preliminarily extended for the blast loading of thin, cylindrical shells. The various topics covered and simplified models proposed are useful to both the experimentalist and designer of blast resistant structures.

## Acknowledgements

First and foremost, I acknowledge my research advisor Dr. Haym Benaroya. Professor, thank you for all that you've done for me. I have learned so much and truly enjoyed my time here at Rutgers, both in no small part due to you. Having shared my graduate experience with numerous students across many departments, I realize just how fortunate I've been to have you as an advisor. Sure, the office itself is nice, but the learning atmosphere inside is even better (more on my fellow csXers to follow). Thank you for your great patience and the liberties you've afforded me over the years to take my research in the current direction. I do not believe I could have thrived so readily in another situation. And I will certainly heed your parting advice, and not mess with Texas.

I sincerely thank the Transportation Security Administration and Department of Homeland Security for their funding of this research and my graduate study for the last five years. In particular, I thank Howard Fleisher and Nelson Carey of the Transportation Security Laboratory for their support and interest. I am especially appreciative of their allowing me the opportunity last year to witness aircraft blast testing firsthand. Nelson and his former TSL colleague Joe Gatto were extremely helpful in answering questions during that trip to Aberdeen. I further thank Joe for his insights into blast scaling, which have greatly influenced the current work. Additionally, I thank my future employer Quentin Baker for his explanations of blast wave phenomena.

Furthermore, I acknowledge the Department of Mechanical and Aerospace Engineering at Rutgers University. Specifically, I thank Dr. Haim Baruh, whom I've known for nearly nine years now. Like Professor Benaroya, you have always shown great confidence in me, for which I am truly grateful. It really dates back to my days in your undergraduate Dynamics class, and has continued throughout your stays as graduate director, soccer teammate and dissertation committee member. As a result, I may come back to Rutgers once again to

pursue that elusive M.P.S. degree.

In addition, I thank Dr. Abelfattah Zebib for all of his assistance during my fellowship. I also acknowledge Drs. Ellis Dill and Alberto Cuitiño, both whom I've had multiple graduate courses under and approved my master's work. Dr. Dill has discussed with me at great length the merits of finite element modeling and given me insight into the issues discussed in Section 6.1. Moreover, Professor Cuitiño served on my dissertation defense committee, along with Dr. Nenad Gucunski from Civil Engineering. I appreciate the useful comments and suggestions each has given in this capacity.

I acknowledge all members past and present of the Center for Structures in eXtreme in Environments (csXe). With regard to my research, I especially thank Dr. Yuriy Gulak and soon-to-be (STB) Master Elan Borenstein. Yuriy, your help over the last three years has been invaluable. I am always amazed by the fact that you have technical expertise in just about every subject imaginable, whether it's fluid dynamics, stock market modeling or table-top hockey. Palooza! Elan, even though I'm the one with the fancy degree, more often than not, you're the one answering my questions. Go figure. Good luck with your blast related research and, more importantly, with the department soccer team (more on my fellow MAE United members to follow). I also thank Drs. Rene David Gabbai and Pravin Subramanian, STB Dr. Subramanian Ramakrishnan, STB Master Paola Jaramillo and Nir Pony for their comradery during my stay in D150. Moreover, Trisha Mazzuco has been very helpful in keeping the center going on a day-to-day basis.

Furthermore, I acknowledge all of those individuals involved with my extracurricular activities at Rutgers. This includes members past and present of the MAE United Soccer Club. Before two and half years ago, I had never played soccer. Thanks to all of you, I've improved from a novice to a below average goalkeeper. This transition could not be possible without the tutelage of Coach Borenstein and my various defensemen, most notably Dr. Lucian Iorga and STB Dr. Pedro Romero, who have been good friends since my first semester of graduate studies. I also thank the Marita's Cantina crew—Elan, Paola, Dr. Carlos Correa, STB Dr. Maria Velez and, more recently, Tushar Saraf for their friendship and shared interest in quarter chicken wings and mango chango. You all justified (at least once a week) my regularly being at the office past 10pm. Special thanks to fellow night

owls Brigham, Stuart and Iago for their help in typesetting this dissertation.

Finally, I thank my family for their encouragement and support throughout the years. In particular, I thank my Aunt Christy, who, for as long as I can remember, wanted me to become a brain surgeon. I hope just being a doctor is enough. I also acknowledge my Uncle Rick for calling me "Dr. Jay" for the last few years, even though it wasn't official. Moreover, I am indebted to my brothers John C. and Steven for, amongst other things, letting me play baseball with them since I was in diapers. I am even more grateful to my parents John H. and Christine for their unending faith in me. I appreciate all that you've sacrificed over the years. Mom and Steve, in my master's thesis acknowledgements, I wrote that "you two are my life." That hasn't changed, but I suppose there's room for one more. With that, I sincerely thank my sweet Paola for her love and support. You've definitely made my life a lot more interesting.

## Dedication

To my mother, Christine Ann Florek, a true angel amongst men. Matka, co wola twój dziecko czynić rezygnować ty?

# Table of Contents

<b>Abstract</b> . . . . .	ii
<b>Acknowledgements</b> . . . . .	iv
<b>Dedication</b> . . . . .	vii
<b>List of Tables</b> . . . . .	xii
<b>List of Figures</b> . . . . .	xiii
<b>1. Introduction</b> . . . . .	1
1.1. Dissertation Motivation . . . . .	1
1.2. Dissertation Contribution . . . . .	3
1.3. Dissertation Outline . . . . .	5
<b>2. Typical Explosive Loading Model</b> . . . . .	7
2.1. Side-On Blast Parameters . . . . .	8
2.2. Blast Scaling . . . . .	10
2.3. Simplified Parameter Relationships . . . . .	13
2.4. Reflected Blast Parameters . . . . .	18
2.5. Uniform Loading . . . . .	21
<b>3. Validation of Structural Model for Uniform Pressure Load</b> . . . . .	23
3.1. Elastic Phase Structural Model . . . . .	25
3.1.1. General Governing Equations . . . . .	25
3.1.2. Simply Supported Plate . . . . .	25
3.1.3. Clamped Plate . . . . .	28
3.1.4. Yield Condition . . . . .	29

3.2.	Plastic Phase Structural Model . . . . .	30
3.2.1.	Plate Displacements and Angular Velocities . . . . .	31
3.2.2.	Energy Relationships . . . . .	32
3.2.3.	Failure Criterion . . . . .	34
3.2.4.	Permanent Deformation . . . . .	35
3.3.	Numerical Procedure . . . . .	36
3.3.1.	Timestepping Scheme . . . . .	36
3.3.2.	Geometry and Material Properties . . . . .	37
3.3.3.	Pressure Loading . . . . .	38
3.4.	Validation with Finite Element Analysis . . . . .	39
3.4.1.	Simply Supported Plate . . . . .	39
3.4.2.	Clamped Plate . . . . .	42
3.4.3.	Permanent Deformation . . . . .	47
3.5.	Validation with Experimental Results . . . . .	48
<b>4.</b>	<b>Improvements to Explosive Loading Model . . . . .</b>	<b>52</b>
4.1.	Nonuniform Reflection . . . . .	53
4.1.1.	Pressure Distribution . . . . .	53
4.1.2.	Impulse Distribution . . . . .	57
4.1.3.	Normalized Criteria for Assessing Applicability of Uniform Pressure Distribution . . . . .	60
4.2.	Specialized Effects . . . . .	62
4.2.1.	Negative Pressure Phase . . . . .	62
4.2.2.	Pressure Relief . . . . .	63
4.2.3.	TNT Equivalence . . . . .	64
4.3.	Problems with Blast Scaling . . . . .	66
4.3.1.	Variety of Scaled Distances . . . . .	66
4.3.2.	Side-On Blast Parameters . . . . .	67
4.3.3.	Reflected Blast Parameters . . . . .	70

4.4.	Determination of Generalized Pressure Distribution . . . . .	73
<b>5.</b>	<b>Structural Response to Nonuniform Pressure Load . . . . .</b>	<b>78</b>
5.1.	Method of Analysis . . . . .	78
5.1.1.	Structural Model and Timestepping Scheme . . . . .	78
5.1.2.	Geometry and Material Properties . . . . .	79
5.1.3.	Pressure Loading . . . . .	81
5.2.	Comparison of Response to Uniform and Nonuniform Deterministic Load . . . . .	83
5.2.1.	Results of Deterministic Trials . . . . .	83
5.2.2.	Evaluation of Normalized Criteria . . . . .	88
5.3.	Response to Nonuniform Random Load . . . . .	91
5.3.1.	Monte Carlo Method . . . . .	91
5.3.2.	Results of Random Trials . . . . .	93
5.3.3.	Probability of Failure . . . . .	94
<b>6.</b>	<b>Improvements to Structural Model . . . . .</b>	<b>97</b>
6.1.	Elastic Phase Structural Model . . . . .	97
6.1.1.	Adding Terms to Fourier Series Expansion . . . . .	97
6.1.2.	Changing Exponent of Assumed Clamped Deflection Shape . . . . .	100
6.2.	Plastic Phase Structural Model . . . . .	103
6.2.1.	Plate Displacements and Angular Velocities for Box Shaped Pattern . . . . .	103
6.2.2.	Energy Relationships for Box Shaped Pattern . . . . .	105
6.2.3.	Additional Equations of Motion for Boxed Shaped Pattern . . . . .	107
6.2.4.	Smoothing Transition at Yielding . . . . .	110
6.2.5.	Permanent Deformation via Damping . . . . .	113
6.3.	Extension of Current Model to Shells . . . . .	113
6.3.1.	Elastic Phase Shell Model . . . . .	114
6.3.2.	Yield Condition of Hinged Shell . . . . .	116
6.3.3.	Plastic Phase Shell Model . . . . .	118

<b>7. Conclusions and Future Work</b> . . . . .	119
7.1. Conclusions . . . . .	119
7.2. Future Work . . . . .	120
<b>Appendix A. Sample Matlab Program</b> . . . . .	122
<b>Appendix B. Sample ANSYS Program</b> . . . . .	130
<b>Appendix C. Details of Box Shaped Deformation Pattern</b> . . . . .	138
C.1. Definition of Modifying Factors . . . . .	138
C.2. Calculation of Initial Values for $\delta$ and $\xi$ . . . . .	139
<b>References</b> . . . . .	141
<b>Vita</b> . . . . .	148

## List of Tables

3.1. Dimensional case definitions with deflections at rupture. . . . .	35
3.2. Blast parameters as a function of scaled distance $Z$ . . . . .	39
3.3. Permanent deflection parameters for a clamped $150 \times 100$ mm plate. . . . .	48
3.4. Comparison of dynamic maximum and permanent deflections for a $500 \times 500 \times 1$ mm plate. . . . .	49
4.1. TNT equivalency factors for common explosives from various sources. . . . .	65
4.2. Impulse comparison for various assumed pressure profiles, charge sizes and standoffs. . . . .	75
5.1. Correction factors to better match Matlab and ANSYS results. . . . .	81
5.2. Comparison of maximum deflection and normalized criterion values for SC/LP case. . . . .	89
5.3. Comparison of maximum deflection and normalized criterion values for LC/LP case. . . . .	90

## List of Figures

2.1. Typical blast wave pressure-time history with parameter definitions. . . . .	9
2.2. Comparison of approximate pressure-time histories for $Z = 1 \text{ m/kg}^{1/3}$ . . . . .	10
2.3. Side-on blast parameters for a spherical charge as a function of scaled distance. . . . .	11
2.4. Geometric representation of Hopkinson-Cranz blast wave scaling. . . . .	12
2.5. Comparison of pressure-scaled distance relationships presented by various sources. . . . .	17
2.6. Reflection coefficient as a function of scaled distance from various sources. . . . .	20
2.7. Reflected blast parameters for a spherical charge as a function of scaled distance. . . . .	20
2.8. Uniform transverse blast loading on a plate. . . . .	22
3.1. Plate geometry and coordinate system. . . . .	26
3.2. Roof shaped deformation pattern. . . . .	32
3.3. Stress-strain curve for a linearly elastic, perfectly plastic material. . . . .	38
3.4. Deflection-time history of a high strength aluminum $100 \times 100 \times 2.5 \text{ mm}$ plate for simple and clamped supports per three different models. . . . .	40
3.5. Cumulative distribution function of absolute percent error between finite element and current model for simple and clamped supports. . . . .	41
3.6. Average absolute percent error between finite element and current clamped model as a function of scaled distance for various plate areas. . . . .	43
3.7. Average absolute percent error between finite element and current clamped model as a function of scaled distance for various plate aspect ratios. . . . .	44
3.8. Ranges of validity for current clamped model with respect to plate size and aspect ratio. . . . .	46
4.1. Geometry of an ideal blast wave impacting a flat surface. . . . .	53
4.2. Reflection coefficient as a function of incident angle and pressure. . . . .	54

4.3. Circular bands of equal reflected pressure across a plate subjected to a centered 6 kg TNT charge with a 0.5 m standoff. . . . .	56
4.4. Reflected pressure distribution across a plate subjected to a centered 6 kg TNT charge with a 0.5 m standoff. . . . .	60
4.5. Side-on overpressure ratio $P_s/P_o$ as a function of scaled distance $\bar{R}$ from various experiments. . . . .	68
4.6. Deviation between side-on impulses reported in Table XI of Ref. [3] and via Eq. 2.6 for a chemical explosion. . . . .	70
4.7. Side-on spherical blast wave parameters as a function of scaled distance from various sources. . . . .	71
4.8. Side-on and normally reflected decay parameters as a function of scaled distance from various sources. . . . .	73
4.9. Comparison of pressure-time history generated for air burst per Eq. 4.1 and surface burst per Fig. 4.2. . . . .	74
4.10. Reflected pressure distribution across a plate subjected to a centered 6 kg TNT charge with a 0.3 m standoff. . . . .	77
5.1. Small fuselage section with small plate (SP) geometry shaded. . . . .	79
5.2. LD-3 luggage container with large plate (LP) geometry in front. . . . .	80
5.3. Comparison of maximum deflection results per Refs. [2,4] for an LD-3 panel subjected to uniform and nonuniform blasts from a 0.75 kg TNT charge. . .	84
5.4. Comparison of maximum deflection results per Refs. [2-4] for an LD-3 panel subjected to uniform and nonuniform blasts from a 0.75 kg TNT charge. . .	86
5.5. Comparison of maximum deflection results per Refs. [2-4] for an LD-3 panel subjected to uniform and nonuniform blasts from a 6 kg TNT charge. . . .	87
5.6. Comparison of maximum deflection results per Refs. [2-4] for a fuselage panel subjected to uniform and nonuniform blasts from a 0.75 kg TNT charge. . .	87
5.7. Normalized arrival time and impulse as a function of standoff distance, charge size and panel size. . . . .	88
5.8. Blast parameter bounds for use in Monte Carlo simulation. . . . .	92

5.9. Mean maximum deflection for an LD-3 panel (LP) subjected to an SC blast with standard deviation bounds. . . . .	93
5.10. Mean maximum deflection for an LD-3 panel (LP) subjected to an LC blast with standard deviation bounds. . . . .	94
5.11. Mean maximum deflection for a fuselage panel (SP) subjected to an SC blast with standard deviation bounds. . . . .	95
5.12. Probability of failure curves for SC/SP and LC/LP cases per assumed elastic and plastic deformation shapes. . . . .	96
6.1. Finite element results for instantaneous exponent of Eq. 6.8 for a $100 \times 100 \times 2.5$ mm Al 2024-T3 plate subjected to a uniform blast with $Z = 1$ . . . . .	102
6.2. LD-3 luggage container deformed due to internal explosive loading. . . . .	104
6.3. Box shaped deformation pattern. . . . .	104
6.4. Upper right-hand quadrant of box shaped deformation pattern. . . . .	106
6.5. Moment-causing loads acting on region I of box shaped deformation pattern. . . . .	109
6.6. Transient deformation profiles of a clamped, high strength aluminum $150 \times 100$ mm plate due to a uniform load for $Z = 1$ . . . . .	111
6.7. Transient deformation profiles of a clamped aluminum $150 \times 100 \times 2.5$ mm plate due to a uniform load for varying yield strengths and scaled distances. . . . .	112
6.8. Shell geometry and coordinate system. . . . .	115
C.1. Roof shaped and box shaped, rigid plastic deformation patterns with notation of Ref. [64]. . . . .	139

# Chapter 1

## Introduction

As a result of escalating terrorist threats in recent years, the potential damage caused by an explosion onboard an aircraft has become a necessary design consideration. There are multiple ways to study the response of a structure subjected to an explosive loading. The best way is through experiment, which provides the most realistic response data. However, experiments are costly as specimens and explosives, and often measuring devices (e.g., pressure transducers), cannot be reused. Numerical simulations (i.e., hydrocodes) have the benefit of increased repeatability, but, depending on the complexity of the finite element model, can take days to process a single loading case. Additionally, without sufficient experience, finite element programs are essentially black boxes that convert input to output data. Each code has its own unique way of solving the relevant governing equations that must be validated over numerous trials.

Simplified analytical models serve as an efficient alternative to finite element models. Results from simplified models are repeatable, relatively quick to process, and based on engineering theory, so that they give physical insight into the problem. As a result, parameter studies can be easily performed in the initial stages of structural design. Once a preliminary design is chosen, a more detailed finite element model can be used to finalize all aspects of the design. Using simplified models saves on both the cost and time of unnecessary finite element and experimental trials. Moreover, they can be used to verify more detailed finite element results when experimental data are unavailable.

### 1.1 Dissertation Motivation

The primary application here is the structural response of thin plates to an applied explosive blast. In order to predict this response, both said loading and resulting structural

behavior must be accurately modeled. As such, this dissertation examines simple, yet accurate analytical models of explosive pressure loading and thin, rectangular plates. The study of thin, rectangular plates is useful in aviation design as such plates can model the skin panels that cover a given airframe or the panels of a luggage container stored beneath the cabin (see Figs. 5.1 and 5.2). Moreover, the large deflection, dynamic response of these plates to a transverse pressure pulse can aid in making an aircraft structure that is resilient to an internal explosion.

Key parameters for input into the pressure model, such as incident and reflected pressures, impulse (i.e., the area under the pressure-time curve), and blast duration, can be determined from various sources. Common sources used in the literature include the charted data of Baker and his colleagues [1,2], the tabulated data of Kinney and Graham [3] based on empirical equations, and specialized computer programs such as ConWep [4]. However, a problem arises in that these references yield data that are often inconsistent with one another and experimental results, particularly for close standoffs. Therefore, there is a general need for a more consistent set of blast parameter data, or at least some way to measure the uncertainty of design calculations based on the data from these common sources.

Moreover, typically in the literature, explosive blasts are assumed to act uniformly across a target area. Many times there is no justification given for this assumption. Other times the rationale is simply that the explosion occurs “far enough away” to form a nearly planar wave upon impact. As the procedure for calculating a nonuniform pressure can quickly become burdensome, it is useful to the designer to have a quantitative criterion to determine when a uniform loading is or is not appropriate. Further, when deemed inappropriate, it is also beneficial to have a simplified procedure for estimating the nonuniform pressure profile acting across a target area. Ideally, from a mathematical standpoint, this pressure profile should be a closed form expression of position and time.

In addition, there is a general need for more accurate structural modeling. For a single-degree-of-freedom (SDOF) model of a structure subjected to an external load, appropriate factors are usually taken from the classical text of Biggs [5]. These factors, based on an assumed deformation shape, aid in establishing equations of motion for elastic, elastic-plastic and plastic response. However, as shown in the master’s thesis of the current author [6],

this procedure tends to grossly overpredict deflections for thin metallic plates. The linear resistance functions tabulated in Ref. [5] seem to be more applicable for reinforced concrete slabs. Conversely, cubic functions are required for metallic plates in order to better capture these plates' internal resistance to deformation via membrane stretching. In Ref. [6], this conclusion is reached primarily on representative example calculations.

## 1.2 Dissertation Contribution

The simplified large deflection, elastic-plastic plate model of the current author's earlier work [6] is outlined in this dissertation. Moreover, this structural model is validated through comparison with both finite element and previously published experimental results. Suggestions for improvement to this model are made, which include retaining higher-order modal terms in the elastic regime and incorporating a box shaped deformation pattern in the plastic regime. As opposed to using only a common moment balance approach, the current author develops equations of motion (Eqs. 6.19 and 6.20) for the box shaped profile via an energy rate balance. Furthermore, this simplified plate model is extended for use with cylindrical shells subjected to an internal blast pressure.

Whereas Ref. [6] considers only uniform blast loading, this dissertation also examines nonuniform pressure distributions. It is shown that for close-in explosions, a nonuniform distribution is necessary to capture the correct maximum structural displacement. Only once the charge is moved a substantial distance away from the target area does the loading become approximately uniform. As very few papers discuss this transition region or give a numerical value for the required "substantial distance," a means of gauging when a uniform explosive pressure loading can be assumed is proposed here. The resulting normalized criteria are defined by Eqs. 4.6 and 4.8. These criteria are later evaluated through comparison with the finite element results of two charge sizes at various standoffs.

Other current practices for modeling an explosive pressure load are also thoroughly examined. It is found that while blast parameters such as incident and reflected pressures are widely available in the literature, others like reflected decay constant are not. Figure 4.8 displays the value of this previously unavailable parameter, showing the large difference

between it and its unreflected analog.

It is also found that there are many inconsistencies in these commonly used methods that have yet to be acknowledged in the literature. For example, this dissertation shows that the approximate relationship between side-on and reflected values of pressure and impulse given in Refs. [1,2] (Eq. 2.15) rarely holds. Furthermore, Fig. 4.6 shows that the tabulated impulse data of Kinney and Graham [3] significantly differ from those attained via a supplied equation within the same text. Meanwhile, Fig. 4.7 reveals there are even greater deviations between the loading duration values in the aforementioned text [3] and those produced by ConWep [4].

Furthermore, this dissertation uses a methodology similar to that of Bogosian et al. [7] to establish appropriate error bounds for the “deterministic” blast data given in Refs. [2–4]. With ranges of applicability defined for each blast parameter, a Monte Carlo scheme is incorporated to generate trial sets of these parameters for input into the simplified plate model of Ref. [6]. As a result, confidence bounds are also placed on the output, maximum plate deflections. This procedure allows for the generation of probability of failure curves (see Fig. 5.12), which are useful in structural design, for various loading conditions.

Moreover, the importance of some secondary factors are examined. One factor is the inclusion of reflected pressures past an incident angle of  $40^\circ$ , where Mach effects may be introduced. Another is consideration of the negative pressure phase. Many studies ignore both factors, but each may become significant when dealing with close-in explosions of lightweight structures. The end result of this analysis is the preliminary development of a closed form nonuniform pressure history, variant in both space and time.

The procedures described above are by no means limited to only aircraft structures. Indeed, only a handful of comparable works study that particular problem (e.g., Refs. [8,9]). Instead, most experimental research (e.g., Refs. [10–12]) has focused on the general blast loading of metallic (aluminum and primarily steel) plates. In particular, these experimental studies examine the various plate failure modes (e.g, large inelastic deflection and shear failure). Some form of simplified structural response prediction (e.g., Ref. [13]) almost always accompanies the experimental results provided in these studies. As such, the methods used in this dissertation have a wide range of applicability.

### 1.3 Dissertation Outline

Chapter 2 covers the basic concepts related to explosive loading. The modified Friedlander equation (see Eq. 2.1) is presented as a simple, yet accurate representation of an explosion's pressure-time history. Blast scaling is introduced as a means of organizing the parameters in this equation, which are determined experimentally from tests on charges having various sizes and standoffs. Both side-on and reflected blast parameters are covered, but the discussion in Chapter 2 is limited to pressures acting at a single point in air or acting uniformly across a target area.

The uniform pressure profile developed in Chapter 2 is used as input into the various plate equations of motion of Chapter 3. These equations comprise the elastic-plastic structural model with yield condition proposed in the master's thesis of the current author [6] for both simply supported and clamped boundary conditions. This model is summarized in Chapter 3, and then validated with both finite element and experimental data for maximum and permanent deformation due to uniform blast loading.

Chapter 4 suggests improvements to the loading model of Chapter 2. A procedure for calculating a nonuniform pressure load is outlined, which motivates the development of a more generalized pressure function. In addition, two normalized criteria are proposed to aid the designer in determining when a uniform load can be used in lieu of the more complicated nonuniform distribution. Furthermore, various specialized effects and inconsistencies associated with blast scaling are detailed.

Chapter 5 compares the plate deflection results obtained from the uniform pressure model of Chapter 2 with those from the nonuniform model of Chapter 4. A finite element model is also used to compare these results. Moreover, the normalized criteria proposed in Chapter 4 are evaluated, leading to recommendations for their use. Additionally, the blast parameter uncertainties addressed previously are incorporated into a Monte Carlo scheme to determine mean deflections and confidence bounds. Likelihood of failure curves are developed from these statistics.

Furthermore, Chapter 6 suggests some improvements to the elastic-plastic structural model introduced in Chapter 3. These suggestions include modifying the assumed elastic

deformation shape by using a higher-order Fourier series expansion or changing the associated exponent of Eq. 3.12. Moreover, the plastic equations of motion are changed to correspond to a box shaped deformation pattern. Attempts are made to smooth the transition between the elastic and plastic phases, as well as to include material damping. In addition, the supplied plate equations are extended for use with cylindrical shells.

Finally, Chapter 7 offers conclusions pertaining to the covered material. Some possible areas of future work are also suggested. Meanwhile, sample computer programs used in this dissertation are provided in Appendices A and B. Further details regarding the box shaped deformation pattern are shown in Appendix C.

## Chapter 2

### Typical Explosive Loading Model

The methods described in this chapter summarize those presented in numerous sources in the open literature. Baker and his associates [1, 2] provide an excellent background of the fundamentals of explosive loading. The former text provides extensive theory and experimental data as related to external loading, while the latter adds material on internal blasts and simplified structural response. Kinney and Graham [3] give a less detailed treatment of these topics, while discussing explosions in air in a compressible fluids context. Many key parameters are related to an appropriate Mach number, as opposed to only an incident pressure or scaled distance as in Refs. [1, 2]. Numerous empirical relationships for both chemical and nuclear explosions are also provided in Ref. [3]. It should be noted that the structural response coverage in Refs. [2, 3] originate from the definitive structural dynamics text of Biggs [5].

Some more classical work on explosions assuming a point source can be found in Refs. [14–16]. These works are a sampling of the vast research performed by Taylor [14, 15] and von Neumann [16], which are collected in multiple volume sets covering such topics as the formation, propagation and decay of detonation waves, Mach effects and oblique shock reflection. Furthermore, Brode [17] numerically simulated the motion of an explosive gas assuming a spherical wave from a point source. He provides empirical relationships for positive and negative phase blast parameters as a function of scaled distance. In addition, Brode [18] examined the similar propagation coming from a spherical TNT charge.

As one may find it difficult to obtain the older texts and articles mentioned above, some modern, general sources are also provided. These sources are supplemented with recent research on blast loading throughout this chapter. Smith and Hetherington [19] thoroughly capture the important loading and response aspects of the Baker texts [1, 2],

while Beshara [20, 21] reviews only the loading model in these references, but for both internal and external blasts. Additionally, Bulson [22] gives a lengthy history of explosives research, covering not only explosions in air, but also underwater, underground and in tunnels. Meanwhile, Tedesco et al. [23] present a complete overview of blast loads on structures, inclusive of oblique reflections, in Chapter 19 of their structural dynamics text. Florek and Benaroya [24] review the effects that the shape of a pressure pulse has on the response of both aviation and more general engineering structures. Finally, in a more current review article, Zhu and Lu [25] summarize the various failure modes and modal approximations of plastic structures due to blast and impact loading. A focus is placed on experimental and numerical modeling of metal and sandwich beams and plates.

## 2.1 Side-On Blast Parameters

The pressure-time history in Fig. 2.1 captures the major trends of an explosion as would be recorded by a pressure transducer some finite distance away from the charge. Initially, there is zero overpressure (i.e., only ambient pressure  $P_o$  acts at the transducer). Once the blast wave reaches the gauge, there is a near instantaneous rise to a peak side-on overpressure ( $P_s$ ), where “side-on” refers to an impact without reflection, usually acting tangential to a surface. This peak is followed by a sharp decay back to zero overpressure. This positive pressure phase has a duration of  $T_s$ , typically lasting only a few milliseconds, and an impulse (i.e., the area under the pressure-time curve) denoted by  $i_s$ .<sup>1</sup>

The positive phase is followed by a negative pressure phase, which generally has a much smaller impulse. Due to this fact and that an underpressure would reduce the amount of transverse deflection, the negative phase is usually ignored during a structural analysis. Indeed, only the positive phase is considered by the popular, numerical blast wave generator ConWep [4]. However, as noted by Baker et al. [2] and detailed in Section 4.2.1, in certain situations, the negative phase can become significant.

The positive pressure phase in Fig. 2.1 can be mathematically described by the modified

---

<sup>1</sup>Throughout this dissertation, impulse is given in units of pressure multiplied by time (e.g., Pa·s or bar·ms), as opposed to the more traditional units of force multiplied by time (e.g., N·s).

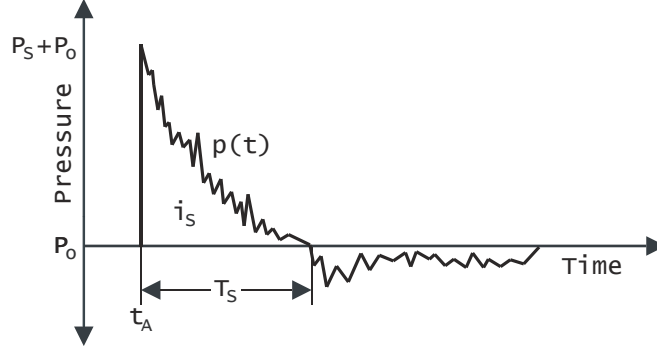


Figure 2.1: Typical blast wave pressure-time history with parameter definitions.

Friedlander equation (e.g., Ref. [26]), namely

$$p(t) = P_o + P_s \left(1 - \frac{t - t_A}{T_s}\right) e^{-\alpha(t - t_A)/T_s}, \quad (2.1)$$

where  $t_A$  is the time it takes for the blast wave to initially strike the target, and  $\alpha$  is the exponential time constant. Equation 2.1 is a commonly accepted compromise between a simple triangular load (where  $\alpha = 0$ ) and more complicated expressions that incorporate additional curve-fit parameters [1]. Triangular loads, as frequently used in blast design charts (e.g., Ref. [5]), preserve the peak pressure and impulse of a blast wave. This results in a fictitious duration time equal to  $2i_s/P_s$ , which is less than the measured  $T_s$ , as shown in Fig. 2.2. Moreover, when maximum structural response occurs early relative to  $T_s$ , the decay rate of the pressure model should match that of the actual blast wave [20]. Per Fig. 2.2, this would result in both a fictitious duration and impulse, both much smaller than actually measured, for a simple triangular profile. As it incorporates more parameters to better match the actual blast wave pressure-time history, the Friedlander waveform does not pose this latter issue. Furthermore, Eq. 2.1 has an advantage over a simple exponential decay, where the  $(1 - \frac{t - t_A}{T_s})$  term is removed, in that  $p(t)$  reduces to ambient pressure at some finite time.

Since parameters  $P_s$ ,  $T_s$  and  $i_s$  are recorded experimentally,  $\alpha$  is typically determined by setting  $i_s = \int_{t_A}^{t_A + T_s} p(t) dt$ . Evaluating this integral with  $p(t)$  as defined in Eq. 2.1 results in the transcendental equation

$$i_s = P_s T_s \left( \frac{1}{\alpha} - \frac{1}{\alpha^2} + \frac{e^{-\alpha}}{\alpha^2} \right). \quad (2.2)$$

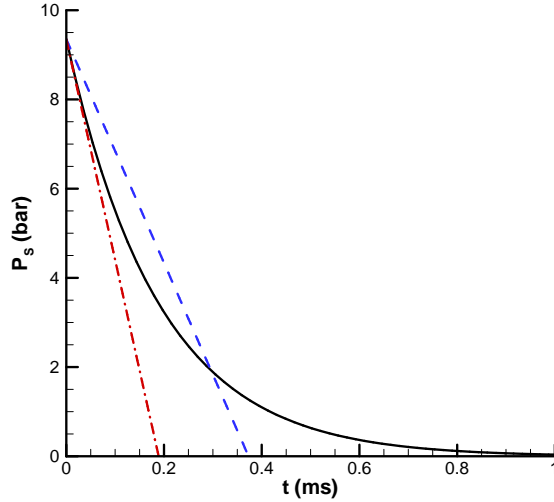


Figure 2.2: Comparison of approximate pressure-time histories for  $Z = 1 \text{ m/kg}^{1/3}$ : —, Friedlander waveform; ---, triangular load preserving impulse; - · - · -, triangular load preserving initial decay rate.

However, as noted in Refs. [1, 3],  $\alpha$  can also be obtained by matching the initial decay rate of an actual blast load, namely  $dp/dt$  at  $t = t_A$ . This method becomes necessary for the case of early maximum response as mentioned above.

## 2.2 Blast Scaling

The parameters listed above can be attained graphically from Fig. 2.3 or from various sources (e.g., Refs. [2, 19, 23]) as a function of the scaled distance  $Z$ , defined by

$$Z = R/W^{1/3}. \quad (2.3)$$

Here,  $R$  is the standoff distance from the blast origin to the target, and  $W$  is the mass equivalent of trinitrotoluene (TNT), a measure of potential blast energy. This “cube-root scaling” allows a wide range of experiments to be compared, assuming all rate-dependent and gravity effects are negligible, and that self-similar blast waves are formed by charges of the same explosive and geometry detonated at the same scaled distance under the same atmospheric conditions [1]. When comparing tests of different explosives, it is assumed

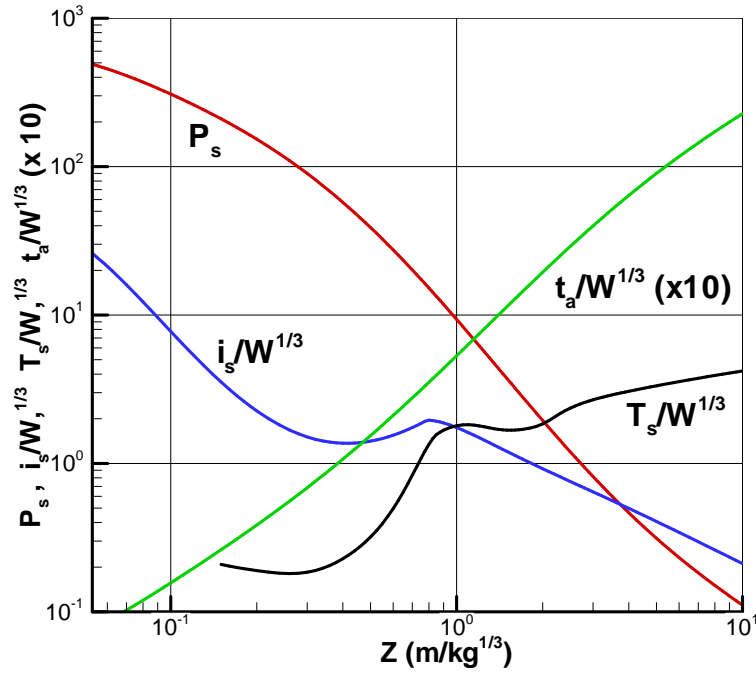


Figure 2.3: Side-on blast parameters for a spherical charge as a function of scaled distance, where the following units are used:  $P_s$  (bar),  $i_s/W^{1/3}$  (bar-ms/kg<sup>1/3</sup>),  $T_s/W^{1/3}$  and  $t_a/W^{1/3}$  (ms/kg<sup>1/3</sup>). Data from Refs. [2, 4].

that similarity exists for explosives having the same mass equivalence. This notion of TNT equivalence is explored further in Section 4.2.3.

The concept of self-similar blast waves per the cube-root scaling law is shown graphically in Fig. 2.4.<sup>2</sup> A measuring device a distance  $R$  away from a detonating charge of diameter  $d$  records a peak pressure  $P$ , impulse  $i_s$ , positive duration  $T$  and arrival time  $t_a$ . Theoretically, a measuring device a distance  $KR$  away from a detonating charge of diameter  $Kd$  should record the same pressure as before, with all other parameters being scaled by the factor  $K$ . As detailed in Refs. [1, 29], the scaled parameters in Fig. 2.3 arise from a nondimensional analysis with a constant ambient pressure and speed of sound factored out, and energy assumed to be directly proportional to charge mass.

<sup>2</sup>The scaling represented by Eq. 2.3 is commonly referred to as ‘‘Hopkinson scaling’’ or ‘‘Hopkinson-Cranz scaling’’ in honor of the independent work of Hopkinson [27] and Cranz [28].

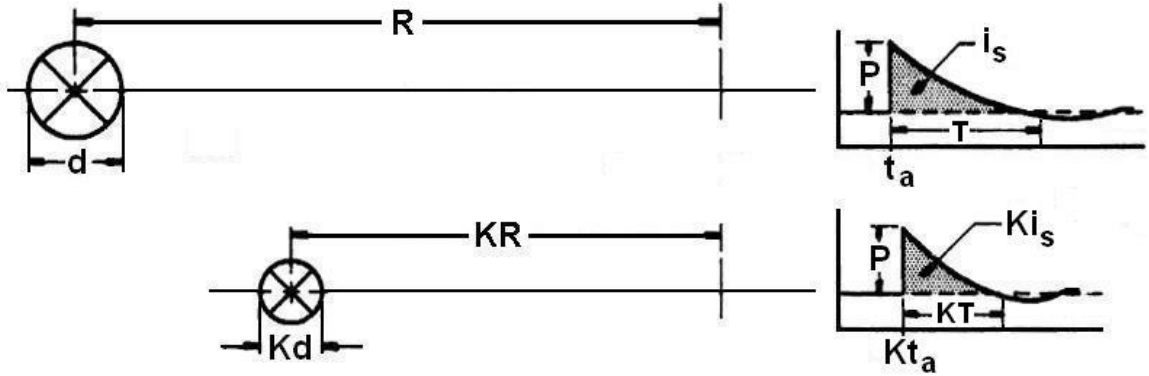


Figure 2.4: Geometric representation of Hopkinson-Cranz blast wave scaling [1].

For example, a 1 kg spherical TNT charge 1 m away from a given point on a target would have a  $Z$  value of  $1 \text{ m/kg}^{1/3}$ .<sup>3</sup> From Fig. 2.3, such a charge produces a blast with a peak side-on pressure of roughly 9.35 bar,<sup>4</sup> a duration of 1.8 ms and an impulse of 1.75 bar·ms. Inserting these values into Eq. 2.2,  $\alpha = 8.5$ . These parameter values can be substituted into Eq. 2.1 (with relative arrival time set to zero) to establish a pressure-time history at the given point. An 8 kg TNT charge with a standoff of 2 m would also have a  $Z$  value of  $1 \text{ m/kg}^{1/3}$ . However, while  $P_s$  and  $\alpha$  retain their values from the previous example,  $T_s/W^{1/3} = 1.8 \text{ ms/kg}^{1/3}$  now implies that  $T_s = 3.6 \text{ ms}$ . Similarly,  $i_s = 3.5 \text{ bar}\cdot\text{ms}$ .

The curves in Fig. 2.3 are the best-fit traces of Kingery and Bulmash [30,31] to the compiled data of many experiments on TNT and pentolite charges (e.g., Refs. [32,33]). These traces, which are reproduced by the computer program ConWep [4], are nearly identical to those presented by Baker et al. [2] for  $Z < 10$ . The proximity of the experimental data over a wide range of both standoff distance and charge mass serves to prove the cube-root scaling law. Yet, the shapes of the provided parameter curves are troubling. While one expects the pressure curve to decrease as scaled distance increases, as is predicted by the classical point source analysis of Taylor [15], the duration time curve should monotonically increase with  $Z$  value. Clearly, this is not the case for duration time in Fig. 2.3, where there is a relative maximum near  $Z = 1.1$ . Additionally, the scaled impulse curve also

<sup>3</sup>These units for  $Z$  are implied, if not stated, throughout the remainder of this dissertation.

<sup>4</sup>Standard atmospheric pressure is 1.01325 bar, where 1 bar equals 100 kPa or 14.504 psi.

shows a relative maximum, but at  $Z = 0.8$ .

Only a few sources [34,35] mention the kinks in these curves, but none were found that actually explain why the kinks are present. Through personal correspondences, Baker [36] and Gatto [37] give their reasonings. Baker [36] claims that upon reaching the charge radius, the blast wave formed by the exploding products within the charge reflects a rarefaction wave back towards the center of the charge.<sup>5</sup> It is apparently this rarefaction wave and the one that rereflects at the charge center that, in part, cause the oscillatory behavior in scaled duration at small  $Z$  values. The interaction between the expanding detonation products and air also contributes to this behavior. At the interface between these two media, properties such as density and speed of sound become altered from their ideal values (see Eqs. 2.11 and 2.12). This, in turn, results in a distortion of the ideal blast curve for air, particularly at distances close to the charge.

Furthermore, according to Gatto [37], the kink in the impulse curve arises from the fact that pressure decreases and blast duration generally increases as  $Z$  increases. At small scaled distances, the blast wave acts at a very high pressure over a very small time. For larger distances, the blast wave acts at a small pressure, but over a longer period. As a result, there reaches a point near  $Z = 0.8$  where impulse achieves a relative maximum. These thoughts are echoed by Brode [18], who notes a dip in impulse when the internal energy of a spherical TNT blast reaches a minimum concurrently with the kinetic energy achieving a maximum. Brode [18] claims the dip to be artificial in that the phenomenon discussed by Baker [36] causes a premature end to the positive pressure phase. A reduced duration time, in turn, leads to a reduced impulse.

### 2.3 Simplified Parameter Relationships

As an alternative to charts such as Fig. 2.3, blast parameters can be determined as relatively simple functions of  $Z$  from curve-fit equations. As stated above, the parameter traces in Fig. 2.3 are indeed themselves curve fits to experimental data. However, the polynomial equations associated with each parameter are unwieldy, involving logarithmic

---

<sup>5</sup>More details on wave reflection can be found in Section 2.4, while more details on spherical charges and rarefaction waves can be found in Chapter 4.

and exponential functions of as high as ninth-order terms. In addition, some parameters need two or three sets of such equations to describe their behavior over the entire range of scaled distances, like Eqs. 2.8aa-c below. These complicated polynomial expressions can be found in Refs. [30,38].

A popular set of simpler equations is provided by Kinney and Graham [3], who developed asymptotic, Bode-type relations commonly used in control theory (e.g., Ref. [39]). For chemical (i.e., non-nuclear) explosions, these equations are as follows:

$$P_s = \frac{808P_o \left[1 + \left(\frac{Z}{4.5}\right)^2\right]}{\sqrt{\left[1 + \left(\frac{Z}{0.048}\right)^2\right] \left[1 + \left(\frac{Z}{0.32}\right)^2\right] \left[1 + \left(\frac{Z}{1.35}\right)^2\right]}}, \quad (2.4)$$

where the units of  $P_s$  match that of  $P_o$ , and

$$\frac{T_s}{W^{1/3}} = \frac{980 \left[1 + \left(\frac{Z}{0.54}\right)^{10}\right]}{\left[1 + \left(\frac{Z}{0.02}\right)^3\right] \left[1 + \left(\frac{Z}{0.74}\right)^6\right] \sqrt{1 + \left(\frac{Z}{6.9}\right)^2}}, \quad (2.5)$$

where  $T_s$  is in units of milliseconds and  $W$  is in kg TNT. It should be noted that Beshara [20] incorrectly states that  $Z$  is scaled for the energy release of 1 kt (kiloton) of TNT, which would be appropriate for a nuclear explosion.

Additionally, Kinney and Graham [3] provide the impulse relation

$$i_s = \frac{0.067 \sqrt{1 + \left(\frac{Z}{0.23}\right)^4}}{Z^2 \sqrt[3]{1 + \left(\frac{Z}{1.55}\right)^3}}, \quad (2.6)$$

which is based on independent data for chemical explosions with  $i_s$  in units of bar·ms. This formula assumes a charge mass of 1 kg TNT. However, the validity of Eq. 2.6 is brought into question in Section 4.3.2.

Many works use Eqs. 2.4-2.6 over a wide range of  $Z$  values. For example, Akerman et al. [40] applied Eq. 2.4 to calculate the peak pressure acting on eight fuselage shielding panels in experimental tests of explosions onboard an aircraft. In their study, charges with scaled distances of 1.39 and 1.75 m/kg<sup>1/3</sup> were exploded either bare or in filled suitcases near shields of two different densities. Further, Jacinto et al. [41] made use of Eqs. 2.4 and 2.5 to approximate the pressure-time history of shock waves caused by four explosions with  $13.9 \leq Z \leq 55$ . The resulting triangular load was modified to account for a clearing time

(see Section 4.2.2) before being input into the finite element code ABAQUS for comparison with experimental data. Additionally, Koper et al. [42] used Eqs. 2.4-2.6 in an attempt to estimate the yields of four car bomb explosions. Only the pressure equation was found to give accurate results, but scaled distances were limited to  $Z > 64$ .

Furthermore, using the parameter data in Table XI of Ref. [3], Wei and Dharani [43] developed their own curve fit equations for peak side-on pressure, duration time and decay constant, namely

$$\frac{P_s}{P_o} = \frac{0.696}{Z} + \frac{2.1}{Z^2} + \frac{4.13}{Z^3}; \quad (2.7a)$$

$$\frac{T_s}{W^{1/3}} = 24.44Z^{1/5} - \frac{0.0316}{Z} - 40.99; \quad (2.7b)$$

$$\alpha = -0.0697Z - \frac{9.63}{Z} + \frac{15.9}{Z^2} - \frac{5.65}{Z^3} + 2.735. \quad (2.7c)$$

Equations 2.7aa-c made it easier for Wei and Dharani [43] to implement the modified Friedlander waveform into their equations of motion of a laminated glass panel subjected to blast loading. Their model was used to simulate four experimental cases with  $Z = 8.45$  or  $Z = 13.9$ . It should be noted that Eqs. 2.7aa-c have been modified by the current author to work with metric units. This modification produces more manageable coefficients (the maximum is 15.9 in Eq. 2.7ac) than those originally given by Wei and Dharani [43], where some constants exceeded 100,000.

Some additional equations for side-on pressure in terms of scaled distance are provided in Refs. [19, 20, 22]. For example, the inverse polynomial expressions of Henrych [44] are given as

$$P_s = \frac{14.072}{Z} + \frac{5.54}{Z^2} - \frac{0.357}{Z^3} + \frac{0.00625}{Z^4} \quad (\text{for } 0.053 \leq Z \leq 0.3); \quad (2.8a)$$

$$P_s = \frac{6.194}{Z} - \frac{0.326}{Z^2} + \frac{2.132}{Z^3} \quad (\text{for } 0.3 \leq Z \leq 1); \quad (2.8b)$$

$$P_s = \frac{0.662}{Z} + \frac{4.05}{Z^2} + \frac{3.288}{Z^3} \quad (\text{for } 1 \leq Z \leq 10), \quad (2.8c)$$

where  $P_s$  is measured in bar. Brode [17] uses equations of a similar form with as high as third-order terms, like Eqs. 2.7aa and 2.8ab-c.<sup>6</sup> However, as shown in Ref. [19], Eqs. 2.8aa-c are a better match of experiment results than Brode's equations [17] for short-range

---

<sup>6</sup>The theoretical pressure-distance solution of a spherical charge (e.g., Ref. [15]) is a one-term inverse cubic of  $Z$ .

explosions (i.e.,  $Z < 0.3$ ). It should be noted that Ref. [20] incorrectly provides Eq. 2.8cc with a minus sign on the inverse cubic term.

Moreover, Philip [45] suggests the form

$$P_s = \frac{a_1}{Z} \exp\left(b_1/Z^{1/2}\right), \quad (2.9)$$

where  $a_1$  and  $b_1$  are empirically obtained constants. Meanwhile, Philip [45] proposes a form of  $T_s/W^{1/3}$  similar to that of Eq. 2.9, but with the  $1/Z$  term removed and the constant  $b_1$  negative. As for impulse, Philip [45] finds that  $i_s/W^{1/3}$  is proportional to  $1/Z$ . Held [46] revisits this impulse relationship, citing that the proportionality constant  $B$  ranges between 1-10 bar·ms·m/kg<sup>2/3</sup>, with a mean value of 3 bar·ms·m/kg<sup>2/3</sup>. In contrast to Ref. [45], Held [46] presents a pressure that is proportional to  $1/Z^2$ , with linear constant  $A$  ranging between 6-60 bar·m<sup>2</sup>/kg<sup>2/3</sup>, having a mean of 20 bar·m<sup>2</sup>/kg<sup>2/3</sup>. Here, the given lower bounds for  $A$  and  $B$  are for side-on blasts, while the upper bounds are more appropriate for head-on reflected blasts (see Section 2.4). Held [46] warns though that the given values for  $A$  and  $B$  result in only order of magnitude estimates of peak pressure and impulse. These estimates are applicable exclusively as first approximations for the respective parameters.

Furthermore, Collins [47] assumes  $P_s$  to be an exponential function of  $A/(Z + B) - C$ , where again  $A$ ,  $B$  and  $C$  are obtained empirically. A primary goal of these researchers [3,17,43–47] is to mathematically represent the curves in Fig. 2.3 as simply and as accurately as possible to ease the complexity of analytical and numerical calculations. Figure 2.5 compares the pressure-scaled distance relations given by these authors. It is clear that there is a wide discrepancy between the various sources for  $Z \leq 0.5$ , with the exponential fit of Collins [47] yielding the lowest pressures for close-in explosions ( $P_s = 243$  bar at  $Z = 0.053$ ).<sup>7</sup> The most popular sources (i.e., Refs. [3, 4]), meanwhile, are within 10% of one another for all  $Z \leq 6$ . In contrast, the remaining curve [44] in the lower pressure set [3, 4, 44, 47] only comes within 10% of the ConWep [4] data for a small window between  $Z = 0.2$  and  $Z = 0.35$ , and later for  $Z \geq 2$ .

The other curves [17, 43, 45, 46] in Fig. 2.5 appear to grossly overestimate pressure

---

<sup>7</sup>The minimum possible  $Z$  value is 0.053, which corresponds to the outer radius of a spherical TNT charge with density 1600 kg/m<sup>3</sup> [19].

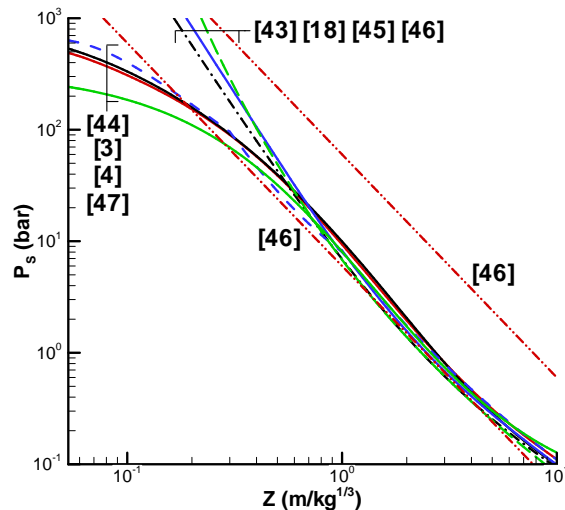


Figure 2.5: Comparison of pressure-scaled distance relationships presented by various sources. The two curves attributed to Ref. [46] are lower and upper bounds.

for  $Z < 0.5$  before more or less collapsing onto one another for higher scaled distances. However, caution should be taken especially when using the curves of Refs. [17, 43, 45, 46] as the logarithmic scaling of Fig. 2.5 can make the pressure values seem closer than they really are. For example, at  $Z = 0.5$ , the various pressure models still have a fairly large spread between 28 and 55 bar. Of particular note amongst the higher pressure set curves are that of Wei and Dharani [43] and Held [46]. As mentioned earlier, the former is supposed to be a best fit of the data within Ref. [3]. However, in Fig. 2.5, Wei and Dharani's approximating function is only within 10% of Kinney and Graham's data [3] for  $0.5 \leq Z \leq 0.6$  and  $Z \geq 5.5$ . Furthermore, the upper bound of Held [46] seems to be overly conservative for all scaled distances. It is much more appropriate for the reflected pressures of the next section. In contrast, his lower bound is fairly representative for  $Z \geq 0.2$ , even though it does not give the lowest pressures amongst Refs. [3, 4, 17, 43–45, 47] for much of the  $Z$  range. Some of the curves in Fig. 2.5 are used by the current author in Chapters 4 and 5 to develop levels of uncertainty in published blast pressure data.

## 2.4 Reflected Blast Parameters

When a blast wave first comes in contact with a surface, the incident wave reflects, causing an increase in pressure [1]. This pressure increase is due to two separate phenomena—acoustic doubling of the incident pressure and the dynamic pressure  $q_s$  bringing the compressed air to rest at the reflecting surface. Quantitatively, for shocks acting normal to a rigid reflecting surface,

$$P_r = 2P_s + (\gamma + 1) q_s, \quad (2.10)$$

where  $P_r$  is the reflected overpressure, and  $\gamma$  is the specific heat ratio of the compressed air.

Using the Rankine-Hugoniot equations [48] to relate shock front density  $\rho_s$  and particle velocity  $u_s$  to their respective ambient counterparts  $\rho_o$  and  $u_o$ ,

$$\rho_s = \rho_o \frac{(\gamma + 1) P_s + 2\gamma P_o}{(\gamma - 1) P_s + 2\gamma P_o} \quad (2.11)$$

and

$$u_s = P_s \sqrt{\frac{2}{\rho_o [(\gamma + 1) P_s + 2\gamma P_o]}}. \quad (2.12)$$

Although Eqs. 2.11 and 2.12 look complicated, they arise essentially from a mass and energy balance across the shock (see Ref. [1]). As  $q_s = \rho_s u_s^2 / 2$ , substituting Eqs. 2.11 and 2.12 into Eq. 2.10 yields

$$C_r \equiv \frac{P_r}{P_s} = 2 \left[ \frac{(3\gamma - 1) P_s / 2 + 2\gamma P_o}{(\gamma - 1) P_s + 2\gamma P_o} \right], \quad (2.13)$$

where  $C_r$  is termed the reflection coefficient. This expression is a reworked version of Eq. 3-3 given in Ref. [2] and of the analogous Eq. 5-12 in Ref. [3], where  $C_r$  is in terms of absolute peak pressure  $P_s + P_o$  instead of overpressure.

Typically, air is considered to behave as an ideal gas so that  $\gamma = 1.4$  for all pressures. Inserting this value for the specific heat ratio into Eq. 2.13,

$$C_r = 2 \frac{4P_s + 7P_o}{P_s + 7P_o}. \quad (2.14)$$

For weak shocks (i.e.,  $P_s \ll P_o$ ), the acoustic term in Eq. 2.10 dominates the dynamic term so that  $C_r \approx 2$ . For strong explosions (i.e.,  $P_s \gg P_o$ ), the dynamic term is dominant, and the ambient pressures in Eq. 2.14 drop out, resulting in  $C_r \approx 8$ .

However, there is contention between Refs. [1–3] as to whether the specific heat ratio is constant for high pressures. Baker and his colleagues [1, 2] claim that air ionizes and dissociates as shock strength increases, resulting in a variable  $\gamma$  and a  $P_r$  that can be an order of magnitude larger than the corresponding normal incident overpressure  $P_s$ . This assertion is repeated by Smith and Hetherington [19] and Beshara [20] in their reviews of blast loading on structures. Moreover, in their parametric study of reflected shocks, Kingery and Pannill [49] provide specific heat ratios varying between 1.119 and 1.402. Inserting  $\gamma = 1.2$  into Eq. 2.13 yields an upper limit of  $C_r = 13$ , in-line with the charted data of Refs. [1, 2, 4]. When  $\gamma = 1.1$ ,  $C_r$  can reach a value of 23, near the maximum possible value cited in the references above.

In contrast, Kinney and Graham [3] state that the upper limit for reflection coefficient in air is  $C_r = 8$ . As shown in Fig. 2.6, using Eq. 2.14 with the stated upper bound gives better approximations as scaled distance increases. There is at least a 5% error between the curves for  $Z < 0.65$ , at least a 10% error for  $Z < 0.5$ , and at least a 20% error for  $Z < 0.27$ . The maximum deviation of 37.7% occurs at  $Z = 0.053$ . It should be noted that the limit assertion of Ref. [3] is erroneously copied in the textbooks of Bulson [22] and Tedesco et al. [23], as well as in the work of Kambouchev et al. [48], who studied fluid-structure interaction problems as related to blast loading.

It appears that the reflected pressure distribution, ignoring re-reflections, can be described by substituting  $P_r$  for  $P_s$  in Eq. 2.1. This claim, which is brought into question in Section 4.3.3, gains credence in that only pressure and impulse typically have reflected analogs in published charts. Figure 2.7 compares the side-on and reflected values of these parameters. In contrast, arrival and duration times, as well as decay constant, are usually only given one value. For the analysis of Chapter 3, it is assumed that  $t_A$ ,  $T_s$  and  $\alpha$  retain their values for a reflected blast wave. The arrival time equivalency is obvious since the presence of a reflecting surface has no bearing on the time it takes for the blast wave to reach said surface. Meanwhile, Baker [1] provides some data for a reflected positive duration  $T_r$  different than  $T_s$ . But since the amount of collected data is sparse and measuring duration time is at times arbitrary [34], duration time equivalency is more out of convention.

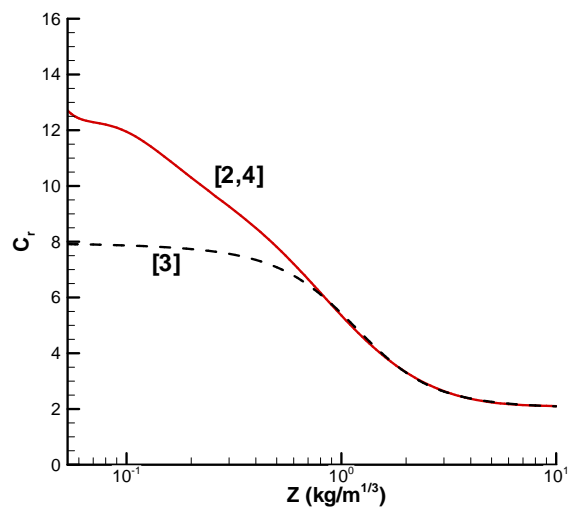


Figure 2.6: Reflection coefficient as a function of scaled distance from various sources.

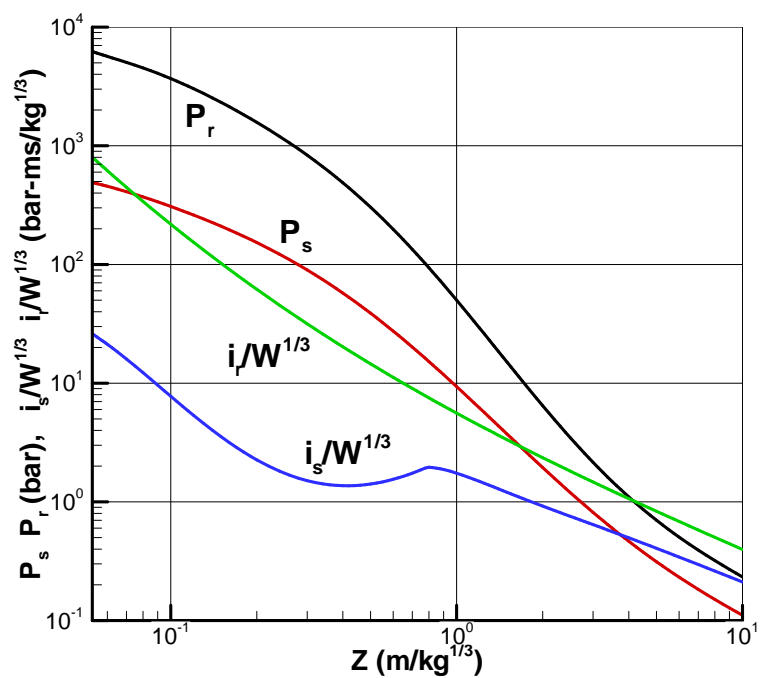


Figure 2.7: Reflected blast parameters for a spherical charge as a function of scaled distance [2, 4].

If the above assumptions are correct, the approximation [2]

$$\frac{P_r}{P_s} \approx \frac{i_r}{i_s} \quad (2.15)$$

between reflected and side-on values of pressure and impulse should hold. A value for  $P_r$  can be determined from Fig. 2.7 or similar reflected blast parameter charts in the literature. Alternatively, since  $P_r = C_r P_s$ ,  $P_r$  can be calculated by extracting appropriate values from Figs. 2.3 and 2.6. Luccioni et al. [50] used Eq. 2.15 in conjunction with Eq. 2.14 and the tabulated impulses of Ref. [3] (see Fig. 4.6) to determine reflected impulses for comparison with the hydrocode AUTODYN. They also incorporated Eqs. 2.8aa-c with Eq. 2.14 to calculate comparable reflected pressures in their study of blast wave propagation on buildings.

## 2.5 Uniform Loading

Thus far, only methods for determining the pressure-time history at a point some distance away from an explosion have been discussed. In order to compute an entire structure's response to a blast, the pressure-time history must be known at all points on the pressure-acting surface. If a spherical charge is far enough away from the structure or if the target area is sufficiently small, the blast wave from the exploding charge acts essentially like a planar wave upon impact.<sup>8</sup> Therefore, the pressure distribution can be assumed to act uniformly across the target area, as shown in Fig. 2.8. When assuming a uniform pressure distribution, only one scaled distance  $Z$  needs to be calculated. In Eq. 2.3,  $R$  would be the normal measured from the center of the spherical charge to the flat target surface. Meanwhile, the equivalent mass  $W$  for a non-TNT charge would be calculated by multiplying the actual charge mass by an appropriate equivalence factor (see Section 4.2.3). This  $Z$  value would then be used to find parameters  $P_s$ ,  $T_s$  and  $\alpha$  as described above. As the blast wave reaches all points on the surface nearly simultaneously, the incident pressure distribution of Eq. 2.1 becomes fully described by setting the reference arrival time  $t_A = 0$ .

Most journal papers assume a uniform pressure distribution for simplicity, regardless of application. Gupta et al. [51] considered the pressure due to a charge with  $P_r = 68.9$

---

<sup>8</sup>The expression "far enough away" is clarified in Chapter 5.

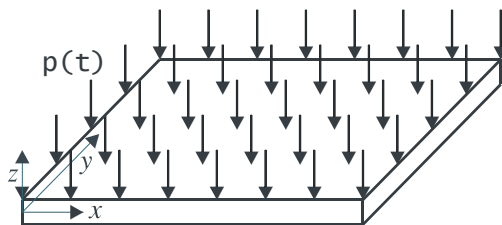


Figure 2.8: Uniform transverse blast loading on a plate.

bar,  $i_r = 79$  bar-ms and  $T_s = 4$  ms to be uniform across a  $1.016 \times 0.381 \times 0.00127$  m hinged, steel plate. Meanwhile, Guven et al. [52] assumed that a  $1 \times 0.45$  m section of an aluminum sandwich plate was subjected to a uniform triangular blast with a peak pressure of 1 GPa and duration of  $1 \mu$ s. Both of these studies [51,52] numerically model armor panels for military applications. In contrast, Veldman et al. [8] experimentally and numerically subjected a small section of an aircraft fuselage to an onboard explosion. Representative, pre-pressurized  $0.152 \times 0.152 \times 0.0016$  m aluminum plates were exposed to the blasts from two C-4 charges. The standoff distance of 1.52 m for both charges was deemed sufficiently large so as to produce planar blast waves. Furthermore, in their numerical model, Louca and Wadee [53] assumed a uniform blast was formed due to a hydrocarbon explosion acting on a  $2 \times 1$  m steel plate of variable thickness from an offshore structure. The aforementioned work of Wei and Dharani [43] also incorporates entirely uniform loading. This approach is further used throughout the analysis of Chapter 3.

## Chapter 3

### Validation of Structural Model for Uniform Pressure Load

As noted by Teng et al. [54] and Nurick and Martin [55], relatively few papers in the literature have considered the large deflection, dynamic response of rectangular plates to an applied load.<sup>1</sup> In contrast, most address only static behavior or circular plates. Moreover, the papers that do treat dynamic response typically consider either purely elastic or purely plastic deformations, but not both. Timoshenko and Woinowsky-Krieger [57] derived elastic governing equations using both  $w-u-v$  (assumed transverse and in-plane deflection shapes) and  $w-F$  (assumed transverse deflection shape and Airy stress function) formulations. The  $w-u-v$  formulation, although mathematically valid, may yield some unexpected values due to the first order approximation of displacements  $u$  and  $v$ . Whether this method truly conserves the plate's total energy, even when keeping higher order terms, is questionable. This point was remarked on by Lee [58, 59], who suggests using the alternative  $w-F$  formulation instead. Indeed, Teng et al. [54] and Bauer [60] use this theory in their elastic plate analyses, which deal with stress free boundaries and both stress free and immovably constrained edges, respectively. Both of these papers incorporate the Galerkin method in order to obtain nonlinear equations of motion related to their assumed transverse deflection shape. This same procedure was used more recently by Wei and Dharani [43] and by Lai et al. [61], who examined the possible chaotic behavior of simply supported plates subjected to an arbitrary loading.

As for purely plastic analyses, Jones [62, 63] and Yu and Chen [64] also assume the plate's deflection shape. Their deformations are not sinusoidal, however, but rather they consist of either four or five rigid sections separated by plastic hinges, where all energy dissipation is

---

<sup>1</sup>This chapter is a modified version of work by Florek and Benaroya [56]. Further details of the structural model herein can be found in Ref. [6].

concentrated. These methods, along with those reviewed by Nurick and Martin [55], prove to be suitable when pressures are in excess of the static collapse load, so elastic effects can be ignored entirely.

Conversely, when the pressure does not remain above the collapse load, as is the case with an exponentially decaying load, elastic deformations may be significant. In this situation, an elastic-plastic model is needed. Typically, such models are entirely numerical, relying on finite element runs for a solution. However, as stated in Chapter 1, single-degree-of-freedom (SDOF) systems can serve as valuable design tools. Biggs [5] suggests breaking an SDOF plate model into elastic, elastic-plastic and plastic parts, each governed by a linear equation of motion with a different transformed stiffness. However, as also noted in Chapter 1, for large deflections, these linear stiffness terms do not adequately represent the plate's internal membrane resistance. A nonlinear stiffness is needed so as not to severely overestimate the amount of deflection caused by an applied pressure.

In this vein, Singh and Singh [65] propose using Bauer's [60] nonlinear elastic formulation for thin plates subjected to a decaying pressure pulse up until a gross yield condition is met. At this point, Singh and Singh [65] suggest using the rigid plastic method of Johnson and Mellor [66] to estimate the plastic deformation attained during the remaining application of the load. This simple procedure was originally modified in the master's thesis of the current author [6], where the hinge line method of Jones [62, 63] replaces the plastic model of Ref. [66]. The important aspects of the resulting elastic-plastic structural model are outlined in Sections 3.1 and 3.2. The remainder of this chapter serves to validate this model through comparison with both finite element and experimental results. Loadings here are assumed to be completely uniform. Nonuniform loads, meanwhile, are considered in the structural analysis of Chapter 5.

### 3.1 Elastic Phase Structural Model

#### 3.1.1 General Governing Equations

As given by Bauer [60], the two governing equations for dynamic response of an elastic plate using the  $w$ - $F$  formulation are

$$\nabla^4 F = E \left\{ \left( \frac{\partial^2 w}{\partial x \partial y} \right)^2 - \frac{\partial^2 w}{\partial x^2} \frac{\partial^2 w}{\partial y^2} \right\} \quad (3.1)$$

and

$$\frac{Eh^3}{12(1-\nu^2)} \nabla^4 w + \rho h \ddot{w} = p(x, y, t) + h \left\{ \frac{\partial^2 F}{\partial y^2} \frac{\partial^2 w}{\partial x^2} + \frac{\partial^2 F}{\partial x^2} \frac{\partial^2 w}{\partial y^2} - 2 \frac{\partial^2 F}{\partial x \partial y} \frac{\partial^2 w}{\partial x \partial y} \right\}, \quad (3.2)$$

where  $E$  is the elastic modulus,  $h$  the plate thickness,  $\nu$  Poisson's ratio,  $\rho$  the mass density of the plate,  $p$  the pressure acting on the plate, and the operator  $\nabla^4 \equiv \frac{\partial^4}{\partial x^4} + 2 \frac{\partial^4}{\partial x^2 \partial y^2} + \frac{\partial^4}{\partial y^4}$ . By definition, the Airy stress function  $F$  is related to the in-plane membrane stresses by

$$\sigma_x = \frac{\partial^2 F}{\partial y^2}, \quad \sigma_y = \frac{\partial^2 F}{\partial x^2} \quad \text{and} \quad \sigma_{xy} = -\frac{\partial^2 F}{\partial x \partial y}. \quad (3.3a-c)$$

Equations 3.1 and 3.2 comprise what is commonly referred to as von Kármán large deflection theory. However, in reality, deflections per this theory are limited to the order of the plate thickness since the aforementioned equations, which respectively follow from continuity and a force balance, are derived assuming small strains and moderately large rotations. As such, the expression “moderately large deflection theory” may be a more accurate description.

The deflections in Eqs. 3.1 and 3.2 are assumed so as to satisfy the plate's boundary conditions. In this chapter, two such conditions are examined—entirely simply supported edges and entirely clamped edges. The equations of motion for these two boundary cases during the elastic phase are derived in Sections 3.1.2 and 3.1.3, respectively.

#### 3.1.2 Simply Supported Plate

Assuming a sinusoidal, elastic deflection shape as per Refs. [43, 54, 60, 65], the transverse deflection of the plate in Fig. 3.1 is taken as

$$w(x, y, t) = hf(t) \cos \frac{\pi x}{a} \cos \frac{\pi y}{b}, \quad (3.4)$$

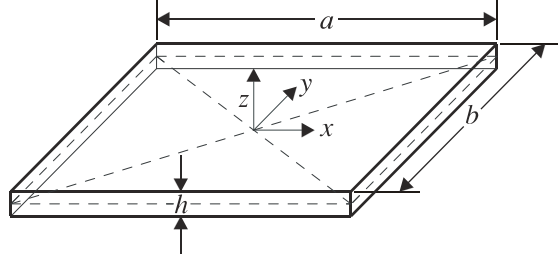


Figure 3.1: Plate geometry and coordinate system.

where  $f$  is an arbitrary time function, and  $a \geq b$ . Clearly,  $hf(t)$  gives the maximum plate deflection for all  $t$ . Equation 3.4 satisfies the simply supported boundary conditions that there be no transverse deflection along the plate edges (i.e.,  $w = 0$ ) and that the flexural moments per unit length, namely

$$M_x = \frac{-Eh^3}{12(1-\nu^2)} \left( \frac{\partial^2 w}{\partial x^2} + \nu \frac{\partial^2 w}{\partial y^2} \right) \quad (3.5a)$$

and

$$M_y = \frac{-Eh^3}{12(1-\nu^2)} \left( \frac{\partial^2 w}{\partial y^2} + \nu \frac{\partial^2 w}{\partial x^2} \right), \quad (3.5b)$$

equal zero along the boundaries  $x = \pm a/2$  and  $y = \pm b/2$ , respectively. The latter constraint is satisfied in that each second partial derivative in Eqs. 3.5a-b is independently zero at the specified edges.

Meanwhile, per Bauer [60], the Airy stress function is assumed to be of the form

$$F(x, y, t) = F^*(x, y)f^2(t), \quad (3.6)$$

where  $F^*$  is an entirely spatial component, and  $f$  is the same function used in Eq. 3.4. As the Airy stress function is related to the normal and shear stresses in the plate, it is also a function of the mid-plane strains and, therefore, the mid-plane displacements  $u$  and  $v$ . So instead of assuming a shape function for these displacements, as one would do in a  $w$ - $u$ - $v$  formulation,  $u$  and  $v$  are now defined by

$$u = \int_0^x \left\{ \frac{1}{E} \left( \frac{\partial^2 F}{\partial y^2} - \nu \frac{\partial^2 F}{\partial x^2} \right) - \frac{1}{2} \left( \frac{\partial w}{\partial x} \right)^2 \right\} dx \quad (3.7a)$$

and

$$v = \int_0^y \left\{ \frac{1}{E} \left( \frac{\partial^2 F}{\partial x^2} - \nu \frac{\partial^2 F}{\partial y^2} \right) - \frac{1}{2} \left( \frac{\partial w}{\partial y} \right)^2 \right\} dy. \quad (3.7b)$$

The first term in brackets in Eqs. 3.7a-b gives the total mid-plane strain in the appropriate direction per theory of elasticity via Eqs. 3.3a-b. The second term removes the nonlinear strain caused by transverse displacement  $w$  [57]. This leaves either  $\partial u/\partial x$  or  $\partial v/\partial y$  remaining for integration.

Using Eqs. 3.1, 3.4, 3.6 and 3.7a-b, assuming the edges are immovably constrained (zero displacement and shear stress) in the plane of the plate, the following expression for the Airy stress function is found:

$$F(x, y, t) = \frac{Eh^2}{32} f^2(t) \left\{ \frac{2\pi^2}{1-\nu^2} \left[ \left( \frac{\nu}{a^2} + \frac{1}{b^2} \right) x^2 + \left( \frac{1}{a^2} + \frac{\nu}{b^2} \right) y^2 \right] - \left( \frac{a^2}{b^2} \cos \frac{2\pi x}{a} + \frac{b^2}{a^2} \cos \frac{2\pi y}{b} \right) \right\}. \quad (3.8)$$

Now substituting Eqs. 3.4 and 3.8 into Eq. 3.2 yields

$$\left\{ \rho h^2 \ddot{f}(t) + \frac{Eh^4 \pi^4}{12(1-\nu^2)} \left( \frac{1}{a^2} + \frac{1}{b^2} \right)^2 f(t) + \left[ \frac{Eh^4 \pi^4 (1/a^4 + 2\nu/a^2 b^2 + 1/b^4)}{8(1-\nu^2)} + \frac{1}{b^4} \cos \frac{2\pi x}{a} + \frac{1}{a^4} \cos \frac{2\pi y}{b} \right] \right\} f^3(t) \cos \frac{\pi x}{a} \cos \frac{\pi y}{b} - p(x, y, t) = 0. \quad (3.9)$$

As pointed out by Bauer [60], one cannot expect Eq. 3.9 to exactly satisfy the governing Eq. 3.2. Changing the right side of Eq. 3.9 to read the residue  $R$ , the Galerkin method, which assumes

$$\int_0^{b/2} \int_0^{a/2} R \cos \frac{\pi x}{a} \cos \frac{\pi y}{b} dx dy = 0, \quad (3.10)$$

is used to find the true nonlinear equation of motion for a simply supported plate,

$$\rho h \ddot{W} + \frac{Eh^3 \pi^4}{12a^4(1-\nu^2)} \left( 1 + \frac{a^2}{b^2} \right)^2 W + \frac{Eh\pi^4}{8a^4} \left[ \frac{1 + 2\nu a^2/b^2 + a^4/b^4}{1-\nu^2} + \frac{1}{2} \left( 1 + \frac{a^4}{b^4} \right) \right] W^3 = \frac{16}{\pi^2} p(t). \quad (3.11)$$

Here,  $W$  is substituted for  $hf(t)$  for consistency with the plastic phase equations, which are introduced in Section 3.2. Furthermore, as pressure is assumed to act uniformly across the plate,  $p(x, y, t)$  reduces to  $p(t)$ . It should be noted that the cosine terms in Eq. 3.10 correspond to the mode shape of Eq. 3.4. Changing the mode shape would also change the Galerkin integral.

### 3.1.3 Clamped Plate

For the case of a clamped plate, a similar procedure as detailed above was used by Bauer [60]. However, in order to satisfy the new boundary conditions, namely that both the transverse deflection and slope be zero at the edges, the transverse deflection shape of Eq. 3.4 is modified to

$$w = hf(t) \cos^2 \frac{\pi x}{a} \cos^2 \frac{\pi y}{b}. \quad (3.12)$$

This form of the clamped deflection shape is also used by Elgamel [67] in his study of the large deflection response of thin silicon diaphragms. Again assuming an Airy stress function of the form given by Eq. 3.6, substitution of Eq. 3.12 into Eq. 3.1 yields

$$\begin{aligned} F(x, y, t) = & \frac{Eh^2}{512} f^2(t) \left\{ \frac{24\pi^2}{1-\nu^2} \left[ \left( \frac{\nu}{a^2} + \frac{1}{b^2} \right) x^2 + \left( \frac{1}{a^2} + \frac{\nu}{b^2} \right) y^2 \right] \right. \\ & - \frac{a^2}{b^2} \left( 16 \cos \frac{2\pi x}{a} + \cos \frac{4\pi x}{a} \right) - \frac{b^2}{a^2} \left( 16 \cos \frac{2\pi y}{b} + \cos \frac{4\pi y}{b} \right) \\ & - 16a^2b^2 \left[ \frac{2}{(a^2+b^2)^2} \cos \frac{2\pi x}{a} \cos \frac{2\pi y}{b} + \frac{1}{(4a^2+b^2)^2} \cos \frac{2\pi x}{a} \cos \frac{4\pi y}{b} \right. \\ & \left. \left. + \frac{1}{(a^2+4b^2)^2} \cos \frac{4\pi x}{a} \cos \frac{2\pi y}{b} \right] \right\}, \quad (3.13) \end{aligned}$$

which was originally derived in Ref. [6]. Although Eq. 3.12 indeed satisfies the clamped boundary conditions, the choice of an exponent  $n = 2$  is arbitrary. Any exponent  $n > 1$  will also give a function that yields no deflection or slope at the plate edges. It appears that  $n = 2$  is chosen to facilitate the integrations involved with obtaining the Airy stress function and subsequent equation of motion, namely Eq. 3.14. The implications of using Eq. 3.12 as the assumed deflection shape are further addressed in Section 6.1.

As was done before for the simply supported case, the expressions for deflection and stress function, now Eqs. 3.12 and 3.13, respectively, are substituted into Eq. 3.2, yielding a rather lengthy expression. Also as earlier, all non-zero terms in this expression are brought to one side, resulting in the residue  $R$ . Using the Galerkin method with the assumed mode shape of Eq. 3.12, the equation of motion for a clamped plate is found to be of the nonlinear form

$$\rho h \ddot{W} + \frac{4Eh\pi^4}{27a^4(1-\nu^2)} \left( 3 + 2\frac{a^2}{b^2} + 3\frac{a^4}{b^4} \right) [h^2W + C_f W^3] = \frac{16}{9} p(t), \quad (3.14)$$

where  $C_f$  is roughly constant. For  $0.25 \leq \nu \leq 0.35$  and  $1 \leq a/b \leq 2$ ,  $C_f \approx 0.51$ . It should

be noted that the linear and cubic terms were presented independently of one another in the equation of motion provided by Bauer [60]. Converting his equation into the form of Eq. 3.14,  $C_f \approx 0.52$  for the same  $\nu$  and  $a/b$  ranges. In all cases,  $C_f$  tends to decrease slightly as  $\nu$  decreases and  $a/b$  increases. Equation 3.14 is generalized for a nonuniform pressure in Section 5.1.3.

### 3.1.4 Yield Condition

However, Eqs. 3.11 and 3.14 are only valid in the elastic range. Once yielding occurs, another method must be employed to calculate the plate's plastic deformation. But before incorporating this new procedure, a yield condition must first be established to signify the transition between elastic and plastic regimes. Singh and Singh [65] suggest using a von Mises yield criterion. Per Massonnet [68], the von Mises yield condition is given by

$$Y_c \equiv \frac{M_x^2 + M_y^2 - M_x M_y + 3M_{xy}^2}{M_0^2} + \frac{N_x^2 + N_y^2 + N_x N_y + 3N_{xy}^2}{N_0^2} - 1 = 0, \quad (3.15)$$

where  $M_k$  and  $N_k$  represent the elastic bending moments per unit length and membrane forces per unit length, respectively, in either the  $x$ ,  $y$  or  $xy$  direction. Meanwhile,  $M_0$  is the plastic bending moment per unit length, and  $N_0$  the plastic membrane force per unit length. These quantities are defined as in Eqs. 3.5a-b and as

$$M_{xy} = \frac{-Eh^3}{12(1+\nu)} \frac{\partial^2 w}{\partial x \partial y}, \quad M_0 = \frac{\sigma_0 h^2}{4}, \quad (3.16a-b)$$

$$N_x = h \frac{\partial^2 F}{\partial y^2}, \quad N_y = h \frac{\partial^2 F}{\partial x^2}, \quad N_{xy} = -h \frac{\partial^2 F}{\partial x \partial y} \quad \text{and} \quad N_0 = \sigma_0 h, \quad (3.16c-f)$$

where  $\sigma_0$  is the dynamic yield stress for the plate material. For convenience, Eq. 3.15 is rewritten as

$$Y_c \equiv Y_m + Y_n - 1 = 0.$$

For a simply supported plate, by substituting Eq. 3.4 into Eqs. 3.5a-b and 3.16a-b, the first term of Eq. 3.15 becomes, after evaluating at the plate center ( $x = y = 0$ ),

$$Y_m(x, y, t) = \frac{E^2 h^4 \pi^4 f^2(t)}{9a^4 b^4 \sigma_0^2 (1 - \nu^2)^2} [(a^4 + b^4)(\nu^2 - \nu + 1) - a^2 b^2 (\nu^2 - 4\nu + 1)]. \quad (3.17)$$

Similarly, substituting Eq. 3.8 into Eqs. 3.16c-f, the second term of Eq. 3.15 becomes

$$Y_n(x, y, t) = \frac{E^2 h^4 \pi^4 f^4(t)}{64 a^4 b^4 \sigma_0^2 (1 - \nu^2)^2} [(a^4 + b^4) (\nu^4 - \nu^3 - 3\nu^2 + 2\nu + 4) + a^2 b^2 (\nu^4 - 4\nu^3 - 3\nu^2 + 8\nu + 4)]. \quad (3.18)$$

Therefore, by Eqs. 3.15, 3.17 and 3.18, the yield condition at the center of a simply supported plate is of the form

$$Y_c = \frac{E^2 \pi^4}{a^4 b^4 \sigma_0^2 (1 - \nu^2)^2} \left[ \frac{L_n}{64} W^4 + \frac{L_m h^2}{9} W^2 \right] - 1 = 0, \quad (3.19)$$

where  $L_m$  and  $L_n$  are functions of  $a$ ,  $b$  and  $\nu$ , given respectively by the bracketed terms in Eqs. 3.17 and 3.18. The yield condition given by Eq. 3.19 is said to be satisfied when  $Y_c$  first takes on a non-negative value. As noted in Refs. [6, 56], Eq. 3.19 differs substantially from the analogous expression for yielding presented by Singh and Singh [65].

A similar procedure is used to determine the yield condition of a clamped plate. First, Eq. 3.12 is inserted into Eqs. 3.5a-b and 3.16a-b. Then, Eq. 3.13 is inserted into Eqs. 3.16c-f. After combining the resulting expressions through Eq. 3.15, one finds that the yield condition at the center of a clamped plate is of the form

$$Y_c = \frac{E^2 \pi^4}{a^4 \sigma_0^2} \left[ \frac{L_n^*}{1024} W^4 + \frac{4L_m h^2}{9b^4(1 - \nu^2)^2} W^2 \right] - 1 = 0, \quad (3.20)$$

where  $L_m$  and  $L_n^*$  are functions of  $a$ ,  $b$  and  $\nu$ .  $L_m$  is again given by the bracketed term in Eq. 3.17, while  $L_n^* = A^2 + AB + B^2$ , where

$$A = \frac{3}{(1 - \nu^2)} \left( 1 + \nu \frac{a^2}{b^2} \right) + 5 + \frac{4a^4}{b^4} \left[ \frac{2}{(1 + a^2/b^2)^2} + \frac{4}{(1 + 4a^2/b^2)^2} + \frac{1}{(4 + a^2/b^2)^2} \right]$$

and

$$B = \frac{3}{(1 - \nu^2)} \left( \nu + \frac{a^2}{b^2} \right) + \frac{5a^2}{b^2} + \frac{4a^2}{b^2} \left[ \frac{2}{(1 + a^2/b^2)^2} + \frac{1}{(1 + 4a^2/b^2)^2} + \frac{4}{(4 + a^2/b^2)^2} \right].$$

### 3.2 Plastic Phase Structural Model

When a plate is subjected to a loading, it deforms elastically up until yielding first occurs at any point in the plate. At that time, with the addition of more load, both elastic and plastic deformations take place throughout the plate until the entire plate yields. At

that time, only plastic deformations continue to occur until the load is removed or at least substantially diminished below the static collapse load ( $p_c \approx 24M_0/b^2$  for a simply supported square plate).

But assuming, like Massonnet [68], that elastic-plastic interactions are negligible in a membrane, the SDOF deformations here are either purely elastic or purely plastic. The total deformation found by simply adding these two deflections is a reasonable approximation when both elastic and plastic deformations are significant. This assertion is further addressed in Sections 3.2.4 and 3.4.3.

The methods of the preceding sections allow the central elastic deflection of a rectangular plate to be found up until a yield condition is met. In order to estimate the plastic deformation, Singh and Singh [65] suggest using a method similar to that of Johnson and Mellor [66] for all loading after initial yield. However, it is unclear how exactly Singh and Singh incorporated Johnson and Mellor's methodology. As such, Jones' [62,63] comparable hinge line method is used here instead for post-yield response. For the transition from the elastic to the plastic phase to be as smooth as possible, it is assumed that the velocity at yielding is also the initial velocity of the plastic phase.

### 3.2.1 Plate Displacements and Angular Velocities

The assumed plastic deflection shape is the roof shaped pattern shown in Fig. 3.2, with one central plastic hinge and four non-central hinges extending from each corner to the central hinge. Although Jones [62,63] based his work on a similarly shaped, kinematically admissible velocity profile, all derivations here are made using the assumed deflection shape, which has been observed experimentally in blast tests [69] and used by Yankelevsky [70] in his elastic-plastic treatment of plates.

Clearly, from Fig. 3.2, the displacement pattern has a quarter symmetry. Taking the upper right quarter as a reference, the regional plate deflections are given by

$$w_I = W \left( 1 - \frac{2x'}{b \tan \phi} \right) \text{ and } w_{II} = W \left( 1 - \frac{2y}{b} \right), \quad (3.21a-b)$$

where  $W$  is the maximum plate deflection,  $\phi$  the angle of a non-central hinge projected onto the  $x$ - $y$  mid-plane, and  $x'$  a reference coordinate from the end of the central plastic

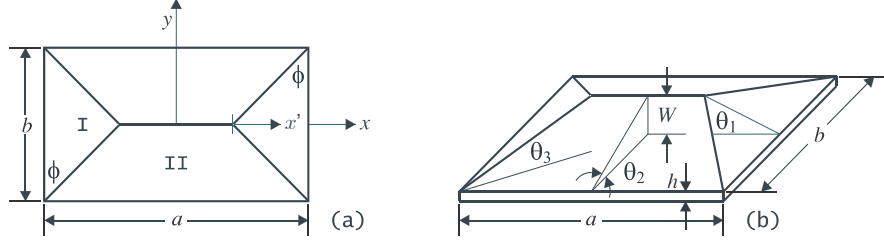


Figure 3.2: Roof shaped deformation pattern: (a) plan view, (b) isometric view.

hinge. Assuming  $\dot{\phi}$  small in comparison to  $\dot{W}$ , the velocities and accelerations of the two regions can be approximated by simply substituting either  $\dot{W}$  or  $\ddot{W}$  for  $W$  in Eqs. 3.21a-b. Furthermore, from geometry [6, 63], assuming that  $W < b/6$ , the angular velocities of regions I and II and the non-central hinges are given respectively by

$$\dot{\theta}_1 = \frac{2\dot{W}}{b \tan \phi}, \quad \dot{\theta}_2 = \frac{2\dot{W}}{b} \quad \text{and} \quad \dot{\theta}_3 = \frac{2\dot{W}}{b \sin \phi}. \quad (3.22a-c)$$

Much like the von Kármán elastic phase equations, the current plastic phase model has a limited range of applicability per the assumptions made throughout its derivation. Consequently, the theory holds for only “moderately large” plastic deflections. However, now deflections can be of the order of the plate width. Indeed, plastic deflections can easily exceed twenty times the plate thickness.

### 3.2.2 Energy Relationships

In addition to assuming zero in-plane velocities, taking both the in-plane displacements and accelerations as negligible compared to their out-of-plane counterparts yields the following statement of conservation of energy [62]:

$$\int (p - \mu \ddot{w}) \dot{w} dA = \sum_{m=1}^r \int (M + Nw) \dot{\theta}_m dl_m, \quad (3.23)$$

where  $p$  is the external transverse pressure acting on the plate area  $A$ ,  $\mu$  the plate mass per unit area, and  $w$  the transverse deflection along one of  $r$  plastic hinge lines of length  $l_m$ . Moreover,  $M$  and  $N$  are the acting bending moment and membrane force per unit length, respectively, and  $\dot{\theta}_m$  is the relative angular velocity across the  $m$ -th hinge. The

left-hand side of Eq. 3.23 is a balance between the external and inertial work rates, while the right-hand side represents the internal energy dissipation across all hinge lines.

Evaluating the terms on the left-hand side of Eq. 3.23,

$$\int (p - \mu \ddot{w}) \dot{w} dA = pb\dot{W} \left( L - \frac{1}{6}b \tan \phi \right) - \frac{2}{3}\mu b \ddot{W} \dot{W} \left( L - \frac{1}{4}b \tan \phi \right). \quad (3.24)$$

Meanwhile, in order to find the dissipation terms on the right-hand side of Eq. 3.23, a few auxiliary relations must first be given. From their definitions in Eqs. 3.16b and 3.16f, it is easily seen that the fully plastic membrane force and bending moment per unit length are related by

$$N_0 = \sigma_0 h = \frac{4}{h} \frac{\sigma_0 h^2}{4} = \frac{4M_0}{h}, \quad (3.25)$$

where  $\sigma_0$  is again the dynamic yield stress. Furthermore, membrane forces dominate the action of those parts of the plate where deflection has exceeded a critical value ( $W = h/2$  for a simply supported plate,  $W = h$  for a clamped plate). Hence, in these finitely deformed parts,  $M = 0$  and  $N$  takes on its fully plastic value, making

$$\dot{E}_{diss} = \sum_{m=1}^r \int (M + Nw) \dot{\theta}_m dl_m = \sum_{m=1}^r \int 4M_0 \frac{w}{h} \dot{\theta}_m dl_m. \quad (3.26)$$

For those regions where deflection is subcritical, it is assumed that membrane force is linearly related to deflection and that the flow rule

$$\frac{M}{M_0} + \left( \frac{N}{N_0} \right)^2 = 1 \quad (3.27)$$

applies.

Using Eqs. 3.22a-c and 3.25-3.27, the energy dissipation rate can be calculated along the five interior hinges of a simply supported plate or along the five interior and four support hinges of a clamped plate. Balancing these dissipation rates with the work rates from Eq. 3.24 and assuming  $\phi \approx 45^\circ$  throughout plastic deformation per Nurick et al. [71], the following governing equations are found:

$$\frac{\rho b^2}{\sigma_0 h} \left( \frac{2}{\beta} - 1 \right) \ddot{W} + \frac{24}{\beta} \frac{W}{h} + 2 \frac{h}{W} = \frac{pb^2}{\sigma_0 h^2} \left( \frac{3}{\beta} - 1 \right) \quad (3.28)$$

for a simply supported plate, and

$$\frac{\rho b^2}{\sigma_0 h} \left( \frac{2}{\beta} - 1 \right) \ddot{W} + \frac{24}{\beta} \frac{W}{h} + 8 \frac{h}{W} = \frac{pb^2}{\sigma_0 h^2} \left( \frac{3}{\beta} - 1 \right) \quad (3.29)$$

for a clamped plate, where  $\beta = b/a$ . Clearly, Eqs. 3.28 and 3.29<sup>2</sup> are identical save for the coefficient of the nonlinear  $h/W$  term.

### 3.2.3 Failure Criterion

With the assumptions made in their derivations, Eqs. 3.28 and 3.29 should prove accurate so long as  $W < b/6$ . Theoretically, beyond this limit, these equations are still usable, but accuracy is diminished. However, physically, there comes a point when the plastic deformation becomes so large that any additional strain leads to material failure (e.g., plate rupture).

For any structure, maximum strains occur at points where both the total deflection is high and the original length is relatively low. For a plate with the elastic or plastic deformation shapes above, this describes the symmetry line running across the plate width. The maximum deflection before plate rupture is approximated here then, by assuming that this line can only extend by 18% (the rupture strain for aluminum) of its original length,  $b$ . Therefore, the plate fails when strain  $\varepsilon = 0.18$ , where

$$\varepsilon = \frac{1}{b} \int_0^b \sqrt{1 + \left(\frac{dw}{dy}\right)^2} dy - 1, \quad (3.30)$$

and  $w$  is defined by any of Eqs. 3.4, 3.12 or 3.21b. This procedure was used by Olson et al. [72] to estimate the critical membrane strain in a steel plate subjected to a uniform blast pressure.

Table 3.1 lists the deflection at rupture for eight different plate sizes for the assumed elastic profiles of Eqs. 3.4 and 3.12 ( $W_{re}$ ), as well as the plastic profile of Eqs. 3.21a-b ( $W_{rp}$ ). Despite having dissimilar shapes, the rupture deflections for the elastic and plastic regimes are close, within about 9% of each other. In the current model, central deflections over  $W_{rp}$  predict a failure. Meanwhile, deflections between  $W_{re}$  and  $W_{rp}$  are considered borderline failure cases.

---

<sup>2</sup>These equations are only applicable when  $W > h/2$  and  $W > h$ , respectively. This restriction is expanded upon more in Section 3.3.

DC	a (mm)	b (mm)	a/b	Area (m <sup>2</sup> )	W <sub>re</sub> (mm)	W <sub>rp</sub> (mm)
A	100	100	1	0.01	28.73	31.32
B	150	100	1.5	0.015	28.73	31.32
C	200	100	2	0.02	28.73	31.32
D	225	150	1.5	0.03375	43.1	46.98
E	200	200	1	0.04	57.47	62.64
F	300	150	2	0.045	43.1	46.98
G	300	200	1.5	0.06	57.47	62.64
H	300	300	1	0.09	86.2	93.96

Table 3.1: Dimensional case definitions with deflections at rupture.

### 3.2.4 Permanent Deformation

Barring cases where material failure occurs, after the maximum central deflection is reached, the plate begins to deflect in the direction opposite that of the applied pressure. The plate then proceeds to oscillate about its final position. This vibration continues well after loading terminates. Eventually though, all of the energy introduced to the plate by the external loading is dissipated, and the plate motion ceases. For low intensity pressures, the response is purely elastic, and the plate returns to its original, preload shape. However, for more intensive loadings, the plate deforms plastically, resulting in a permanent set.

As neither the elastic (Eqs. 3.11 and 3.14) nor plastic (Eqs. 3.28 and 3.29) equations of motion contain dissipative terms (i.e.,  $\dot{W}$ ), these equations cannot produce a stationary, final deflection. Therefore, the current model cannot directly predict a final, permanent central plate deflection,  $W_p$  (see Section 6.2.5). Still, an approximation can be made assuming the relationship

$$W_p \simeq C_m W_{\max} - (1 - C_e) W_e, \quad (3.31)$$

where  $W_{\max}$  is the maximum central deflection attained by the current method, and  $W_e$  is the maximum elastic deflection or the deflection that first satisfies the appropriate yield condition (Eq. 3.19 or 3.20). Meanwhile,  $C_m$  and  $C_e$  ( $0 \leq C_e \leq 1$ ) are potential correction factors that are discussed in Section 3.4.3. Equation 3.31, in particular the  $C_e$  term, comes about due to the fact that an SDOF system cannot entirely account for the complex elastic-plastic interactions during large plate deformation. That is, one cannot expect the permanent deflection to simply equal the difference between the maximum overall and maximum elastic deflection for all cases. This difference though seems to give a lower bound

for permanent deflection. For non-intensive loadings,  $C_e = 0$ , so there is no permanent offset. In contrast, for highly intensive loadings,  $C_e$  tends towards 1, making the maximum and permanent deflections nearly equal. With no comparative data, correction factors  $C_m$  and  $C_e$  are assumed to take on values of 1 and 0, respectively.

### 3.3 Numerical Procedure

When analyzing the dynamic response of a simply supported plate, Eq. 3.11 is used up until the point Eq. 3.19 becomes positive. After this condition is met, Eq. 3.28 governs the plate motion. Similarly, Eq. 3.14 drives the dynamic behavior of a clamped plate until the yield condition of Eq. 3.20 is satisfied. Post-yield, Eq. 3.29 governs the clamped plate response. In this analysis, it is assumed that the critical plastic deflection values ( $W = h/2$  for simple supports and  $W = h$  for clamped supports) are reached during the elastic phase. If this is not the case, intermediate subcritical plastic equations of motion would need to be defined as in Jones [62,63]. These equations are also nonlinear, but with quadratic, instead of inverse, deflection terms (see Ref. [6]).

In contrast, for a rigid plastic analysis like Ref. [10], elastic response is assumed to be negligible. Therefore, the elastic equations of motion and yield criteria above would not be used. Instead, only Eqs. 3.28 and 3.29, along with the now necessary subcritical plastic equations of Jones [62,63], would be incorporated into an appropriate timestepping scheme.

#### 3.3.1 Timestepping Scheme

Whereas Bauer [60] suggests solving Eqs. 3.11 and 3.14 for the elastic phase by using a perturbation method, this dissertation uses a fourth-order Runge-Kutta method. As detailed by Jaluria [73], the Runge-Kutta method retains higher-order terms of the Taylor series expansion of a given function. This allows an ordinary differential equation containing that function to be broken up into multiple lower-order equations, which in turn, can be solved incrementally, with no limit on range of applicability. Timestepping Eqs. 3.11 and 3.14 can begin assuming  $W(0) = \dot{W}(0) = 0$ . Central plate deflection  $W$  is calculated at each time step ( $\Delta t \leq 1\mu s$ ) until the respective yield conditions of Eqs. 3.19 and 3.20 are

satisfied at  $t = t_{yield}$ .

For the plastic phase, the Runge-Kutta method is also used to timestep Eqs. 3.28 and 3.29. However, initial conditions are now  $W_{el}(t_{yield}) = W_{pl}(t_{yield})$  and  $\dot{W}_{el}(t_{yield}) = \dot{W}_{pl}(t_{yield})$ , so that the displacement and velocity between the elastic and plastic phases are continuous. This procedure, which is reexamined in Section 6.2.5, continues until a maximum deflection or a rupture deflection, as given in Table 3.1, is reached. These computations, carried out in Matlab<sup>®</sup> [74] on a Dell Precision 470 with a dual-core 2.8 GHz Intel Xeon processor, typically last only a few seconds for each dimensional case set.

### 3.3.2 Geometry and Material Properties

As an example, Singh and Singh [65] used their proposed method to determine the maximum deflection of both simply supported and clamped, high strength aluminum alloy  $100 \times 100 \times 2.5$  mm plates. These plates, representative of aircraft skin panels, were subjected to a uniform pressure due to detonation of a 1 kg TNT charge. Material properties were given as  $E = 75$  GPa,  $\nu = 0.33$ ,  $\rho = 2800$  kg/m<sup>3</sup> and  $\sigma_0 = 970$  MPa. In Section 3.4, the unspecified high strength alloy of Ref. [65] is considered along with a more typical Al 2024-T3 alloy, whose properties are taken as  $E = 73.1$  GPa,  $\nu = 0.33$  and  $\rho = 2780$  kg/m<sup>3</sup> as per Ref. [75] for both simply supported and clamped boundary conditions. Most notably, the dynamic yield strength of Al 2024-T3 is assumed to be the same as its static yield strength, so  $\sigma_0 = 345$  MPa. This assumption is reasonable for aluminum, which is essentially insensitive to strain rate effects. However, as is discussed in Section 3.5, this is not the case for steel plates.

Furthermore, various plate dimensions are examined here. Length and width are varied between 100 mm, as in Singh and Singh's paper [65], and 300 mm, which is comparable to the plate dimensions experimentally studied by Jones et al. [69]. This results in eight different dimensional combinations with an aspect ratio  $a/b$  of either 1, 1.5 or 2 (see Table 3.1). Meanwhile, thickness is taken as either 1 mm or 2.5 mm. Varying material properties, length, width and thickness, there are 32 different cases considered per pressure loading for each boundary condition.

The maximum deflections attained from the above procedure are compared with those

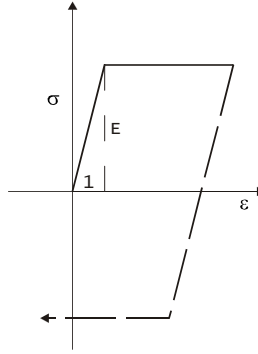


Figure 3.3: Stress-strain curve for a linearly elastic, perfectly plastic material.

found from the finite element software ANSYS<sup>®</sup> [76]. In ANSYS [76], the plate material is taken as bilinear-elastic, perfectly plastic, as depicted in Fig. 3.3. Square SHELL93 elements are used with a maximum side length of 12.5 mm to ensure proper coverage of all eight meshed areas. Each finite element run on the Dell Precision 470, with  $0.1 \leq \Delta t \leq 1\mu\text{s}$ , lasts between 15 and 90 minutes, depending on the plate dimensions and whether or not the plate fails.

As explained in Ref. [77], SHELL93 elements are useful in many applications as they support both large deflections and large strains. These elements each contain eight nodes, namely four corner and four mid-side. Furthermore, each node has six degrees of freedom, three translational and three rotational.

### 3.3.3 Pressure Loading

Like in Ref. [65], the uniform, transient pressures in Eqs. 3.11, 3.14, 3.28 and 3.29 are given by the modified Friedlander equation, namely Eq. 2.1. As suggested in Section 2.4, reflected pressure  $P_r$  is substituted for  $P_s$  in Eq. 2.1, while  $t_A$  is set to zero per Section 2.5 since the load is uniform. Blast parameter values, as obtained from charts in Baker et al. [2], are provided in Table 3.2 for the range of interest  $0.4 \leq Z \leq 2 \text{ m/kg}^{1/3}$ . This scaled distance range allows for deformations that are entirely elastic when  $Z = 2$ , and approximately rigid plastic when  $Z = 0.4$ . Between these extreme values, both elastic and plastic effects are generally significant. As the blast parameters are taken at ten different

$Z$ (m/kg <sup>1/3</sup> )	0.4	0.5	0.6	0.8	1	1.2	1.4	1.6	1.8	2
$P_r$ (MPa)	52	34	22.5	10.5	4.5	2.2	1.6	1.25	0.98	0.75
$T_s$ (ms)	0.215	0.3	0.5	1.2	1.8	1.65	1.6	1.7	1.8	1.9
$\alpha$	8.6	8.3	8.6	10	9	5.5	3.9	2.9	2.3	1.9

Table 3.2: Blast parameters as a function of scaled distance  $Z$ .

$Z$  values, there are 320 total trials per boundary condition.

### 3.4 Validation with Finite Element Analysis

In Singh and Singh’s [65] example problem, it was found that a simply supported, high strength aluminum  $100 \times 100 \times 2.5$  mm plate starts to yield at  $Z \approx 1.21$ . At this scaled distance, the maximum central deflections were 4.568 mm and 2.77 mm for simple and clamped supports, respectively. Fig. 3.4 plots Singh and Singh’s deflection-time histories for  $Z = 1.23$  against that produced by the finite element model and current method, both using the parameters in Table 3.2 for  $Z = 1.2$ .<sup>3</sup> There is good agreement between all three models, particularly between the latter two models for simple supports ( $W_{\max} = 3.983$  mm for the ANSYS [76] model,  $W_{\max} = 4.114$  mm for the current model, a 3.3% error). For clamped supports, a phase lag develops between these two models, but maximum deflections are nonetheless close ( $W_{\max} = 2.693$  mm for the ANSYS [76] model,  $W_{\max} = 2.857$  mm for the current model, a 6.1% error). Discrepancies with Singh and Singh’s model can most likely be attributed to their using different definitions for the parameters in Eq. 2.1 (see Ref. [3]).

#### 3.4.1 Simply Supported Plate

However, changing the plate dimensions greatly increases the deviations between the current simply supported model and its finite element analog. Keeping thickness constant, besides the square plate mentioned above (case A in Table 3.1), just four of the other seven dimensional cases produce maximum deflections within 10% of that output by ANSYS [76]. These are predominately the smaller area plates listed in Table 3.1 (B, C, D, G). The

---

<sup>3</sup>As there is some uncertainty reading the charted parameter values in Ref. [2], it is assumed that  $P_r$ ,  $T_s$  and  $\alpha$  for  $Z = 1.2$  and  $Z = 1.23$  are approximately equal. Indeed, interpolating parameter values for  $Z = 1.23$  from those in Table 3.2 shows hardly any difference for  $T_s$ , and only a 4% decrease in  $P_r$  and  $\alpha$ .

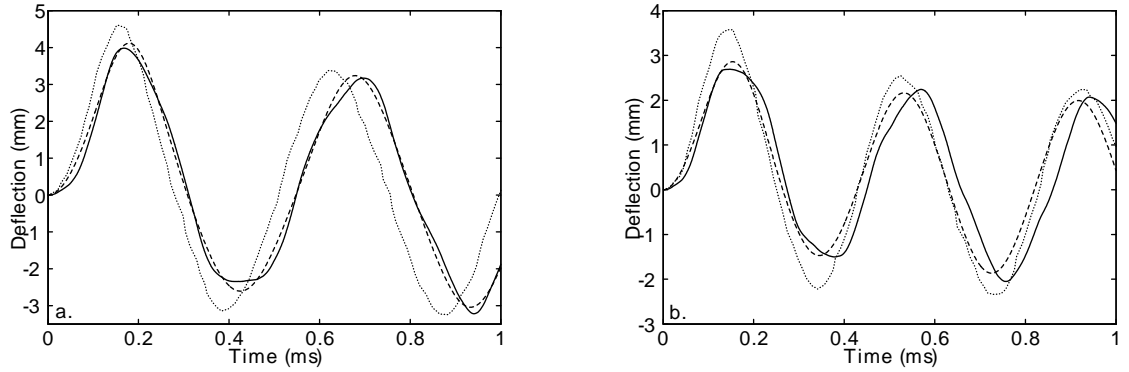


Figure 3.4: Deflection-time history of a high strength aluminum  $100 \times 100 \times 2.5$  mm plate for (a) simple supports, and (b) clamped supports, where: —, ANSYS,  $Z=1.2$ ; - - -, current model,  $Z=1.2$ ;  $\cdots$ , Ref. [14],  $Z=1.23$ .

largest deviation is for the largest area plate (H, 18.9% error). Changing  $\sigma_0$  to 345 MPa, only one of the total eight dimensional cases is within a 10% error for the same  $h$  and  $Z$ ; four cases have errors greater than 20%.

Figure 3.5a shows all of the simply supported run data from the current method as a cumulative distribution function. As detailed in Ref. [78], this type of function depicts the probability of an event being less than or equal to a selected value. In Figs. 3.5a-b, the selected value is the absolute percent error (APE) relative to the maximum deflection attained via finite element analysis. The specified parameter is the only one held constant between trials. Therefore,  $F_C(10\%) = 0.388$  for  $h = 2.5$  mm translates to 38.8% of the 160 simply supported, thicker plate trials per the current method being within 10% of their respective finite element solutions when  $a$ ,  $b$ ,  $Z$  and  $\sigma_0$  are all variable. Meanwhile, per Fig. 3.5a, 61.3% of the thicker plate trials are within 15%, and 79.4% are within 20%. The maximum error for  $h = 2.5$  mm is 27.7%. The most consistent approximations are made for the small area (A, B, C), high strength alloy plates when  $Z \geq 1.2$ . These plates undergo entirely elastic deformation so that Eq. (3.11) is the only equation of motion. Larger plate cases D and G, both with an aspect ratio  $a/b = 1.5$ , also produce highly accurate results for  $Z \geq 1.2$ , while undergoing small plastic deformation. The  $200 \times 100$  mm plate (C) actually gives very good results for both aluminum alloys over the entire  $Z$  range (an average 7.2% error over twenty cases).

Now, maintaining  $h = 1$  mm while varying  $\sigma_0$  and  $Z$ , 26 of the 160 simply supported

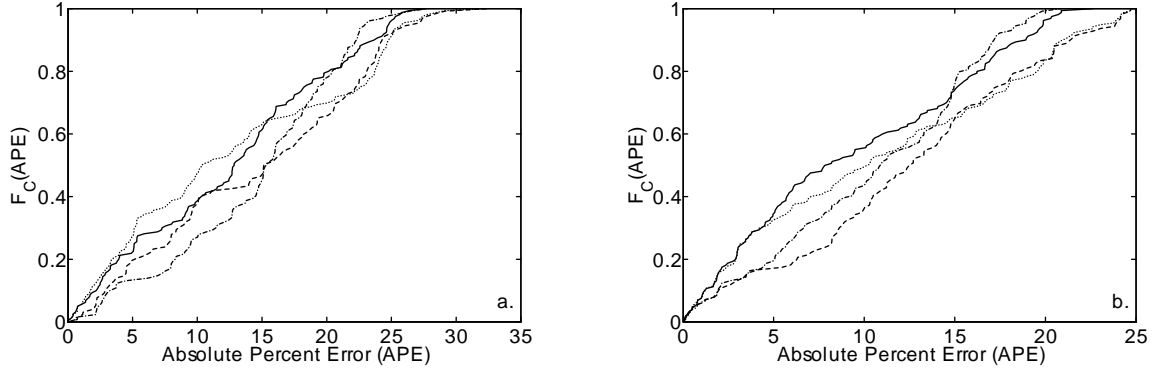


Figure 3.5: Cumulative distribution function of absolute percent error between finite element and current model for (a) simple supports, and (b) clamped supports, where: —,  $h = 2.5$  mm; ---,  $h = 1$  mm; ····,  $\sigma_0 = 970$  MPa; - · - · - ,  $\sigma_0 = 345$  MPa. The specified parameter is the only one held constant for a given trial set. Note: the given data represent 289 non-failed, simply supported (160 trials each for  $h = 2.5$  mm and  $\sigma_0 = 970$  MPa) and 286 clamped trials (160 trials for  $h = 2.5$  mm and 157 for  $\sigma_0 = 970$  MPa).

trials fail to converge to a solution for ANSYS [76], even for a refined grid size. The maximum strain criterion of Section 4.3 predicts failure for all of these trials, as well as in five additional trials (all 31 predicted failures also have  $\sigma_0 = 345$  MPa). It is seen from Fig. 3.5a that of the remaining 129 thinner plate trials per the current method, 37.2% are within 10% of their respective finite element results. Furthermore, slightly under half are within 15%, slightly under two-thirds are within 20%. The maximum error for  $h = 1$  mm is 32.3%. It appears that the current simply supported model is only a rough indicator of the physical maximum deflection behavior, particularly for the thinner plates.

Furthermore, Fig. 3.5a also shows the effect of varying thickness and scaled distance, while keeping the dynamic yield stress constant. The plates with a higher yield stress generally have a more accurate solution than their low strength analogs for  $h = 2.5$  mm and  $Z \geq 0.6$ . Still, for  $APE > 18\%$ ,  $F_C(APE)$  is greater when  $\sigma_0 = 345$  MPa. This reversal can be explained by the fact that the 31 failure trials, occurring exclusively when  $\sigma_0 = 345$  MPa,  $h = 1$  mm and  $Z \leq 0.8$ , are not considered for the development of the low strength curve. Therefore, the stiffer plates have more large error ( $h = 1$  mm) trials factored into  $F_C$  than do the Al 2024-T3 plates. On average, there is a 13.5% error for the current simply supported model over all 289 non-failed trials.

Comparing the results from the current method to those from a rigid plastic model,

the latter is generally more appropriate only when the loading is extremely intensive (i.e.,  $Z \leq 0.5$ ), and  $h = 1$  mm,  $\sigma_0 = 345$  MPa or the square plate area is large (E, H). This conclusion is expected since elastic effects become more negligible with increasing uniform load and decreasing material resistance.

### 3.4.2 Clamped Plate

In contrast, the current clamped model is generally an exceptional predictor of maximum deflection. As already stated, there is a 6.1% error for the current clamped model for the baseline case of a  $100 \times 100 \times 2.5$  mm plate with  $\sigma_0 = 970$  MPa and  $Z = 1.2$ . Varying the length and width per Table 3.1, the same four dimensional cases (B, C, D, G) as the current simply supported model produce maximum deflections within 10% of that given by ANSYS [76]. Like the simply supported model, the largest deviation for clamped edges is for the largest area plate (H, 19.9% error). Looking at the eight dimensional cases where  $h = 2.5$  mm,  $Z = 1.2$  and  $\sigma_0 = 345$  MPa, again only one clamped case (F, 2.1% error) is within a 10% error of its respective finite element solution. But unlike the current simply supported model, all clamped maximum deflections are within a 20% error.

Figure 3.5b shows the clamped run data from the current method as a cumulative distribution function. From this figure, it is seen that 55% of cases where  $h = 2.5$  mm are within a 10% error of the ANSYS [76] solutions, nearly three-quarters are within 15%, and 96.3% are within 20%. These numbers are a great improvement over the simply supported results. In fact, no errors for  $h = 2.5$  mm exceed 22.6%. The best approximations per the current method for  $h = 2.5$  mm are made when the area is small (A, B, C) and when either  $\sigma_0 = 970$  MPa and  $Z \geq 1$ , or  $\sigma_0 = 345$  MPa and  $Z \leq 0.8$ . For the first grouping, stiffer plates are being subjected to less intensive loads. This results in primarily elastic deformation governed by Eq. 3.14. For the second grouping, lower strength plates are being subjected to intensive pressures. These plates undergo mostly plastic deformation with Eq. 3.29 dominating response.

The fact that these two groupings of thin, small area plates give the best approximations can be better seen by interpreting Fig. 3.6a, which plots average absolute percent error against the scaled distance  $Z$  for dimensional cases A, B and C. Just like in Fig. 3.4, the

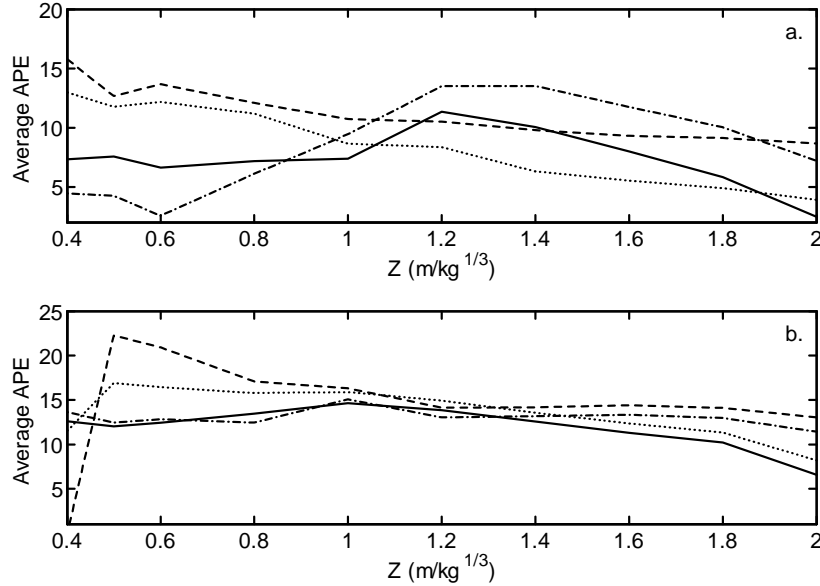


Figure 3.6: Average absolute percent error between finite element and current clamped model as a function of scaled distance for (a) small area cases, and (b) large area cases, where: —,  $h = 2.5$  mm; ---,  $h = 1$  mm;  $\cdots$ ,  $\sigma_0 = 970$  MPa; - · - · -,  $\sigma_0 = 345$  MPa. The specified parameter is the only one held constant for a given trial set.

parameter attributed to a given line in Fig. 3.6 is the only one held constant for a particular trial set. For example, the  $\sigma_0 = 970$  MPa line gives the average error attained at every  $Z$  for trials where thickness and surface area ( $SA \leq 0.02$  m<sup>2</sup>) are variable, but yield stress is fixed. Therefore, from Fig. 3.6a, the average percent error for all clamped, small area, high strength aluminum trials falls below 10% for  $Z \geq 1$ . As trials with  $h = 2.5$  mm have a relatively small percent error for all  $Z$  (the peak average error of 11.4% occurs at  $Z = 1.2$ ), the intersection of these ranges also produces a small percent error. Similarly, for the second grouping, the average percent error does not exceed 6.1% for trials where  $\sigma_0 = 345$  MPa and  $Z \leq 0.8$ . The reversal of yield stress curves in Fig. 3.6a near  $Z = 1$  shows the transition from plastic-dominant to elastic-dominant response.

Still, highly accurate results are also found in the intermediate elastic-plastic region. Similar to the simply supported runs, a clamped, high strength  $200 \times 100 \times 2.5$  mm plate has good agreement with finite element results over the entire  $Z$  range (an average 3.1% error over ten cases). Furthermore, the current clamped model also works well with a

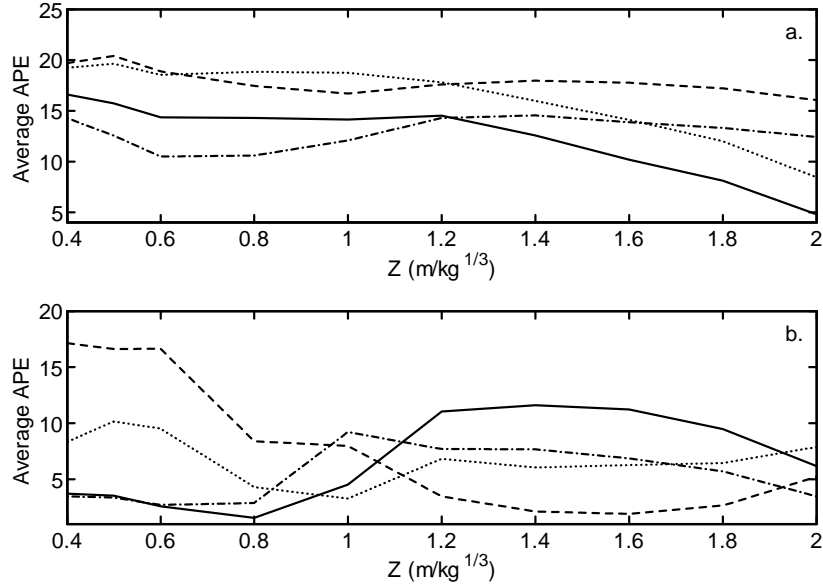


Figure 3.7: Average absolute percent error between finite element and current clamped model as a function of scaled distance for (a)  $a/b = 1$ , and (b)  $a/b = 2$ , where: —,  $h = 2.5$  mm; ---,  $h = 1$  mm; ····,  $\sigma_0 = 970$  MPa; -·-·-,  $\sigma_0 = 345$  MPa. The specified parameter is the only one held constant for a given trial set.

$300 \times 150 \times 2.5$  mm Al 2024-T3 plate for all  $Z$  (an average 4.3% error over ten cases). It should be noted that both of these plates have an aspect ratio  $a/b = 2$ . Indeed, from Fig. 3.7b, one can see that the average percent error for the more oblong plates (C, F) peaks at about 10%, regardless of which material strength is chosen. For  $Z \leq 1$ , the average percent error is less than 5% when  $h = 2.5$  mm. Outside of this  $Z$  range, the maximum average percent error for thicker, clamped plates is only 11.6%.

Considering the clamped trials where thickness is held at a constant  $h = 1$  mm, 34 trials are deemed as failures. All but one of these trials reach their respective rupture limit from Table 3.1. The additional trial (case H,  $\sigma_0 = 970$  MPa and  $Z = 0.4$ ) falls shorts of this limit ( $W_{\max} = 77.47$  mm per the current model), but is non-convergent in ANSYS [76]. From Fig. 3.5b, of the remaining 126 thinner plate trials, 36.5%, 65.1% and 83.3% of them respectively attain at most a 10%, 15% and 20% error. Moreover, 92.1% of trials are within 22%, while the maximum error for  $h = 1$  mm is 24.7%.

Briefly looking at the remaining charted data, in addition to showing the cumulative

distribution functions for constant thickness, Fig. 3.5b presents the effect of changing thickness and scaled distance, while maintaining the dynamic yield stress constant. Unlike in the simply supported trials, clamped plates with a high yield stress tend not to have a significantly more accurate solution than their lower strength counterparts as  $Z$  increases. This can be seen in Figs. 3.6b and 3.7a-b, and results in  $F_C(10\%) = 0.497$  and  $0.442$ , respectively, for  $\sigma_0 = 970$  MPa and  $\sigma_0 = 345$  MPa according to Fig. 3.5b. The  $F_C$  for clamped, high strength aluminum becomes lower than that for Al 2024-T3 for  $APE > 14\%$ . Comparing Figs. 3.5a-b, the top figure shows the cases where  $\sigma_0 = 970$  MPa to be the most precise (a high  $F_C$  for a low  $APE$ ), followed closely by those with  $h = 2.5$  mm. This relationship holds for about 63% of the trials. In contrast, the bottom figure depicts the  $\sigma_0 = 970$  MPa and  $h = 2.5$  mm curves about even until  $F_C \approx 0.3$ , after which, the two curves deviate with the latter producing more accurate results. Therefore, it appears that for the current clamped model, thicker plates generally tend to produce better results than stiffer plates. In particular, this claim does not hold for some small area and oblong plates with highly elastic deformation ( $1.2 \leq Z \leq 1.8$ ) per Figs. 3.6a and 3.7b.

Meanwhile, Fig. 3.6b shows that for large area plates (G, H), the average percent error remains fairly constant, between 12-15%, for all  $Z$ , regardless of thickness or yield stress. This consistency is also found for medium-sized plates (D, E, F), but the range drops to roughly an 8-12% error. For  $h = 1$  mm and  $Z \leq 0.8$ , the error exceeds these percent ranges for the larger plates, with a peak 22.3% average error at  $Z = 0.5$ . It should be noted that the zero error at  $Z = 0.4$  is due to all plates failing for such an intensive blast loading.

Moreover, Fig. 3.7a shows a large deviation for the square plate cases (A, E, H). Only the thicker and stiffer square plates for  $Z \geq 1.8$  produce an average error below 10%. As the uniform load acting on the entire large area square plate (H) causes large plastic deformation, it probably causes a large error between the current elastic-plastic, clamped model and the finite element output. As such, the deviations for the large plate overshadow some of the previously stated accuracy of the smaller square plate (A). However, the medium-sized  $300 \times 150$  mm cases (F) do not seem to adversely affect the average errors portrayed in Fig. 3.7b. Clearly, aspect ratio, independent of surface area, has an effect on the current model. Furthermore, it is interesting that for  $Z \geq 1.2$ , the thinner plate

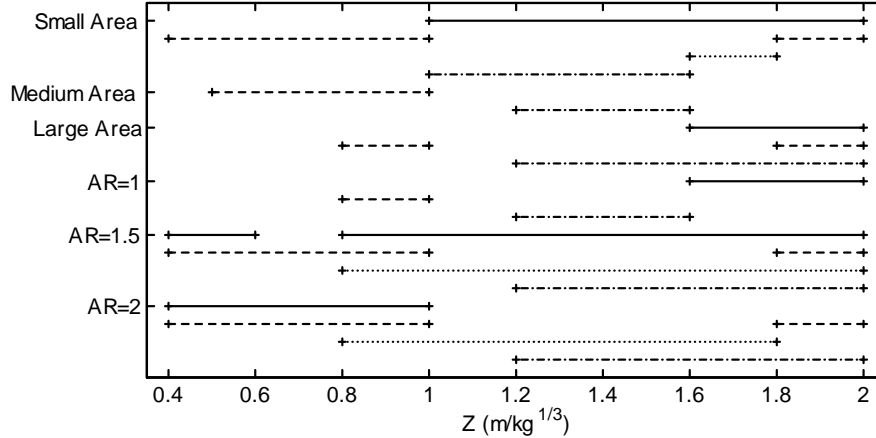


Figure 3.8: Ranges of validity for current clamped model with respect to plate size and aspect ratio (AR), where: —,  $h = 2.5$  mm and  $\sigma_0 = 970$  MPa; ---,  $h = 2.5$  mm and  $\sigma_0 = 345$  MPa; ····,  $h = 1$  mm and  $\sigma_0 = 970$  MPa; - · - · -,  $h = 1$  mm and  $\sigma_0 = 345$  MPa. These validity ranges depict where the current model is within 15% of the corresponding finite element solution for maximum deflection for all trials with the given parameter combinations.

trials produce a much smaller error than their thicker plate counterparts. For these higher  $Z$  values, errors for  $h = 1$  mm stay below 5%, while those for  $h = 2.5$  mm peak at the aforementioned 11.6%. This crossover between thickness curves in Fig. 3.7b can be attributed to there being a relatively high error for both the lower strength  $200 \times 100 \times 2.5$  mm plate and the higher strength  $300 \times 150 \times 2.5$  mm plate for  $Z \geq 1.2$ . These cases significantly underestimate and overestimate maximum deflection, respectively. These thicker plates with  $b/h < 100$  (see Ref. [57]) apparently do not act exactly like membranes for elastic-dominant response as is assumed.

Most of these trends are captured in Fig. 3.8. The validity ranges in this figure depict where the current clamped model is within 15% of the corresponding finite element solution for maximum deflection for all trials with the given parameter combinations. It is seen that the clamped model tends to have a larger range of applicability when plate area decreases and aspect ratio increases. The average absolute error between the maximum deflections from the current method and ANSYS [76] is 10.7%.

Finally, comparing the results attained from the current clamped model with that from

a rigid plastic model, just like for simple supports, the latter is generally more appropriate when the loading is extremely intensive (i.e.,  $Z \leq 0.5$ ). This results in about 16% of all clamped, rigid plastic runs showing a marginally better or similar result (within 2%) with regard to the current model. However, 64% of the rigid plastic trials show at least a 10% worse result than the current model, while roughly half are over 20% worse. As such, the current method's accounting for elastic effects is necessary for the vast majority of trials.

### 3.4.3 Permanent Deformation

For the baseline, clamped  $100 \times 100 \times 2.5$  mm plate, an entirely elastic response is seen for  $Z \geq 1.2$  when  $\sigma_0 = 970$  MPa. As  $Z$  increases, other dimensional cases also cease to plastically deform. However, due to the lack of a dissipation term in the relevant governing equations, permanent deformation cannot be attained by, for example, extending Figs. 3.4a-b until a final deflection is reached. As such, permanent central plate deflections for all dimensional cases are found using ANSYS [76] when  $Z = 1$  (small plastic deformation) and  $Z = 0.6$  (large plastic deformation without failure). These permanent deflections are then subtracted from the maximum deflections generated earlier by ANSYS [76] in order to determine appropriate  $C_e$  values per Eq. 3.31. This procedure attempts to verify the assertions made in Section 3.2.4 regarding elastic deflections.

Some representative parameter values for dimensional case B are given in Table 3.3. The lowest tabulated  $C_e$  value is 0.03 for  $Z = 1$ ,  $\sigma_0 = 970$  MPa and  $h = 2.5$  mm. This is expected per the discussion in Section 3.2.4 as a thick, high strength aluminum plate subjected to a low intensity blast would have very little plastic deformation. Likewise, there is little surprise that  $C_e$  increases with decreasing  $Z$ ,  $\sigma_0$  or  $h$  per Table 3.3. The largest values occur when these conditions are coupled, namely low strength with a either a thin plate ( $C_e = 0.83$ ) or a lower scaled distance ( $C_e = 0.63$ ). Furthermore, there is a weaker tendency for  $C_e$  to increase with increasing surface area. Again, this makes sense as a larger area equates to a larger net force, which, in turn, increases the amount of plastic deformation. Indeed, all values for  $C_e$  fall within the predicted range of  $0 \leq C_e \leq 1$ . This supports the claim that  $W_e$  is an upper bound of the elastic deformation.

Using these trends for obtaining  $C_e$ , permanent deformation can then be estimated from

$\mathbf{Z}$ (kg/m <sup>1/3</sup> )	1	1	1	1	0.6	0.6
$\sigma_0$ (MPa)	970	345	970	345	970	345
$\mathbf{h}$ (mm)	2.5	2.5	1	1	2.5	2.5
$\mathbf{W}_p$ (FE, mm)	0.967	5.14	5.71	18.72	6.499	16.52
$\mathbf{W}_{\max}$ (FE, mm)	5.408	7.052	10.06	19.23	10.52	17.35
$\mathbf{W}_{\max}$ (CM, mm)	5.083	6.332	8.901	16.44	9.208	16.07
$\mathbf{C}_m$	1.064	1.114	1.13	1.17	1.142	1.08
$\mathbf{W}_e$ (CM, mm)	4.582	2.217	5.178	3.004	4.584	2.219
$\mathbf{C}_e$	0.03	0.14	0.16	0.83	0.12	0.63

Table 3.3: Permanent deflection parameters for a clamped  $150 \times 100$  mm plate. FE denotes a result from finite elements, CM from the current method.

Eq. 3.31. While  $W_e$  in this equation is attained directly from the current method,  $W_{\max}$  can be multiplied by correction factor  $C_m$  to better match the maximum deflection per finite element analysis or, if available, that found through experiment. Considering all non-failed clamped runs, there is an average 10.7% absolute error between the maximum deflections from the current method and ANSYS [76]. Therefore, it is suggested that the  $W_{\max}$  found by the current method be multiplied by a correction factor of 1.107 in Eq. 3.31. This factor is close to the 1.116 calculated by averaging all  $C_m$  values in Table 3.3.

It should be stressed that the advantage of the current method is its computational efficiency. Accurate results for initial design are attained on the order of a thousand times faster than by finite element analysis. As such, the effects of various combinations of plate dimensions and material properties can be rapidly assessed, limiting the number of more detailed and time-consuming finite element runs that need to be processed in the next design stage. The correction factors in Eq. 3.31 serve to make the simple SDOF model output more realistic when actual data are available. However, their use is not required for this physically-based model. Adequate results are attained when  $C_m = 1$  and  $C_e = 0$  or 1.

### 3.5 Validation with Experimental Results

The current clamped method is now compared with some previously published experimental data for small, rectangular plates subjected to a uniform blast pressure. Langdon and Schleyer [10] examined  $500 \times 500 \times 1$  mm thick, clamped aluminum plates with a yield stress of either 95 MPa or 136 MPa. The uniform pressure load was roughly triangular

$\sigma_0$ (MPa)	95	95	95	136	136	136	136
$P_{\max}$ (kPa)	85	100	125	50	100	200	225
$W_{\max}$ (EX, mm)	–	–	–	–	14	25.1	38.8
$W_{\max}$ (CM, mm)	21.4	23.8	29.8	10.9	18.2	32.7	37.7
$W_{\max}$ (AN, mm)	–	–	–	–	17.8	F	F
$W_p$ (EX, mm)	12	18	22	0	10.5	23	F
$W_p$ (CM, mm)	14.1	16.5	22.5	2.2	9.42	24	28.9
$W_p$ (RP, mm)	20.9	24.5	30.7	8.5	17.1	–	–

Table 3.4: Comparison of dynamic maximum and permanent deflections for a  $500 \times 500 \times 1$  mm plate. EX denotes a result obtained experimentally [10], CM from the current method, AN analytically [10], RP from a rigid plastic model [10]. F denotes plate failure, – no data recorded.

and symmetric. However, the maximum pressure was varied between 50 kPa and 225 kPa, loading duration between 40 ms and 1 s. Of the three dynamic trials in Table 3.4 where maximum displacement was recorded, the high pressure results match very well with the current method ( $W_{\max} = 38.8$  mm experimentally,  $W_{\max} = 37.7$  mm for the current model, a 2.9% error). In contrast, there is a 30% overshoot for  $W_{\max}$  when  $P_{\max} = 100$  and 200 kPa. Still, the current method’s predictions are in line with that of Langdon and Schleyer’s more complicated analytical model, where stiff, translational springs simulate the clamped boundary condition, for  $P_{\max} = 100$  kPa.

As for permanent deflections, predictions by the current method are made by using the default values  $C_m = 1$  and  $C_e = 0$  in Eq. 3.31. For the low strength, experimental cases where  $W_p$  was recorded, there is good agreement with the current method. From Table 3.4, the two higher pressure cases show less than a 10% deviation, while the 85 kPa case has a 2.1 mm difference. Similar deviations are seen for  $\sigma_0 = 136$  MPa. Clearly, from Table 3.4, the current method’s results are much closer to the actual  $W_p$  values than the simple rigid plastic model provided in Ref. [10], where the ratio of maximum to static collapse pressure ( $p_c \approx 43M_0/b^2$  for a clamped square plate) approximates the deflection ratio  $W_p/h$ .

With few published experimental results for maximum and permanent deflections of rectangular aluminum plates available, the current method is also compared with the steel data of Refs. [71, 72]. Olson et al. [72] subjected  $89 \times 89 \times 1.6$  mm steel plates to uniform impulsive loads, assumed to have a rectangular time history with a  $15 \mu\text{s}$  duration. Applied impulses varied between 9.9 and 30.2 N·s.

As steel is highly strain rate-sensitive, the yield stress that enters Eq. 3.29 must be varied at each time step. This is accomplished by differentiating Eq. 3.30 with respect to time and inserting the result into the Cowper-Symonds relation, namely

$$\sigma_0 = \sigma_y \left[ 1 + \left( \frac{\dot{\epsilon}}{D} \right)^{1/q} \right], \quad (3.32)$$

where  $\sigma_y$  is the static uniaxial yield stress, and  $D$  and  $q$  are constants, all dependent on the plate material. Per Refs. [63,72],  $D = 40.4 \text{ s}^{-1}$  and  $q = 5$  for mild steel.

Once again using the default correction factors in Eq. 3.31, it is found that the current method matches only four of the fifteen permanent deflections presented in Ref. [72] within 10%. However, as two different failure modes are observed by Olson et al., namely large inelastic deformation (captured in the current model) and tearing at the supports, some plates exhibit a smaller permanent set with a larger applied impulse. Removing four such trials, the maximum error between the current model and the experimental profiles is 19.4%, while the average error is 11.5%. Setting  $C_m = 1.107$  per Section 3.4.3, these errors decrease to 10.3% and 4.3%, respectively. Assuming a rigid plastic model with  $C_m = 1$  and  $C_e = 1$ , the percent errors are bounded by the two previous results.

In an earlier study, Nurick et al. [71] performed blast tests on not just the same square plates as in Ref. [72], but also on  $113 \times 70 \times 1.6$  mm rectangular steel plates. Impulses for the square plates ranged between 8.7 and 16.6 N-s, resulting in only the large deformation failure mode. For the default, current square plate model, the maximum deviation is 15.6%, with an average error of 10.8% over 37 trials. Using  $C_m = 1.107$ , these errors drop to 9.6% and 3.1%, respectively. As expected, these values are slightly better than those for the more intensive blasts of Ref. [72], where elastic effects play a lesser role with  $W > b/6$  in nearly all trials.

Meanwhile, impulses for the rectangular plates of Ref. [71] varied between 5.2 and 17.4 N-s over 44 trials. These result in respective maximum and average errors of 28.4% and 18.4% when  $C_m = 1$ . Increasing  $C_m$  as above, these errors decrease to 20% and 10.5%, respectively. It is clear that these differences are much greater than for the square plate. There are two reasons for this trend. First, the strain rate obtained by differentiating Eq. 3.30 overestimates the global strain rate. This causes the transient yield strength to be

overestimated, which, in turn, underestimates the central plate deflection. It is found that the strain rate must be lowered to roughly 5% of its value per Eq. 3.30 in order to predict permanent deflection within an average 5% error for  $C_m = 1$ . For  $C_m = 1.107$ , the strain rate would need to be reduced to a more reasonable 40% to achieve the same accuracy.

Second, and more importantly, the oblong plates are subjected to pressures that are non-decaying and well above the plate's collapse load. In this instance, elastic effects (the first part of the current model) are low and the box shaped, plastic deformation pattern of Fig. 6.3 becomes more appropriate than the roof shape of Fig. 3.2 (the second part of the current model). For these reasons, the current model's applicability becomes questionable when dealing with strain rate-sensitive materials, particularly for non-square plates subjected to high pressure, impulsive loading. These concerns are further addressed in Section 6.2.

## Chapter 4

### Improvements to Explosive Loading Model

As stated in Section 2.5, most papers in the literature assume a uniform pressure distribution. However, such a distribution is only applicable for explosions having a sufficient standoff distance. Some papers do deal with more localized loading. For example, Wierzbicki and Nurick [79] detonated cylindrical PE4 charges of variable diameter 12 mm away from a 100 mm-diameter steel plate. The resulting impulse was shown to be nonuniform, both across the plate and within the footprint of the charge. Further, Lee and Wierzbicki [80] examined the effects of changing the impulsive loading profile on thin, square and circular plates, both analytically and numerically. The permanent deformed shape of the plates was shown to differ greatly between uniform and nonuniform rectangular and triangular loadings. In addition, Neuberger et al. [81] performed scaled experiments with spherical TNT charges in proximity to steel plates. A numerical model incorporating the pressure distribution of Eq. 4.1 matched the actual permanent plate deflections for various charge sizes and standoffs.

Simplified design methods for structures subjected to nonuniform blast loading are covered in technical manuals published by various U. S. government agencies [31, 38, 82]. The support manual for the program SBEDS [83] also collects these methods. The procedures listed within these manuals for dealing with nonuniform blasts are outlined below. Whenever possible, said procedures are supplemented with relevant research in the open literature and suggestions for improvement, which are incorporated throughout the remainder of this dissertation. In addition, some specialized topics, such as negative blast phase, pressure relief and TNT equivalence, are detailed in this chapter, along with potential discrepancies between published parameter data sets.

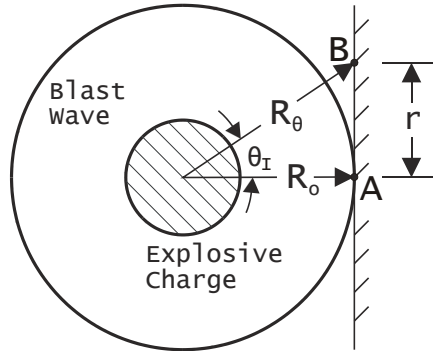


Figure 4.1: Geometry of an ideal blast wave impacting a flat surface.

## 4.1 Nonuniform Reflection

### 4.1.1 Pressure Distribution

From Fig. 4.1, assuming a spherical wave propagation, the blast wave reaches reference point  $A$  on the normal before it strikes point  $B$  some distance  $r$  away. For this case, point  $A$  is subjected to the same pressure-time history as described in Chapter 2 for a uniform load. In contrast, point  $B$  has a scaled distance  $Z = R_\theta/W^{1/3}$ , where  $R_\theta$  is termed the slant distance. Once  $Z$  is known, the procedure for determining  $p(t)$  at this arbitrary point on the target surface is essentially the same as detailed above for a uniform distribution across the surface with two exceptions, which pertain to incident angle and arrival time per Ref. [82].

First, one must account for the non-zero angle of incidence as reflected pressure tends to decrease as  $\theta_I$  increases. In this dissertation, the pressure at each point on the target surface is determined either by multiplying the calculated side-on pressure by a reflection factor per Fig. 4.2 or is found directly from

$$p(Z, \theta_I) = [P_r(Z) + P_o] \cos^2 \theta_I + K [P_s(Z) + P_o] (1 - \cos \theta_I)^2. \quad (4.1)$$

Here,  $K$  is a parameter introduced in this dissertation, set equal to 1 for the present discussion. From Ref. [23], it seems that using Fig. 4.2 is appropriate for a “free air burst,” where the blast wave only travels through air before reaching the target area. However, based on where this figure appears in Ref. [38], it may only be applicable for a surface burst, where

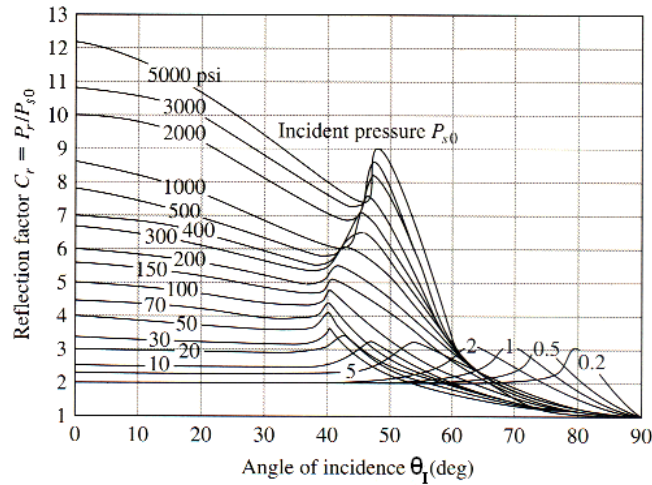


Figure 4.2: Reflection coefficient as a function of incident angle and pressure [23]. Note: 1 bar equals 14.504 psi.

a hemispherical blast of increased intensity reflects immediately off a surface, typically the ground. This latter limitation seems reasonable since the increase in reflection coefficient in Fig. 4.2 near  $40^\circ \leq \theta_I \leq 50^\circ$  is due to formation of a Mach stem, a coalescence of the reflected blast wave with a secondary incident wave [1]. Meanwhile, Eq. 4.1, which apparently ignores Mach effects, is explicitly given in Refs. [31, 81] and based on charts found in Refs. [31, 38, 82]. For completeness, both approaches mentioned are considered in this dissertation (see Section 4.4).<sup>1</sup>

An air burst is appropriate for the initial pressure loading due to a bare charge directly acting on the fuselage or within an empty luggage container (see Figs. 5.1 and 5.2). Meanwhile, a surface burst better models the case where reflections occur prior to impact with the target surface. For example, should the blast wave strike a piece of luggage or another panel of the luggage container before reaching the target surface, an amplification of pressure occurs as described in Section 2.4. As such, modeling an explosive blast as an air or surface burst tends to bound the actual pressure distribution.

<sup>1</sup>Per Ref. [82], there is also the intermediate case of an “air burst” (or “air burst above ground”), where the blast wave is reflected off the ground before reaching the target area, but not immediately. For clarity, throughout Chapter 4, the term “air burst” implies a free air burst, while “surface burst” implies a reflection before target impact, either immediate or delayed.

It should be noted that the curves in Fig. 4.2 can be made to fit Eq. 4.1 by changing the value of  $K$ . Indeed, setting  $K = 30$  makes for an extremely good fit for all  $P_s > 4$  bar (58 psi) and  $\theta_I \leq 40^\circ$ . This pressure range corresponds to  $Z < 1.5$ . Such a high value for  $K$  is justified in that the first term in Eq. 4.1 dominates the latter for low angles of incidence. Yet, as  $\theta_I$  increases, the high weighting factor allows for the quick-rising humps in Fig. 4.2. However, as these humps are also quickly-decaying,  $K$  must decrease as  $\theta_I$  continues to increase. Otherwise, Eq. 4.1 would greatly overestimate the actual pressure distribution.  $K$  achieves its maximum value of between 33 and 39 when  $40^\circ < \theta_I < 47^\circ$ . Meanwhile,  $K$  drops to about 20 at  $\theta_I = 50^\circ$  for  $P_s > 20$  bar. Over the range  $P_s > 4$  bar,  $5 \leq K \leq 12$  at  $\theta_I = 55^\circ$  and  $1 \leq K \leq 6$  at  $\theta_I = 60^\circ$ . For higher incident angles,  $K \approx 1$ , which reduces Eq. 4.1 to the form given in Refs. [31,81].

Additionally, unlike a planar wave, the arrival time of a nonuniform blast wave is different for each  $Z$  value across the reflecting surface. Arrival time can be determined per Fig. 2.3 or from the following equation provided by Kinney and Graham [3]:

$$t_a = \frac{1}{a_x} \int_{R_c}^{R_\theta} \frac{dr}{\sqrt{1 + 6P_s/7P_o}}, \quad (4.2)$$

where  $a_x$  indicates the ambient speed of sound ( $a_x = 340$  m/s),  $R_c$  the charge radius, and  $R_\theta$  the slant distance of the point of interest. The radical expression in Eq. 4.2 gives the Mach number  $M_x$  of a blast with a constant specific ratio  $\gamma = 1.4$ . Therefore, Eq. 4.2 is a simple reworking of the definition of shock front velocity (i.e.,  $u_x \equiv dr/dt = M_x a_x$ ). Moreover, it appears that a variable  $\gamma$ , as discussed in Section 2.4, does not result in any significant deviations from the  $t_a$  values calculated per Eq. 4.2.

Hence, as  $r$  increases, peak pressure decreases and blast arrival time increases. It should be clear that this procedure creates circular bands of equal pressure acting at equal times on the target surface. These bands can be seen in Fig. 4.3 for a 6 kg TNT charge detonated 0.5 m away from a plate. Beyond 0.92 m, zero pressure acts as the blast wave has yet to reach the outer parts of the plate after 0.25 ms. These circular bands are also seen in Ref. [84], which deals with the loading of laminated plates due to a mine blast. However, Coggin [84] limits the pressure profile to the range  $\theta_I \leq 45^\circ$ . For higher incident angles, he assumes the pressure reduces to zero, thereby ignoring most conflicts with the hump in

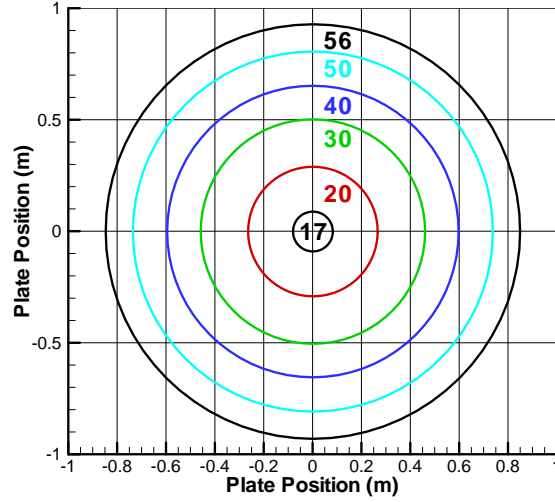


Figure 4.3: Circular bands of equal reflected pressure across a plate subjected to a centered 6 kg TNT charge with a 0.5 m standoff. Numbers indicate pressure in bar after 0.25 ms.

Fig. 4.2. In contrast, non-zero reflected pressures are calculated for  $0^\circ \leq \theta_I \leq 90^\circ$  in this dissertation. Indeed, using Coggin's procedure [84], all pressures greater than 30 bar would be removed from Fig. 4.3, thereby greatly diminishing the net impulse acting on the plate.

Another way of capturing a nonuniform pressure distribution was used by Turkmen and Mecitoglu [85], who compared analytical and finite element solutions for a plate struck with a pressure from a detonation tube. For a tube set 100 cm away from the  $9 \times 9$  cm laminated plate, the loading was essentially uniform. However, moving the shock tube within 35 cm resulted in a roughly sinusoidal pressure distribution. This distribution is approximated by modifying Eq. 2.1 as

$$p(t) = P_o + \left[ (P_m - P_c) \sin^2 \left( \frac{\pi x}{a} \right) \sin^2 \left( \frac{\pi y}{b} \right) + P_c \right] \left( 1 - \frac{t - t_A}{T_s} \right) e^{-\alpha(t - t_A)/T_s}, \quad (4.3)$$

where  $P_m$  is the maximum peak pressure acting at the plate center  $(a/2, b/2)$ , and  $P_c$  is the peak pressure acting along the plate edges. This waveform yields a pressure-time history having a similar trend as that in Fig. 4.4, with a discernible peak near the plate center. Equation 4.3 is referred to both in Sections 4.4 and 6.3 in the context of generalized loading shapes acting, respectively, on plates and shells.

### 4.1.2 Impulse Distribution

Just as a scaled distance-incident angle dependent pressure can be determined from Eq. 4.1, impulse for an oblique reflection can be calculated from

$$i(Z, \theta_I) = i_r(Z) \cos^2 \theta_I + i_s(Z) (1 + \cos \theta_I - 2 \cos^2 \theta_I), \quad (4.4)$$

as presented in Refs. [30,31]. Equation 4.4 is apparently applicable for both air and surface bursts since it correctly models both sets of curves given in Refs. [31,38,82].

Meanwhile, Henrych [22,44] suggests one assume a symmetrical triangular or trapezoidal impulse distribution for a prismatic charge detonated on a rigid surface. As a result, the blast wave pressure more realistically strikes the center of the target area before it reaches the edges. For a nearby explosion from a spherical charge (see Fig. 4.1), the impulse at a point can be estimated as

$$i = \frac{W(u_x + V_s)}{4\pi R_o^2} \cos^4 \theta_I, \quad (4.5)$$

where  $W$  is the charge mass,  $u_x$  is outburst speed, and  $V_s$  is the displacement speed of the outburst surface. For TNT, these speeds are provided as 6450 m/s and 7100 m/s, respectively.

This dissertation primarily uses Eq. 4.4 for impulse distribution. However, comparing the terms of Eqs. 4.1 and 4.4, it should be clear that the approximate relationship between side-on and reflected pressure and impulse given by Eq. 2.15 cannot be extended for all angles of incidence.<sup>2</sup> At small incident angles (i.e.,  $\theta_I \leq 20^\circ$ ), the side-on terms in the given equations are small compared to their reflected counterparts. Should blast pressure be well in excess of  $P_o$ , Eqs. 4.1 and 4.4 reduce to  $p(Z, \theta_I) = P_r \cos^2 \theta_I$  and  $i(Z, \theta_I) = i_r \cos^2 \theta_I$ , respectively, which are in keeping with Eq. 2.15. On the other hand, should  $\theta_I$  be continually increased beyond  $20^\circ$ , the side-on terms in Eqs. 4.1 and 4.4 start to become significant, much more so in the case of Eq. 4.4. In this case, the resulting relationships for distributed pressure and impulse no longer share a common multiplying factor.

---

<sup>2</sup>In other words, there does not exist a function  $C_r(\theta_I)$  such that  $p(Z, \theta_I) = C_r(\theta_I)P_s(Z)$  and  $i(Z, \theta_I) = C_r(\theta_I)i_s(Z)$  for all angles of incidence. Keep in mind that  $P_s$  and  $i_s$  in these expressions are calculated at an appropriate slant range and are, therefore, not necessarily at normal incidence.

The general procedure for calculating a nonuniform pressure distribution due to an air burst [82] can be summarized as follows:

1. For each point on the target surface, determine  $Z = R_\theta/W^{1/3}$  and angle of incidence  $\theta_I$ .
2. Use Figs. 2.3 and 2.7 to find values of  $P_s$ ,  $P_r$ ,  $T_s$  and  $t_A$  for the  $Z$  calculated in step #1.
3. Knowing  $P_s$ ,  $P_r$  and  $\theta_I$ , and assuming  $K = 1$ , use Eq. 4.1 to determine the net reflected pressure  $p(Z, \theta_I)$ .
4. Obtaining values of  $i_s$  and  $i_r$  from Fig. 2.7, evaluate the net reflected impulse  $i(Z, \theta_I)$  from Eq. 4.4.
5. Using  $T_s$  from step #2 and substituting the results of steps #3 and #4, respectively, for  $P_s$  and  $i_s$  in Eq. 2.2, numerically solve for exponential decay constant  $\alpha$ .
6. Again substitute  $p(Z, \theta_I)$  from step #3 for  $P_s$ . Insert this value along with  $T_s$  and  $t_A$  from step #2 and  $\alpha$  from step #5 into Eq. 2.1.

The resulting Friedlander waveform gives the pressure at a particular point on the target area for  $t_A \leq t \leq t_A + T_s$ . As the arrival time is different across the target, a pressure distribution similar to that shown in Fig. 4.4 is formed. In contrast, for a surface burst, the following procedure [82] is used:

1. For each point on the target surface, determine  $Z = R_\theta/W^{1/3}$  and angle of incidence  $\theta_I$ .
2. Use Fig. 2.3 to find the value of  $P_s$  for the  $Z$  calculated in step #1.
3. Knowing  $P_s$  and  $\theta_I$ , use Fig. 4.2 to determine the net reflected pressure  $P_r$ .
4. Obtaining values of  $i_s$  and  $i_r$  from Fig. 2.7, evaluate the net reflected impulse  $i(Z, \theta_I)$  from Eq. 4.4.

5. From Fig. 2.7, determine the  $Z$  value that corresponds to the  $P_r$  calculated in step #3. Call this scaled distance  $Z_p$ .
6. From Fig. 2.7, determine the  $Z$  value that corresponds to an  $i_r$  that matches the  $i(Z, \theta_I)$  calculated in step #4. Call this scaled distance  $Z_i$ .
7. From Fig. 2.3, determine the value of  $t_A$  that corresponds to the  $Z$  calculated in step #1.
8. From Fig. 2.3, determine the value of  $T_s$  that corresponds to  $Z = Z_i$ .
9. Using  $T_s$  from step #8 and substituting the results of steps #3 and #4, respectively, for  $P_s$  and  $i_s$  in Eq. 2.2, numerically solve for exponential decay constant  $\alpha$ .
10. Again substitute  $P_r$  from step #3 for  $P_s$ . Insert this value along with  $t_A$  from step #7,  $T_s$  from step #8 and  $\alpha$  from step #9 into Eq. 2.1.

The procedure for calculating the pressure distribution due to a surface burst appears to be much lengthier than that for an air burst. The differing  $Z$  values in steps #5-8 arise from the rationale that arrival time is directly related to pressure, and duration time is directly related to impulse [38, 82]. However, for the charge sizes and standoff distances considered in this dissertation  $Z_p \approx Z_i$  for all cases. Still, there appears to be a need for relationships that give  $Z$  as a function of  $P_r$ , as well as  $Z$  as a function of  $i_r$ . These relationships would theoretically be the inverse functions of Eqs. 2.4 and 2.6, respectively.

It should be noted that steps #5-7 presented here are modified from the procedure stated in Refs. [38, 82]. In these technical manuals, the  $P_r$  and  $i(Z, \theta_I)$  calculated in steps #3-4 are matched with their side-on, as opposed to their reflected, counterparts in Fig. 2.7 in order to determine  $Z_p$  and  $Z_i$ . Following this recommendation seems to doubly account for reflection. Moreover, for close-in explosions, the aforementioned  $P_r$  and  $i(Z, \theta_I)$  often exceed, respectively, the maximum values for  $P_s$  and  $i_s$  given in Fig. 2.7.

Furthermore, intuitively, the arrival time should depend only on the distance the explosion is away from the structure. For oblique incident angles, this distance increases by virtue of the slant range. Therefore, step #7 modifies the procedure recommended in

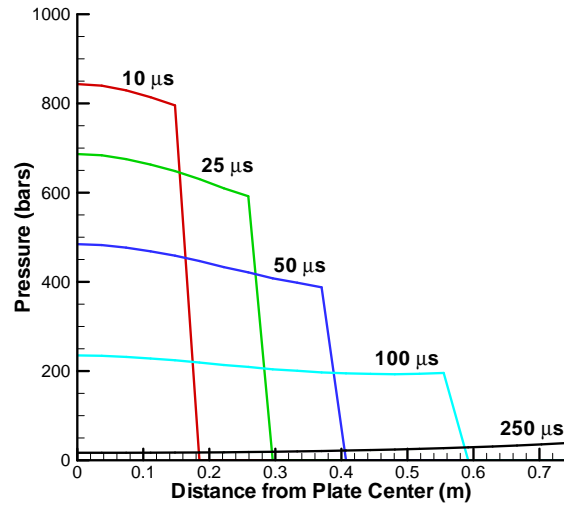


Figure 4.4: Reflected pressure distribution across a plate subjected to a centered 6 kg TNT charge with a 0.5 m standoff.

Refs. [38,82], which calls for transforming  $t_A$  to correspond with the  $Z_p$  determined in step #5.

### 4.1.3 Normalized Criteria for Assessing Applicability of Uniform Pressure Distribution

The procedures outlined above for computing a nonuniform pressure distribution can become quite time-intensive, particularly when dealing with small grid sizes. Yet, this procedure is at times necessary, as is the case for the distribution shown in Fig. 4.4. Here, a 6 kg TNT charge is detonated 0.5 m away from a plate. Clearly, a uniform pressure would severely overestimate the plate response, especially for the first 100  $\mu\text{s}$ .

Therefore, it is useful to determine when the standoff is large enough so as to assume a uniform pressure distribution. Surprisingly, no standard criterion was found in the open literature that addresses this issue. As noted in Section 2.5, the only stipulation for using a uniform distribution is that the explosion be far enough away from the target so as to produce a planar blast wave. Veldman et al. [8] verified such a wave in their experiments by measuring the arrival times across each test plate. Their measured deviations within 5%

indicated a nearly uniform distribution. Meanwhile, according to TM 5-1300 [82], a uniform loading can be assumed when the target is completely within the Mach stem of the blast wave. However, this criterion is more useful for buildings subjected to a far-off blast than for the close-in explosions of the current application. Furthermore, Ref. [83] suggests that a uniform load is adequate when  $Z > 1.2-2$ , but how this range was determined is unclear. From limited small-scale experiments using C-4 charges, Rickman and Murrell [86] estimate that a planar wave occurs near  $Z = 1.8$ .

Intuitively, the verification method of Veldman et al. [8] seems reasonable. A uniform loading can be used when the difference in arrival times across the target area is sufficiently small. As an example, for the case represented in Fig. 4.4, this difference should be well less than  $100 \mu\text{s}$ . This dissertation proposes a more mathematically formal, normalized arrival time criterion to determine when a uniform distribution can and cannot be used from a plate deflection standpoint. This criterion is defined as

$$t_A^* = \frac{\max(t_{Ai}) - \min(t_{Ai})}{T_{tar}}. \quad (4.6)$$

Here,  $\min(t_{Ai})$  and  $\max(t_{Ai})$  respectively indicate the minimum and maximum arrival time, while  $T_{tar}$  denotes the loading duration across the target area. For a charge centered about a plate, the minimum  $t_A$  is associated with the plate center. Meanwhile, the maximum  $t_A$  occurs at the farthest point from the charge, which would be any of the corners for a rectangular plate, or along the boundary for a circular plate.

As for  $T_{tar}$  in Eq. 4.6, it cannot always be determined so easily as it is found from the equation

$$T_{tar} = \max(t_{Ai} + T_{si}) - \min(t_{Ai}). \quad (4.7)$$

Here, the minimum  $t_A$  is again associated with the plate center. In contrast to the  $\max(t_{Ai})$  of Eq. 4.6, the expression  $\max(t_{Ai} + T_{si})$  does not necessarily occur at a corner or edge due to the kinks in the duration curve in Fig. 2.3, which were discussed in Section 2.2. Hence, for  $Z < 2$ , the quantity  $(t_{Ai} + T_{si})$  should be evaluated at all grid points on the target surface using Fig. 2.3 and the appropriate slant distance, with the maximum sum being inserted into Eq. 4.7. As standoff distance increases, the difference in arrival time across the target decreases. This means  $t_A^* = 0$  for a perfectly uniform load.

In Chapter 5, the arrival time criterion of Eq. 4.6 is compared with one minimizing the difference between uniform and nonuniform impulse, namely

$$i^* = i_{NU}/i_{UF}. \quad (4.8)$$

Here,  $i_{NU}$  refers to the total impulse acting on the target area using one of the procedures outlined in Section 4.1.2. This total impulse is the summation of the impulse at each point on the target area multiplied by the area over which that value acts. Therefore,  $i_{NU}$  has the more typical impulse unit of force multiplied by time (e.g., N·s). In contrast,  $i_{UF}$  is the total impulse associated with a uniform pressure. This value is calculated by simply multiplying  $i_r$ , as obtained from Fig. 2.7 for the scaled distance of the plate's center point, by the total plate area. Thus, the normalized impulse of Eq. 4.8 has an upper limit of  $i^* = 1$ , which is approached as the load becomes more uniformly distributed.

## 4.2 Specialized Effects

### 4.2.1 Negative Pressure Phase

As stated in Section 2.1, the negative phase of a blast pressure profile is usually ignored in a structural analysis. Its effects are generally minimal when dealing with rigid structures, such as those made from reinforced concrete. However, the negative phase can become important when dealing with flexible structures, where structural motion is affected by the phasing of blast loads acting across the target surface [38, 82]. According to Gantes and Pnevmatikos [87], who analyzed SDOF systems subjected to blast loads, the negative phase can possibly become important if it occurs during structural rebound, resulting in a maximum displacement which is opposite the direction of initial loading. Moreover, Dharani and Wei [88] have shown this phase to be significant for laminated glass panels.

As the structures of interest in the present application are lightweight aircraft structures, the negative blast phase is now briefly examined, albeit in a mathematical context. For close-in explosions, this pressure phase has hardly any effect on the structure, as evidenced by the small negative reflected impulse,  $i_r^-$ , relative to its positive phase analog at small scaled distances. For example, at  $Z = 0.1$ ,  $i_r^-/W^{1/3} \approx 4.9 \text{ bar}\cdot\text{ms}/\text{kg}^{1/3}$ , while  $i_r/W^{1/3} \approx$

218 bar·ms/kg<sup>1/3</sup> ( $i_r^-/i_r = 0.022$ ).<sup>3</sup> Indeed, the negative phase impulse does not even reach 20% of the positive phase value until  $Z > 0.36$ . This percentage increases to 50% for  $Z > 0.93$ . For the representative cases studied in Chapter 5,  $0.15 \leq Z \leq 1.1$ . This means that the negative phase is insignificant for most of the trials. For some of the smaller charge/larger standoff cases, this suction phase helps to slightly decrease the permanent plate deflection. However, it has no effect on maximum deflection as this critical value is reached well before the negative phase begins.

#### 4.2.2 Pressure Relief

Pressure relief occurs when the pressure acting on a structure is reduced from that calculated through the aforementioned procedures. This can happen in a number of ways. For example, the blast wave shown in Fig. 4.1 will continue to grow radially as it strikes the target surface. Once this wave propagation reaches the edges of the target, a rarefaction wave forms as the initial wave starts to go around structure. This rarefaction wave acts against any oncoming blast waves, thereby diminishing the total pressure acting on the structure (e.g., see Ref. [1]). This wave interaction makes it necessary to consider the time it takes for a blast wave to completely clear a structure. In a recent paper, Rickman and Murrell [86] discuss how conventional clearing time methodologies can be improved.

Furthermore, many times, an actual target is not completely rigid. This is particularly true of the aircraft structures considered herein. As the structure deforms, the incident angle of the blast increases. From Fig. 4.2 or Eq. 4.1, it is clear that pressure decreases as incident angle increases. Therefore, the blast wave-structure interaction prevents full reflection from occurring, thereby causing some relief of pressure. In this dissertation, this interaction effect is essentially ignored. As such, the calculated blast pressures herein are predominately higher than would be measured experimentally. Thus, the current approach is conservative, but much less so than one where all blast pressures are assumed to be uniform.

---

<sup>3</sup>The negative phase parameter data used here are obtained from figures in Refs. [38,82]. Some empirical equations for these parameters, which were developed by Brode, can be found in Refs. [17,19].

### 4.2.3 TNT Equivalence

The notion of TNT equivalence arises from the desire to collapse data from various explosive materials onto a single curve. Some sources (e.g., Ref. [20]) state that the ratio of release energies between a non-TNT and a TNT charge of equal mass defines the TNT equivalency. Therefore, pentolite, with a release energy ( $Q_x$ ) of 5110 kJ/kg, would have a TNT equivalency of 1.13, since  $Q_x = 4520$  kJ/kg for TNT [2, 19]. Ideally, if one is dealing with 1 kg pentolite charges, the associated blast parameters can be attained from Fig. 2.3, taking  $Z$  as the standoff distance in meters divided by  $1.13^{1/3}$ , or  $1.042$  kg<sup>1/3</sup>. In contrast, Bulson [22] states that a “standard” gram of TNT has a blast energy of 4610 J. Once again taking  $Q_x = 5110$  kJ/kg for pentolite, the resulting “standard” TNT equivalency is closer to 1.11. Moreover, as shown in Table 4.1, TM 5-1300 [38] gives a value of 1.09 for pentolite’s TNT equivalency.

Indeed, it is common to find different equivalence values for the same explosive. Discrepancies in respective energy values are, however, not the only cause of this nonuniformity. As outlined in TM 5-1300 [82], TNT equivalency depends not only on energy output, but also on material shape and pressure range considered (i.e., close-in or far-field). Esparza [34] experimentally showed that small charges at small standoffs produce different equivalencies than the accepted values in Ref. [82], which were developed mostly from large charges at large standoffs. Furthermore, Huntington-Thresher and Cullis [89] explain that the oxygen deficiency of most explosives results in some available energy being released during combustion, instead of completely during detonation. This after-burning phenomenon, also discussed in Ref. [35], accounts for different TNT equivalencies being given when considering pressure, which is related to initial detonation, and impulse, which depends on both detonation and combustion.

Still, since the cube root of these equivalency factors are eventually taken, the overall error of using one versus another is relatively low. Held [90] estimates the maximum error is between 3-10% for any explosive. Yet, compounded with other errors mentioned throughout this chapter, a 10% error could be significant. Table 4.1 provides TNT equivalency factors for some common explosives as measured by various criteria and given by numerous sources.

<b>Criterion [Ref.]</b>	<b>Composition B</b>	<b>C-4</b>	<b>Pentolite</b>
Energy [19]	1.148	–	1.129
Energy [38]	1.09	–	1.09
Pressure [4]	1.11	1.37	1.42
Pressure [19]	1.11	–	1.40
Pressure [23]	1.11	1.37	1.42
Pressure [34]	1.2	–	1.5
Pressure [82]	1.10	–	1.17
Impulse [4]	0.98	1.11	1
Impulse [19]	0.98	–	1.07
Impulse [23]	0.98	1.19	1
Impulse [34]	1.3	–	1
Various [3]	1.3-1.49	1.15-1.6	1.08-1.56

Table 4.1: TNT equivalency factors for common explosives from various sources.

While most experiments use either C-4 or pentolite, Composition B is included in Table 4.1 because its TNT equivalencies are easily found. Meanwhile, the explosive PE4, which was used in the small scale experiments of Refs. [79, 91], has TNT equivalencies similar to those of C-4.

With regard to Table 4.1, the values attributed to Esparza [34] were experimentally determined for small charges. Meanwhile, the values from Ref. [3] are based on various experimental tests, including ballistic mortar, plate dent and Trauzl block tests (see Ref. [92]). Koper et al. [42] used an average C-4 value of 1.3 based on this data [3] in their study, which examined both pressures and impulses of car bomb explosions. Moreover, Rickman and Murrell [86] claim that C-4 has a TNT equivalency of 1.27, but do not state on which criterion this is based. It is common, although incorrect, that single equivalency factors be used throughout such comparative studies.

In this dissertation, plate deformation is given as a function of  $Z$  value or the standoff distance of a given quantity of TNT. However, this discussion serves to illustrate possible sources of error in a commonly used approach. Additional problem areas pertaining to blast scaling are discussed in the next section.

### 4.3 Problems with Blast Scaling

In the last few sections, various assumptions incorporated within this dissertation have been stated. Additionally, some general problems related to modeling an explosive blast have been noted. These include neither having a standard criterion for applicability of a uniform pressure distribution, nor a standard measure of TNT equivalency. Meanwhile, issues like Refs. [3, 22, 23, 48] giving an improper upper bound for reflection coefficient were addressed in Section 2.4. Unfortunately, other modeling issues exist within the literature.

As stated in Ref. [38], “The actual values for the airblast parameters differ, of course, from one set of experimental or computational results to another. Consequently, one can obtain considerably different predictions of blast overpressures, impulses, and durations from different sources.” Indeed, as mentioned earlier, Refs. [1–4] yield data that are often inconsistent with one another and experimental results, particularly for close standoffs. Moreover, all of these references provide single curves for the aforementioned parameters. As a result, the scatter of the original test data from which they are based has been removed [38]. This section focuses on noting additional sources of error in published blast parameter data and assessing the level of uncertainty associated with these errors. This information is applied to the random blast loading of representative aircraft structures in Chapter 5.

#### 4.3.1 Variety of Scaled Distances

Thus far in this dissertation, the only scaled distance that has been used is  $Z$ , the ratio between standoff distance and the equivalent charge mass of TNT. This measure is given here exclusively in units of  $\text{m}/\text{kg}^{1/3}$ . However, there are a variety of scaled distances used in the literature.

In his compiled data plots, Baker [1] uses Sachs scaling [93], which, unlike Hopkinson-Cranz scaling [27, 28], takes into account the local atmospheric pressure and speed of sound. This scaling incorporates nondimensional units such as  $\bar{R} = RP_o^{1/3}/E^{1/3}$  for scaled distance, where  $E$  is the release energy of the charge. At low altitudes, Sachs scaling reduces to the more traditional Hopkinson-Cranz scaling when an equivalent mass of TNT is substituted for energy. However, Sachs scaling may be more appropriate at high altitudes [1]. An

airplane in flight typically reaches an altitude of 35,000 ft (10,700 m). However, according to Boeing [94], the cabin is pressurized so as to maintain the equivalent of ambient pressure at 8000 ft (2440 m). From an equation provided in Ref. [38], this translates to  $P_o = 10.9$  psi (0.75 bar), as opposed to the more standard 14.7 psi (1.01 bar). Therefore, a slight adjustment may be needed when considering an explosion during flight. Reference [38] estimates the maximum possible correction as 12%.

In addition, Goodman [32] uses charge radius  $X$  in place of scaled distance in his compilation of pentolite blast parameter data. This measure simply divides the standoff distance by the radius of the charge. Finding scaled distance in the U.S. customary unit  $\text{ft}/\text{lb}^{1/3}$  is also common. Conversely, some studies simply plot blast parameters as a function of stand-off distance. The trouble with all of these scaled (and sometimes unscaled) distances arises when trying to compile blast parameter data from various sources. Conversion factors, such as

$$1 \text{ m}/\text{kg}^{1/3} = 2.5208 \text{ ft}/\text{lb}^{1/3} = 0.282\bar{R} = 0.053X,$$

must always be kept in mind. Note that assuming standard atmospheric conditions allows these parameters, some dimensional and some nondimensional, to be equated.

### 4.3.2 Side-On Blast Parameters

Baker et al. [2] state that the experimental and numerical pressure data of various researchers significantly differ from each other. This is shown in Fig. 4.5, where, on average, the minimum and maximum pressures amongst the ten sources vary by a factor of two. This figure, which shows a data spread similar to that of the empirical  $P_s$ - $Z$  relationships in Fig. 2.5, uses the nondimensional scaled distance  $\bar{R}$  introduced in Section 4.3.1. Notice how, just as in Fig. 2.5, the logarithmic scaling of Fig. 4.5 tends to collapse dissimilar curves onto one another.

Chock and Kapania [95] give an example where the reflected impulses of Baker [1] and Kingery and Bulmash [30], from which the values in ConWep [4] are attained, deviate by over 40% for the same scaled distance. Meanwhile, the experimental results of Refs. [89,91] for small scale explosions also significantly deviate from the impulse and blast duration calculated by ConWep [4]. Moreover, Bogosian et al. [7] showed that there are at times

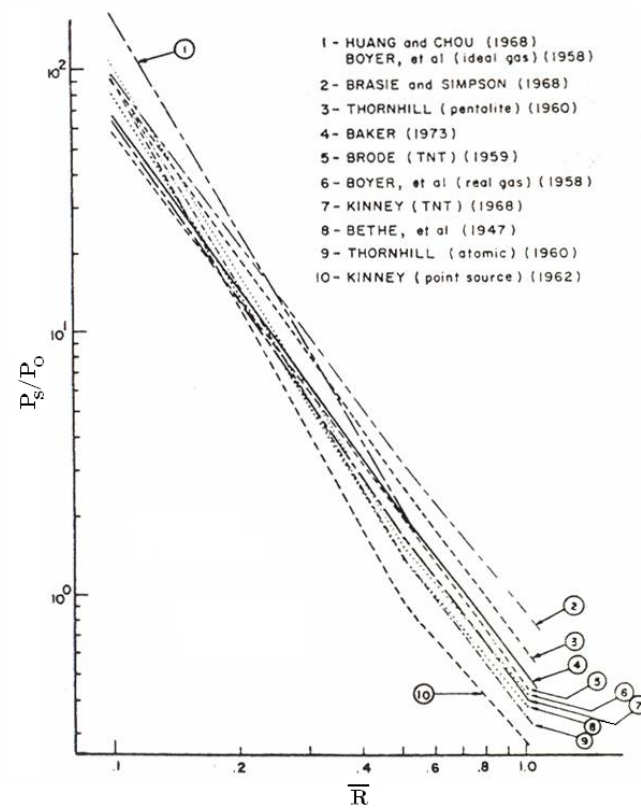


Figure 4.5: Side-on overpressure ratio  $P_s/P_o$  as a function of scaled distance  $\bar{R}$  from various experiments [2].

large discrepancies between ConWep [4], other computer programs, and experimental results with regard to both incident and reflected pressure and impulse. They suggest adding confidence bounds around the ConWep-generated curves to account for uncertainties in the compiled data set. Indeed, this is the approach adopted in Chapter 5 of this dissertation.

Huntington-Thresher and Cullis [89] performed experimental tests on 0.75 kg and 6 kg hemispherical TNT charges, along with PE4 and cylindrical TNT charges. They compared their resulting blast parameter data with that of ConWep [4] and the cAst-Euler hydrocode. They found that all sources produce similar values for peak pressure and arrival time. However, ConWep [4] displayed longer durations and higher impulses than the experimental and hydrocode measurements. As a result, Huntington-Thresher and Cullis [89] claim that blast scaling may only be applicable for  $0.7 \leq Z \leq 6.6$ . Furthermore, like Esparza [34], they provide TNT equivalencies less than the standard published values for 0.75 kg TNT charges, namely 0.8 and 0.7, respectively, for peak pressure and impulse.

As alluded to in Section 2.3, Eq. 2.6, taken from Ref. [3], does not correspond exactly with the impulses provided in Table XI of the same reference. This deviation is shown in Fig. 4.6. There is roughly a 19% difference in the curves for all  $Z < 1$ , and a 19-32% difference for  $Z > 3$ . The minimum error is about 4% at  $Z = 1.4$ . However, a deviation of at most 10% is only seen within the range  $Z = 1.1-2.1$ . It is preferable to use the tabulated values of impulse since the other blast parameters presented by Kinney and Graham [3] are consistent with these values (i.e., they satisfy Eq. 2.2).

Furthermore, Fig. 4.7 shows how these blast parameters [3] compare with those reported by Refs. [2, 4]. As already shown in Fig. 2.5, the side-on pressure values from these sources match extremely well for  $Z < 10$ . However, the impulse values are slightly greater for the Baker and ConWep data [2, 4], with the largest discrepancy occurring between  $0.5 < Z < 1.5$ . Meanwhile, the duration time data are completely divergent. The Baker and ConWep curve [2, 4] is generally increasing with scaled distance, save for the oscillatory behavior explained in Section 2.2. In contrast, the Kinney and Graham curve [3] begins with a value of  $T_s/W^{1/3} = 7.777$  ms at  $Z = 0.1$  before decaying to a minimum near  $Z = 0.5$ . Their curve then monotonically increases until it eventually matches the duration curve of Refs. [2, 4] at some  $Z > 10$ . It seems that Eq. 2.5, from which the Kinney and Graham

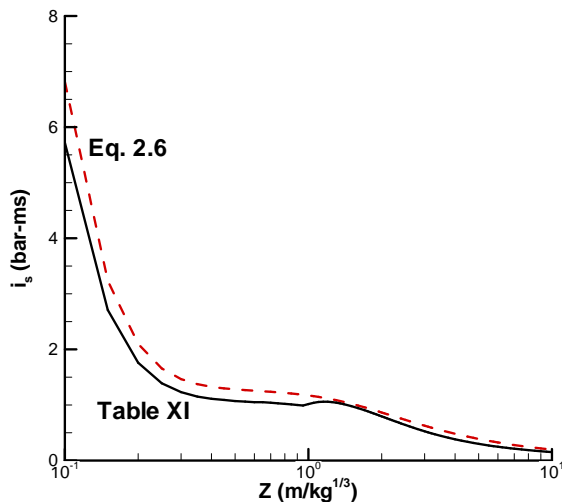


Figure 4.6: Deviation between side-on impulses reported in Table XI of Ref. [3] and via Eq. 2.6 for a chemical explosion.

duration curve is generated, is invalid for  $Z < 10$ . But as noted in Section 2.3, many studies make use of Eq. 2.5 within this  $Z$  range.

As stated above, the blast parameters of Kinney and Graham [3] are internally consistent. But if their duration time is greatly in error for the given  $Z$  range, so too must be at least one other parameter in Eqs. 2.1 and 2.2. Since pressure and impulse seem to be fairly reasonable in comparison to Refs. [2,4] per Fig. 4.7, that leaves only the exponential decay constant  $\alpha$  as a source of error. Indeed, Ismail and Murray [91] found that the time constant of Kinney and Graham [3] does not match their experimentally derived values for small PE4 charges.

### 4.3.3 Reflected Blast Parameters

In Section 2.4, it was assumed that the ratio of reflected and side-on values for pressure and impulse are approximately equal. However, upon first glance of Fig. 2.7, this does not appear to be the case, particular for the deflated impulse region when  $Z < 0.8$ . Indeed, for  $Z < 0.35$ ,  $i_r/i_s > 2P_r/P_s$ . But the impulse ratio decreases much faster than the pressure ratio, allowing  $P_r/P_s = i_r/i_s = 7.2$  near  $Z = 0.6$ . For higher  $Z$  values, the pressure ratio

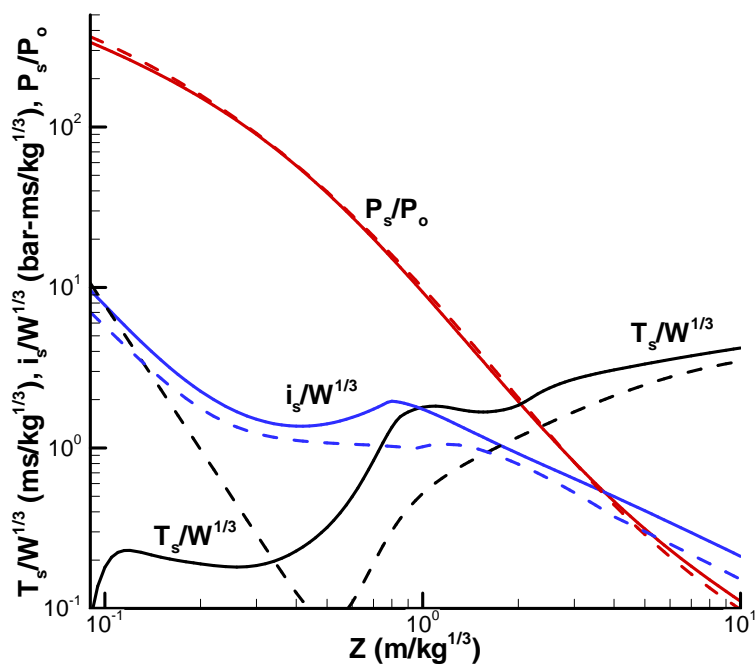


Figure 4.7: Side-on spherical blast wave parameters as a function of scaled distance: —, Refs. [2, 4]; ---, Ref. [3].

is much more dominant. As a result, the two ratios only come within 10% of each other again for  $4.25 < Z < 7.5$ . Since Eq. 2.15 is invalid, the reflected pressure distribution must be described by respectively substituting  $P_r$  for  $P_s$  and a reflected time constant for  $\alpha$  in Eq. 2.1, resulting in

$$p(t) = P_o + P_r \left(1 - \frac{t - t_A}{T_s}\right) e^{-\alpha_r(t-t_A)/T_s}. \quad (4.9)$$

Equation 4.9 assumes that the reflected arrival and duration times are equal to their side-on analogs per the discussion in Section 2.4.

It should be noted that reflected blast parameters such as  $P_r$  and  $i_r$  can be readily found in the literature. However, only Chock and Kapania [95] have provided values for the reflected time constant  $\alpha_r$ . Yet, as shown in Fig. 4.8, neither their side-on nor reflected parameter values match those calculated by the current author per data from Ref. [4]. In fact, the side-on curve of Ref. [95] corresponds better to the reflected curve of the present study, with these curves being coincident for  $1 \leq Z \leq 2$ . Moreover, the reflected time constant curve of Ref. [95] has the same oscillatory behavior as the solid  $\alpha$  curve in Fig. 4.8. Comparing the solid curves in Fig. 4.8 to each other, there is a large difference between  $\alpha$  and  $\alpha_r$  for  $Z < 3$ . A similar deviation is seen over the same  $Z$  range when comparing the two curves of Ref. [95] with each other. It should be made clear that ConWep [4] only explicitly provides a side-on decay constant. The reflected time constant is determined here by matching reflected impulse with the other blast parameters in an analogous procedure to that described in Section 2.1.

Furthermore, Fig. 4.8 displays side-on decay constant values as presented in Refs. [2,3]. As expected, the values from Baker et al. [2] compare fairly well with the ConWep data [4]. The Baker curve [2] also matches the limited time constant data tabulated by Smith and Hetherington [19] (not shown in Fig. 4.8). Moreover, the side-on curve of Chock and Kapania [95] is essentially the same as that plotted in Baker's earlier text [1], which was apparently corrected in Ref. [2]. Finally, the Kinney and Graham [3] curve, whose accuracy was called into question in Section 4.3.2, yields the lowest values of all those presented in Fig. 4.8. Their  $\alpha$  values only begin to approach those of the other studies when  $Z > 2$ . This result seems to verify Ismail and Murray's assertion [91] that Kinney and Graham [3] underpredict the decay rate for charges at small standoffs.

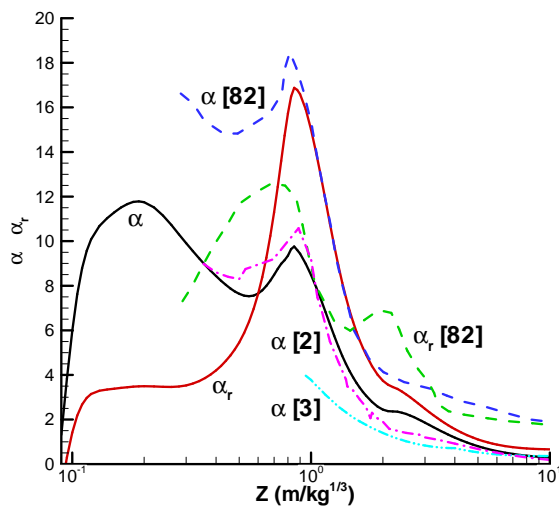


Figure 4.8: Side-on and normally reflected decay parameters as a function of scaled distance from various sources. Solid curves are derived by the current author from ConWep [4] data.

Whereas the results in Chapter 3 incorporated the side-on value of the decay constant, the trials from this point on make use of its reflected analog. Comparing the data in Fig. 4.8 with those in Table 3.2, there is probably only a significant change for three of the ten tabulated scaled distances, namely  $Z = 0.4, 0.5$  and  $1$ . The first two cases would tend to overpredict the decay rate using the Chapter 3 methodology, thereby underpredicting the load. Conversely, the latter case would tend to be conservative, overpredicting the pressure. However, the “underpredicting” trials when  $Z = 0.4$  or  $0.5$  are not really so since an overpredicting uniform load is also assumed in Chapter 3. Indeed, most of the plates in these low  $Z$  value trials fail despite the erroneous decay constant. In Chapter 5, less conservative and more realistic nonuniform loads are examined.

#### 4.4 Determination of Generalized Pressure Distribution

Figure 4.9 compares the two methods of determining nonuniform pressure-time history outlined in Section 4.1.2. The case shown is for a centered  $0.75$  kg TNT charge at a standoff of  $0.5$  m. There is no discernible difference between the curves for the first  $25 \mu\text{s}$ . As time is further increased, however, the surface burst curve exhibits an increased pressure relative

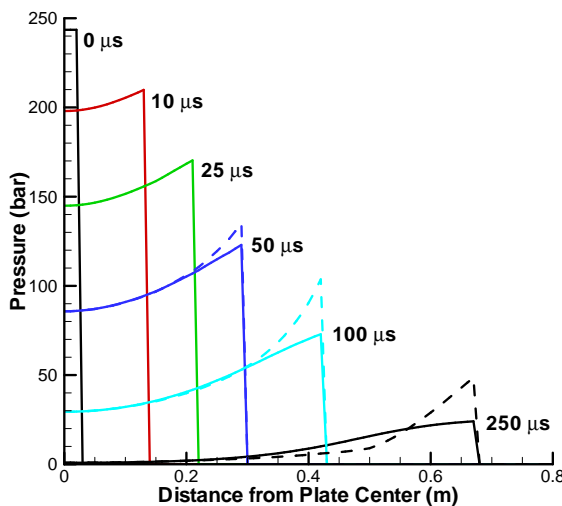


Figure 4.9: Reflected pressure distribution across a plate subjected to a centered 0.75 kg TNT charge with a 0.5 m standoff: —, air burst per Eq. 4.1; ---, surface burst per Fig. 4.2.

to that for an air burst near the blast wave front. This pressure increase away from the plate center is due to the pressure hump in Fig. 4.2. Still, from Table 4.2, the two methods (AB and SB) produce the same overall impulse for all given cases. This is due to the fact that both types of explosion are being modeled with Eq. 4.4 for net reflected impulse. So even though the pressure for the surface burst model rises above that for an air burst, the total area under the pressure time curve stays the same for the two models. This can be seen for the 250  $\mu\text{s}$  curves in Fig. 4.9, where the air burst has higher pressures closer to the plate center ( $r < 0.55$  m) before giving way to surface burst pressure for the smaller region  $0.55 \leq r \leq 0.67$  m.

Turning again to Table 4.2, using a modified air burst procedure also produces the same impulse as for the standard air burst. The two methods differ in their accounting for duration time. One calculates  $T_s$  per a  $Z$  value corresponding to the slant range for a standard air burst, while per a  $Z$  value corresponding to the net reflected pressure after Eq. 4.1 (i.e., similar to the surface burst procedure in Section 4.1.2) for the modified method. However, unlike for the curves in Fig. 4.9, the two airburst methods produce identical

$W_{TNT}$ (kg)	$R$ (m)	$I_{rel}$ (AB)	$I_{rel}$ (MA)	$I_{rel}$ (SB)	$I_{rel}$ (MC)
0.5	0.3	1	1	1	0.648
1	0.3	1	1	1	0.682
2	0.3	1	1	1	0.718
6	0.3	1	1	1	0.757
0.5	0.5	1	1	1	0.702
1	0.5	1	1	1	0.716
2	0.5	1	1	1	0.742
6	0.5	1	1	1	0.782

Table 4.2: Impulse comparison for various assumed pressure profiles, charge sizes and stand-offs. All values are scaled to those of air burst. AB denotes air burst, MA denotes modified air burst, SB surface burst, MC Mach cone.

pressure and impulse histories. As the three methods mentioned all produce similar, if not identical, pressure distributions for the given charge and standoff ranges, the simplest method to evaluate, namely that outlined in Section 4.1.2 for an air burst, is implemented throughout the remainder of this dissertation.

Meanwhile, the last column in Table 4.2 gives the relative impulse perceived within a Mach cone. This is the method that Coggin [84] implemented, which restricts pressure and impulse measurement to the region of the target area where  $\theta_I \leq 45^\circ$ . Intuitively, this method should become more accurate as standoff increases up until a limiting distance is reached. For a plate with a radius of 1 m, which is used in calculating the values in Table 4.2, this limiting distance would be  $R = 1$ , which corresponds to  $\theta_I = 45^\circ$ . Moreover, this table shows another trend in that the approximate method of Ref. [84] works better for larger charge sizes at a given standoff. This is a consequence of the larger charges producing an increasingly higher initial pressure and impulse at the plate center than for surrounding points as they are moved closer to the target. Therefore, the relative impulse of a larger charge is higher within a small incident angle, or more generally within  $\theta_I \leq 45^\circ$ . Still, for the given ranges, the Mach cone method should not be used as it greatly underestimates the total impulse as compared to the other tabulated methods. This approximation can potentially be used for a 6 kg charge at a slightly higher standoff distance than given in Table 4.2 (e.g.,  $R = 0.8$  m), when  $I_{rel} \geq 0.9$ .

Figures 4.4 and 4.9 both present reflected pressure data for a standoff of 0.5 m, but the former depicts the distribution from a charge eight times larger in mass. Whereas

the pressure curves in Fig. 4.4 are slightly decreasing with increased distance, in Fig. 4.9, pressure is distinctly increasing as the blast wave travels farther away from the plate center. Moving the 6 kg charge back to a standoff of 1 m, and therefore, to the same scaled distance as for the curves in Fig. 4.9, an upward swinging pressure distribution is also captured.

It appears then that there are a few different classes of pressure distribution. For far-off blasts (i.e., large  $Z$  values), there is the upward swinging nature of Fig. 4.9. Here, as the blast wave first reaches a point some distance away from the plate center, the pressure at the center has significantly decayed from its peak value. Geometrically, such a distribution can be generated by sweeping arcs from some large distance away.

In contrast, Fig. 4.10 shows the pressure distribution from a close-in blast, with the 6 kg charge moved to within 0.3 m of the target. These curves appear to be almost Gaussian in shape. Indeed, using the Gaussian equation

$$p(x) = \frac{p_{\max}}{\sigma\sqrt{2\pi}} \exp\left(-\frac{x^2}{2\sigma^2}\right) \quad (4.10)$$

supplied by Hoo Fatt and Wierzbicki [96], it is found that a near constant standard deviation  $\sigma$  of 0.2 holds for the 10  $\mu\text{s}$ , 25  $\mu\text{s}$  and 50  $\mu\text{s}$  curves. Therefore, the 6 kg charge exhibits a Gaussian pressure distribution for roughly the first 50  $\mu\text{s}$ . For intermediate blasts (e.g., a 6 kg charge at a standoff of 0.7 m), the pressure curves are nearly rectangular at early times, before transitioning to the upward swinging variety at longer times ( $t > 100 \mu\text{s}$ ). Comparing Figs. 4.4 and 4.10, although the profile shapes are significantly different, the wave front appears to reach equal distances in equal time. In other words, the horizontal propagation speed of the blast seems to be nearly constant for a given charge size, regardless of standoff distance.

Relatively few papers in the literature give geometrically defined pressure functions such as those described above. Collins [47] attempted to generate elliptical pressure waves from an explosion. While Collins [47] gives complicated mathematical functions for various parameters detailing the distribution, Turkmen and Mecitoglu [85] provide for a simpler sinusoidal distribution through Eq. 4.3. Moreover, the exponentially raised cosine expression of Eq. 4.5, which is attributed to Henrych [22, 44], can potentially be used to describe the early-time pressure distribution of a close-in blast.

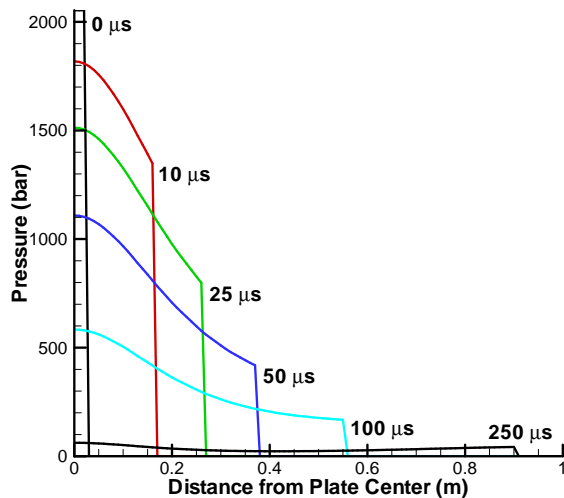


Figure 4.10: Reflected pressure distribution across a plate subjected to a centered 6 kg TNT charge with a 0.3 m standoff.

Additionally, Wierzbicki and Hoo Fatt [97] give a more general relationship, namely

$$p(x, \theta, t) = p_{\max} \exp\left(-\frac{t}{\tau}\right) f(x)g(\theta), \quad (4.11)$$

where the distribution is broken up into individual spatial and temporal components. Equation 4.11 can be used in conjunction with the modified Friedlander equation, like in Eq. 4.3, or also with the Gaussian form in Eq. 4.10 in order to develop a generalized, closed form pressure distribution. Such a distribution minimizes the use of redundant procedures like those outlined in Section 4.1.2. Furthermore, a closed form distribution is very useful when performing analytical calculations, or when developing a simplified loading/structural model as in the current application.

## Chapter 5

### Structural Response to Nonuniform Pressure Load

This chapter incorporates the structural model of Chapter 3, along with the procedures outlined in Chapter 4, in order to develop deflection curves of two representative aircraft structures.<sup>1</sup> These structures are numerically subjected to the explosive pressure from two small charges at a variable standoff. The panel deflections attained by calculating the appropriate nonuniform distribution are compared with those per an assumed uniform loading. Moreover, two different blast parameter data sets are examined.

The resulting parameter study serves to answer two questions. First, when can the pressure distribution acting on a structure be taken as uniform? Secondly, how can the uncertainty in published blast parameter data be assessed? The normalized response criteria of Section 4.1.3 and a Monte Carlo scheme are evaluated in order to respectively address these issues. Furthermore, the Monte Carlo method is also used to establish probability of failure curves for each representative structure.

#### 5.1 Method of Analysis

##### 5.1.1 Structural Model and Timestepping Scheme

The single-degree-of-freedom (SDOF) plate equations described in Sections 3.1 and 3.2 are again used throughout Chapter 5. For simplicity, all edges are considered clamped. This limits the required equations to Eq. 3.14 for elastic phase response, Eq. 3.20 for yield condition, and Eq. 3.29 for plastic phase response. As in Chapter 3, failure is based on a simple maximum strain criterion, namely Eq. 3.30.

---

<sup>1</sup>Chapter 5 represents an expanded version of work by Florek and Benaroya [98].

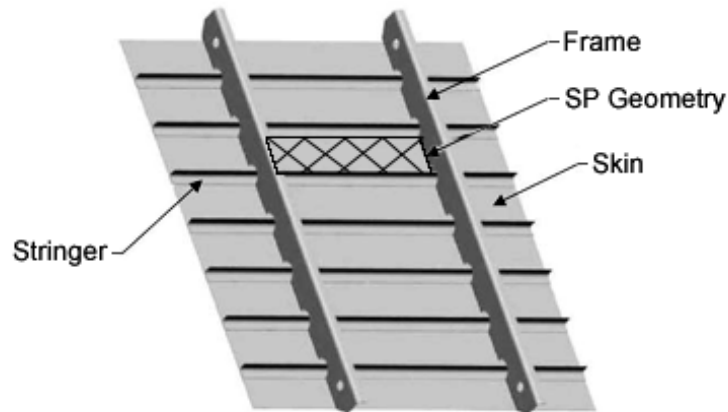


Figure 5.1: Small fuselage section with small plate (SP) geometry shaded [9].

Meanwhile, a Runge-Kutta scheme is again used to solve the above equations for deflection at every timestep. This procedure, as outlined in Section 3.3.1, can, in turn, be used to calculate the maximum deflection at the plate center.

### 5.1.2 Geometry and Material Properties

Two geometries are examined in this chapter. The first is a  $20 \times 8 \times 0.063$  in ( $508 \times 203 \times 1.6$  mm) Al 2024-T3 plate. This small plate (referred to as SP below) is representative of a small fuselage section between consecutive frames and stringers (see Fig. 5.1). As cited in Section 3.3.2, Al 2024-T3 has the following material properties:  $E = 73.1$  GPa,  $\nu = 0.33$ ,  $\rho = 2780$  kg/m<sup>3</sup> and  $\sigma_0 = 345$  MPa. The second geometry is a  $59 \times 57.5 \times 0.16$  in ( $1500 \times 1460 \times 4$  mm) Al 7021-T6 plate. This large plate (LP below) models a panel of an LD-3 luggage container, which is shown in Fig. 5.2. Per Ref. [75], Al 7021-T6 has the same Poisson's ratio and density as Al 2024-T3, with a slightly lower elastic modulus ( $E = 72$  GPa) and slightly higher yield stress ( $\sigma_0 = 380$  MPa). As in Chapter 3, aluminum is assumed here to be effectively strain rate-insensitive so that its static and dynamic yield stress are equal.

The maximum deflections are attained from the procedures in Chapters 3 and 4 for either a uniform or nonuniform pressure using the Matlab [74] programming language. These results are compared with output from the finite element package ANSYS [76]. In



Figure 5.2: LD-3 luggage container with large plate (LP) geometry in front [99].

ANSYS [76], the plate material is taken as bilinear–elastic, perfectly plastic (see Fig. 3.3), while the mesh again consists of square SHELL93 elements. Each finite element run on the Dell Precision 470, with  $0.1 \leq \Delta t \leq 1 \mu\text{s}$ , lasts roughly between 20 minutes and 2 hours, depending on the plate dimensions and whether or not the plate fails. Processing time is slightly increased from the 15-90 minutes cited in Chapter 3 due to the increased panel sizes and additional programming complexities associated with defining a nonuniform loading. Note that, unlike in Chapter 3, many of the current finite element runs are stopped short of achieving a steady state deflection. Meanwhile, with a required time step between  $1 \leq \Delta t \leq 5 \mu\text{s}$ , the corresponding deflection results from Matlab [74] still take only seconds to process.

The difference in results between the two computational methods is found to be generally less than 20%, with the highest errors occurring for the smaller panel (SP) cases. The figures throughout this chapter show Matlab [74] results after being multiplied by an appropriate correction factor ( $C_f$ ) to better match the finite element solutions. These correction factors, similar to those calculated in Section 3.4, are given in Table 5.1 for the various cases of this chapter. Values for  $C_f$  are based on a limited number of runs for each trial, consisting of a unique combination of charge size, reference source, distribution type and panel size.

$W_{TNT}$ (kg)	Ref.	UF/NU	$C_f$ (LP)	$C_f$ (SP)
0.75	[2,4]	UF	1.2	1
6	[2,4]	UF	1	1
0.75	[3]	UF	1	1
6	[3]	UF	1	1
0.75	[2,4]	NU	0.8	1.2
6	[2,4]	NU	1	1.2
0.75	[3]	NU	1	1.2
6	[3]	NU	1	1.2

Table 5.1: Correction factors to better match Matlab and ANSYS results. UF denotes uniform pressure, NU nonuniform pressure.

Standoffs range between  $0.3 \leq R \leq 5$  m. Note from Table 5.1 how most of the uniform runs per the current method do not require alteration based on the finite element data.

It should be noted that, in reality, the geometries presented in Figs. 5.1 and 5.2 have boundaries that are non-clamped. For example, the SP panel is constrained at its edges by the motion of the two frames and two stringers surrounding it. Typically, the frames will deflect a very small amount in comparison to the skin panel, so that two edges are, for practical purposes, clamped. In contrast, the stringers can deflect significantly under the action of a blast load. Each stringer, or the entire stiffened plate as per Refs. [100, 101], can be modeled as a beam. However, such modeling is beyond the scope of this dissertation. Moreover, assuming clamped edges allows for a better comparison with published experimental results related to the blast loading of plates (e.g., Refs. [11, 12, 72]).

### 5.1.3 Pressure Loading

Two sizes of spherical TNT charges are considered in this chapter—0.75 kg and 6 kg. These are the same charge sizes investigated by Huntington-Thresher and Cullis [89] in their small scale experiments. Henceforth, these spherical charges are respectively denoted as small charge (SC) and large charge (LC). Meanwhile, standoff distances range between 0.3 m and 1 m. The lower bound assumes that an explosive placed within a piece of luggage, either in an overhead bin (SP) or underneath the plane (LP), will be at least 0.3 m (roughly 1 ft) away from the target panel. Meanwhile, the upper bound is roughly the standoff for an explosive placed in the center of an LD-3 container, as per the experiments

of Gatto and Krznaric [102]. With the charge sizes and standoffs given, the calculated scaled distances vary between  $0.165 \leq Z \leq 1.1$ . These values are slightly lower than the range  $1.39 \leq Z \leq 1.75$  used by Akerman et al. [40] in their study of explosives in luggage containers.

As per the discussion of Section 4.1, a nonuniform pressure distribution is more appropriate than a uniform for a close-in explosion. However, both a uniform and centered nonuniform loading are examined in Section 5.2. This is done for two reasons. First, it is desired to compare the deflection results attained by using the blast parameters of Baker et al. [2] and ConWep [4], shown earlier to be nearly identical for  $Z < 10$ , with those calculated using values supplied by Kinney and Graham [3]. Secondly, comparing uniform and nonuniform results provides a means of evaluating the normalized criteria defined in Section 4.1.3.

Just like for the trials in Chapter 3, uniform pressures here are assumed to take on their fully reflected values. Whereas Refs. [2,4] provide both reflected pressure and impulse data to enable a reflected, uniform pressure distribution to be calculated per Eq. 4.9, Kinney and Graham [3] give only a means for calculating reflected pressures. With no details on the reflected impulse, Eq. 2.15 is used to generate the pressure distribution of Ref. [3]. Although shown to be in error in Section 4.3.3, Eq. 2.15 must be used due to lack of sufficient information. Therefore, this study also serves to quantify the error in predicted response when using Eq. 2.15 over a more exact relationship.

Moreover, as detailed in Section 2.4, the reflected pressures given by Kinney and Graham [3] are calculated through an unconservative reflection coefficient (see Fig. 2.6). From Fig. 4.7 though, their side-on pressure curve is essentially the same as that of Baker et al. [2] and ConWep [4] over the given  $Z$  range. As such, the reflected overpressures  $P_r$  for all models below are simply taken from Refs. [2,4]. These reflected pressure values are then inserted into Eq. 4.9. This procedure provides a much more reasonable impulse than would be otherwise assuming  $P_r/P_s \leq 8$ . In order to differentiate the models, the side-on values of  $T_s$  (from Eq. 2.5) and  $\alpha$  [3] (from Fig. 4.8) are used for the Kinney and Graham [3] curves below. In contrast, the curves for Refs. [2,4] below use  $T_s$  and  $\alpha_r$  from Figs. 2.3 and 4.8, respectively.

Meanwhile, nonuniform distributions for both models are generated per Eq. 4.1. As such, one should keep in mind the footnote in Section 4.1.2 regarding how nonuniform pressure and impulse distributions are determined. It should further be noted that the predicted pressures of Refs. [2, 4] begin to diverge significantly outside of the presented scaled distance range (i.e.,  $Z > 10$ ). However, for the charge sizes and standoffs used here,  $Z$  does not exceed this value, so the parameters of Baker et al. [2] and ConWep [4] are essentially the same.

Once the uniform or nonuniform pressure distribution is fully described, it can be used as input into the governing equations of the target geometry given in Section 5.1.1. However, in deriving Eqs. 3.14 and 3.29 for respective elastic and plastic phase motion, the pressure load  $p(x, y, t)$  was assumed to be uniform. This assumption effectively made  $p(x, y, t)$  a constant with respect to position, allowing it to be removed from any integral expression, thereby simplifying all derived expressions. In contrast, for a nonuniform pressure,  $p(x, y, t)$  must be integrated over an appropriate area. As a result, Eq. 3.14, for example, can be rewritten as

$$\rho h \ddot{W} + \frac{4Eh\pi^4}{27a^4(1-\nu^2)} \left( 3 + 2\frac{a^2}{b^2} + 3\frac{a^4}{b^4} \right) [h^2W + C_fW^3] = \frac{16}{9}p_{eff}(t), \quad (5.1)$$

where  $p_{eff}(t)$  is the effective uniform pressure load acting across the clamped plate, and all other parameters are as defined in Section 3.1. In Eq. 5.1,

$$p_{eff}(t) = \frac{16}{ab} \int_0^{b/2} \int_0^{a/2} p(x, y, t) \cos^2 \frac{\pi x}{a} \cos^2 \frac{\pi y}{b} dx dy. \quad (5.2)$$

For a simply supported plate,  $p_{eff}(t)$  is similar to that in Eq. 5.2, with  $\pi^2$  in place of 16 and the exponents on the cosine terms removed.

## 5.2 Comparison of Response to Uniform and Nonuniform Deterministic Load

### 5.2.1 Results of Deterministic Trials

In Fig. 5.3, the maximum deflection results for the LD-3 panel (LP) subjected to the blast from a 0.75 kg TNT charge (SC) are compared. Here, only the blast parameters of Baker et al. [2] and ConWep [4] are incorporated, but pressure distribution is assumed

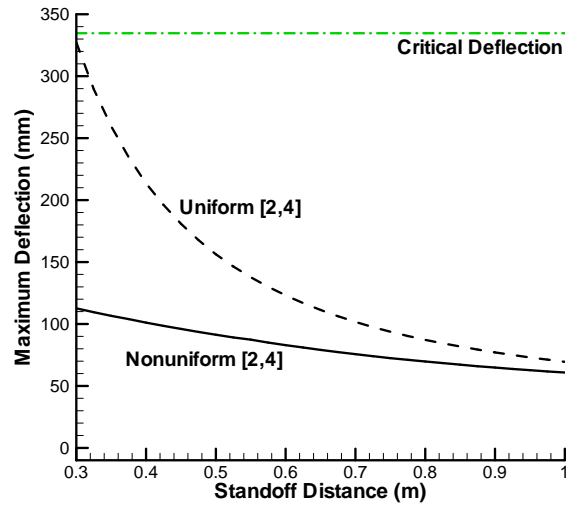


Figure 5.3: Comparison of maximum deflection results per Refs. [2,4] for an LD-3 panel (LP) subjected to uniform and nonuniform blasts from a 0.75 kg TNT charge (SC).

to be both uniform and nonuniform. The uniform distribution clearly produces a much greater deflection than its nonuniform analog for smaller standoffs. This is to be expected since the blast pressure is assumed to act over the entire plate simultaneously for a uniform distribution, while only over isolated sections for a nonuniform. As standoff distance increases, the two curves tend to collapse onto one another, with the uniform curve serving as an upper bound. It appears then that for this SC/LP case, a uniform distribution can be assumed for a standoff  $R > 1$  m, which translates to  $Z > 1.1$ .

There are a few other interesting features of Fig. 5.3. One is that the maximum deflection does not change appreciably over the given standoff distance range for a nonuniform distribution ( $60.8 \leq W \leq 113$  mm), especially when compared to the uniform deflections, where  $W_{\max} = 327$  mm. This seems to be a consequence of there being only a small change in total impulse (or effective uniform pressure) acting on the large area plate as standoff increases. For  $R = 0.3$  m, most of the nonuniform blast pressure is concentrated at the plate center. Analyzing Eq. 4.1, increasing the standoff (or  $Z$  value) has two major effects. First, the peak pressure striking the plate decreases. But simultaneously, points farther away from the center begin to feel significant pressures (see Fig. 4.3), thereby keeping the

net impulse relatively steady. As a uniform distribution acts over the entire plate, deflections are initially much higher. Since a uniform load is only governed by the first effect above, there is a sharp decay in net impulse, and therefore deflection, between  $0.3 \leq R \leq 0.6$  m. Despite these differences and the uniform maximum deflection being nearly triple that of the nonuniform distribution, neither model predicts a failure for  $0.3 \leq R \leq 1$  m (i.e., all deflections fall below the critical deflection of 335 mm calculated per Eq. 3.30). Clearly though, the LD-3 panel will fail for any smaller standoff per a uniform distribution.

In Fig. 5.4, the maximum deflection results from Fig. 5.3 are compared with those attained by using the blast parameter data of Kinney and Graham [3]. Meanwhile, Fig. 5.5 shows analogous curves for the case of a 6 kg charge (LC) acting on the LD-3 panel (LP). Whereas the uniform distribution curves of Refs. [2, 4] bound their corresponding nonuniform curves in these figures, Kinney and Graham's [3] uniform curves exhibit an odd behavior in that they fall below their associated nonuniform curves at certain standoffs. This dip occurs for  $0.4 \leq R \leq 0.6$  m in Fig. 5.4, for  $R \geq 0.85$  m in Fig. 5.5. These standoff ranges correspond to  $0.44 \leq Z \leq 0.66$ , which is approximately where the scaled duration curve of Ref. [3] reaches a minimum in Fig. 4.7. Therefore, a counterintuitive mathematical behavior is possible when the duration time is significantly changed. It appears that this is true even when pressure and impulse are essentially preserved.

In contrast to the plate behavior under a uniform load, the nonuniform load cases for Ref. [3] in Figs. 5.4 and 5.5 have no irregularities. Recall that for a uniform load, only single values of pressure, impulse and duration time are designated over the entire target surface, with an arbitrary arrival time usually set to zero. It is believed that the nonuniform distributions, which produce different arrival and duration times across the plate, smooth out the effect of fluctuations in the loading time. Indeed, these curves appear to have a near constant deflection value in the aforementioned figures, in large part, due to figure scaling. In actuality, the nonuniform deflections of Ref. [3] range between 64.7-70.5 mm and 167-201 mm in Figs. 5.4 and 5.5, respectively. Hence, deflections change very little over the range  $0.3 \leq R \leq 1$  m, and more importantly, do not exhibit an artificial dip like in the uniform cases. A similar, but less prominent, tendency for a dip in uniform pressure response occurs when the fuselage panel (SP) deflects per the data of Ref. [3]. This is seen

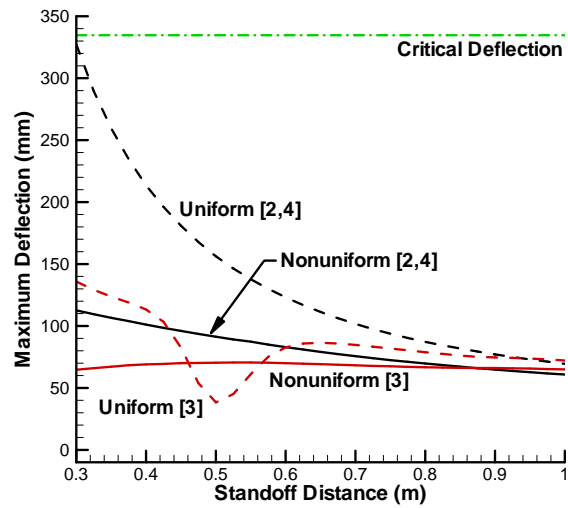


Figure 5.4: Comparison of maximum deflection results per Refs. [2-4] for an LD-3 panel (LP) subjected to uniform and nonuniform blasts from a 0.75 kg TNT charge (SC).

in Fig. 5.6 for the case of a small charge explosion.

Finally, it is clear from Figs. 5.4 and 5.5 that the Kinney and Graham data [3] predict maximum deflections that are well below the values per Refs. [2, 4]. This is an extremely important result since, as established in Chapter 2, the data from Refs. [2-4] are all commonly used in the literature. Such significant deviations in predicted deflection can severely alter a structural design, either conservatively or unconservatively. Indeed, in Fig. 5.5, the nonuniform curve of Refs. [2, 4] indicates failure for  $R < 0.75$  m; their uniform curve, for  $R < 0.95$  m. Therefore, assuming a nonuniform distribution, an additional design tolerance of 0.2 m (8 in) is gained. Similarly, for the SC/SP case shown in Fig. 5.6, an additional standoff tolerance of 0.15 m (6 in) can be gained. In contrast, Kinney and Graham's [3] deflections are entirely below their critical value for a nonuniform distribution in Fig. 5.5. For a uniform load, their deflections exceed the critical value only when  $R < 0.45$  m. These contrasting results make it unclear as to which data source should be used. This issue is examined further in Section 5.3.

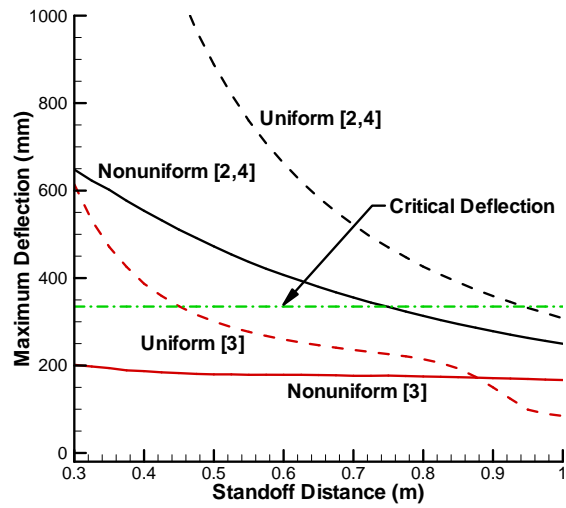


Figure 5.5: Comparison of maximum deflection results per Refs. [2-4] for an LD-3 panel (LP) subjected to uniform and nonuniform blasts from a 6 kg TNT charge (LC).

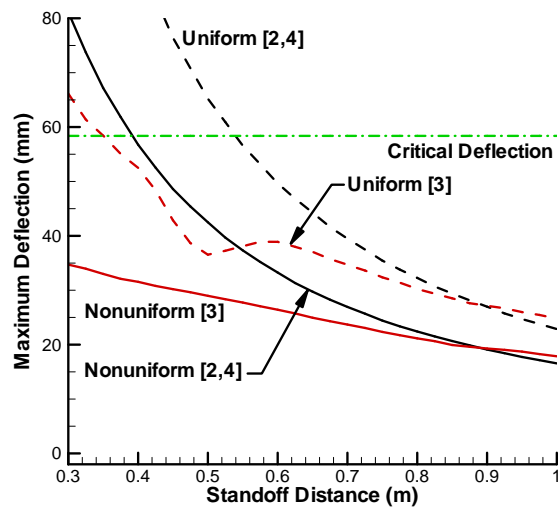


Figure 5.6: Comparison of maximum deflection results per Refs. [2-4] for a fuselage panel (SP) subjected to uniform and nonuniform blasts from a 0.75 kg TNT charge (SC).

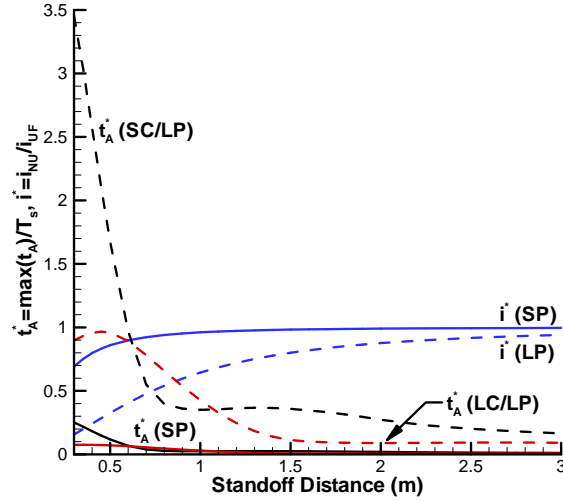


Figure 5.7: Normalized arrival time and impulse as a function of standoff distance, charge size and panel size.

## 5.2.2 Evaluation of Normalized Criteria

Figure 5.7 displays the normalized arrival time and impulse criteria introduced in Section 4.1.3. Per the conflicting results of Section 5.2.1, this figure incorporates only the data of Refs. [2, 4], which are used in the various technical manuals referenced in Chapter 4. As mentioned above, the uniform and nonuniform curves of Refs. [2, 4] for the SC/LP case appear to collapse onto one another near  $R = 1$  m (see Fig. 5.3). This means that a uniform distribution can safely be assumed for  $R > 1$  m. However, for the LC/LP shown in Fig. 5.5, these curves only begin to collapse onto one another at this maximum standoff. As such, Fig. 5.7 is extended to cover  $0 \leq R \leq 3$  m.

Plotting normalized impulse  $i^*$  against distance, a monotonically increasing function approaching unity over the given range is produced. In contrast, intermediate maxima are found in both LP  $t_A^*$  curves before they decay towards zero. This makes a unifying arrival time criterion less desirable for two reasons. First, a one-to-one correspondence between  $t_A^*$  and deflection does not exist. Secondly, some generality is lost in that the LP cases have completely different curves depending on charge size. But why do the  $t_A^*$  curves exhibit these behaviors? While not nearly as pronounced as the scaled duration time dip

<b>R</b> (m)	<b>W<sub>NU</sub></b> (mm)	<b>W<sub>UF</sub></b> (mm)	<b>% Error</b>	<b>t<sub>A</sub><sup>*</sup></b>	<b>i<sup>*</sup></b>
1	39.07	44.19	13.1	0.351	0.644
1.25	34.04	36.67	7.73	0.365	0.736
1.5	30.43	31.91	4.86	0.358	0.801
1.75	27.48	28.46	3.57	0.324	0.844
2	24.98	25.63	2.6	0.272	0.877
3	18.79	18.96	0.9	0.165	0.941
5	13.33	13.38	0.38	0.093	0.978

Table 5.2: Comparison of maximum deflection and normalized criterion values for SC/LP case.

for Ref. [3], there are still fluctuations in the corresponding curve of Refs. [2, 4] in Fig. 4.7. These oscillations affect the  $T_{si}$  values inserted into Eqs. 4.6 and 4.7, which, in turn, affect  $t_A^*$ . Moreover, the large values of  $t_A^*$  (i.e.,  $t_A^* > 1$ ) for the SC/LP case at small standoffs indicate that the time it takes for the small charge blast to reach the edges of the LD-3 panel is significantly greater than the duration time acting on the plate. Increasing the charge size decreases the corresponding arrival time and, therefore, decreases  $t_A^*$ . The resulting lack of a monotonically decreasing and general  $t_A^*$  curve for each geometry makes it difficult to establish a time based criterion for when a uniform distribution can and cannot be used. Meanwhile, the normalized impulse curves in Fig. 5.7 are not affected by either of these issues. Clearly, both the single SP and single LP curves monotonically increase to the maximum value of  $i^* = 1$ .

Table 5.2 displays the maximum deflection values attained by ANSYS [76] for both uniform and nonuniform loading of the LD-3 panel (LP) due to a 0.75 kg charge (SC). The percent errors of these deflections with respect to one another are also shown, and compared with both the normalized arrival time and impulse criteria. Meanwhile, Table 5.3 shows the same data for LD-3 panel subjected to pressures from a 6 kg charge (LC). Notice that the standoffs in Tables 5.2 and 5.3 are taken outside of the previous range  $0.3 \leq R \leq 1$  m. This is due to the fact that uniform and nonuniform deflections of the larger panel only begin to approach one another near  $R = 1$  m per the ConWep [4] parameter data.

For the SC/LP case, the uniform and nonuniform distributions produce deflections within 10% of each other when  $R > 1.1$  m. Meanwhile, the required standoffs for deviations of 5% and 2% are 1.5 m and 2.3 m, respectively. Interpolating the data in Table

$R$ (m)	$W_{NU}$ (mm)	$W_{UF}$ (mm)	% Error	$t_A^*$	$i^*$
1	164.3	201.5	22.6	0.427	0.63
1.25	123.9	138.8	12	0.214	0.726
1.5	97.15	105	8.08	0.113	0.793
1.75	79.57	84.44	6.12	0.093	0.839
2	66.92	70.2	4.9	0.089	0.873
3	42.36	43.38	2.41	0.092	0.94
5	26.59	26.76	0.64	0.051	0.977

Table 5.3: Comparison of maximum deflection and normalized criterion values for LC/LP case.

5.2, these three values of percent error respectively correspond to  $t_A^* = 0.359$ , 0.358 and 0.234. Further, the analogous values for normalized impulse are 0.67, 0.78 and 0.9. Scanning down the  $t_A^*$  column in Table 5.2, the aforementioned fluctuations in the normalized arrival time curve become apparent. The value for  $t_A^*$  increases between  $R = 1$  m and  $R = 1.25$  m, then consistently decreases as standoff increases.

From Table 5.3, a 10% error for the LC/LP case occurs when  $R = 1.38$  m, where  $t_A^* = 0.162$  and  $i^* = 0.76$ . Meanwhile, differences between the uniform and nonuniform maximum deflections decrease to within 5% near  $R = 2$  m, where  $t_A^* = 0.09$  and  $i^* = 0.87$ . A further decrease to a 2% error occurs when  $R = 3.4$  m,  $t_A^* = 0.082$  or  $i^* = 0.949$ . A similar fluctuation in  $t_A^*$  as for the SC/LP case is seen between  $R = 1.75$  m and  $R = 3$  m. Furthermore, comparing these  $t_A^*$  values with their analogous values for the SC/LP case, the numbers are quite different. For example,  $t_A^* = 0.358$  at a 5% error level for the SC/LP case, while  $t_A^* = 0.09$  at the same error level for the LC/LP case. Due to the confirmed fluctuations in the  $t_A^*$  curve and this lack of correspondence in  $t_A^*$  values for the tabulated cases, the normalized arrival time criterion in its current form is dismissed. Moreover, due to a similar lack of correspondence between the SC and LC cases, a  $Z$  value criterion, as proposed by Refs. [83, 86], also seems to be inadequate.

In contrast, it appears that normalized impulse values correspond fairly well between the two loading cases. A maximum 10% error is seen when  $0.7 \leq i^* \leq 0.76$ , a 5% error when  $0.78 \leq i^* \leq 0.87$  and a 2% when  $0.9 \leq i^* \leq 0.95$ , regardless of charge size. As a result, it is suggested that a uniform distribution can be substituted for a nonuniform pressure load when  $i^* > 0.9$ . This threshold also seems to give adequate results for the

smaller panel cases.

### 5.3 Response to Nonuniform Random Load

As explained in Chapter 4, uncertainties arise when using the loading model generated by the modified Friedlander equation (Eq. 2.1 or 4.9) and cube-root scaling law of Eq. 2.3. A primary cause for these uncertainties is that physically, two seemingly identical charges can produce significantly different pressure-time histories. As a result of this acute sensitivity to the numerous physical parameters involved, blast data from different sources tend not to match. As shown in Section 5.2.1, this lack of consistent blast data can cause a wide range of predicted deflections for a plate subjected to an explosive load. To account for this data randomness, uncertainties are introduced into the deterministic pressure model of Eqs. 2.1 and 4.9. The resulting probabilistic model allows for all deflection possibilities within the framework of the modified Friedlander equation to be considered.

#### 5.3.1 Monte Carlo Method

In Fig. 4.7, the scaled duration time and impulse curves of Refs. [2,4] differ from those of Ref. [3] over the entire plotted  $Z$  range. In contrast, the side-on pressure curves are essentially the same over the given range. As a result,  $P_s$  is considered here to be essentially deterministic for every  $Z$  value, while  $T_s$  and  $i_s$  are both taken as random variables. These random parameters are allowed to range anywhere between their respective lowest and highest values in Fig. 4.7 for a particular  $Z$  value. These parameter ranges are more clearly seen in Fig. 5.8. With no information on the type of scatter, simple uniform distributions are assumed to apply throughout.<sup>2</sup>

Deterministic reflected pressure  $P_r$  is simply found from Fig. 2.7. Moreover, each random  $i_r$  is determined by multiplying the random  $i_s$  from Fig. 5.8 for a given trial by the ratio of reflected to side-on impulse from Refs. [2,4] at that particular  $Z$  value. This is in holding with the discussion in Section 5.1.3. Furthermore, time constant  $\alpha_r$  is derived

---

<sup>2</sup>Here, a uniform distribution is in the probability sense of the expression, totally unrelated to a load being uniformly distributed as in Fig. 2.8. Consider a variable  $x$  whose lowest possible value is  $a$ , and whose highest is  $b$ . The variable is said to have a uniform distribution if for a given trial, there is an equal probability that  $x$  takes on any value within the range  $(b - a)$ . See Ref. [78] for more details.

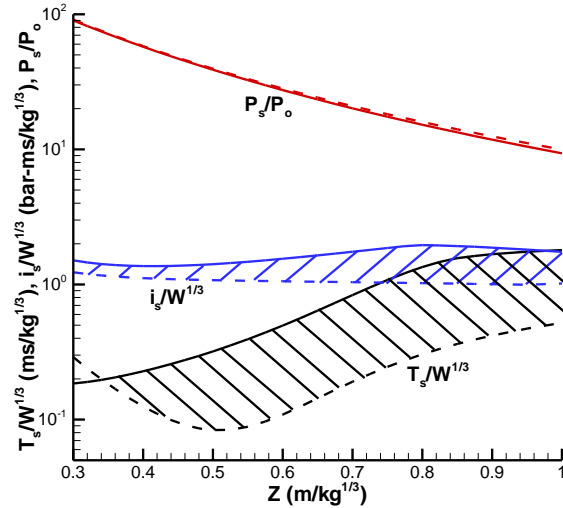


Figure 5.8: Blast parameter bounds for use in Monte Carlo simulation.

from these parameters (i.e.,  $P_r$ ,  $i_r$  and  $T_s$ ) for each trial as outlined in Section 2.1 (see Eq. 2.2). As only nonuniform pressure distributions are considered in this section, the air burst procedure given in Section 4.1 still applies for each trial.

As different maximum plate deflections are produced for each standoff (or scaled) distance depending on the values of the random loading parameters, the Monte Carlo method is implemented to attain a mean maximum deformation. This method works by running multiple trials at a given standoff (or scaled) distance until the average of the output deflections converges to some specified tolerance. Each resultant mean deflection has an associated standard deviation ( $\sigma$ ) at that particular  $Z$  value. For a normally distributed random variable, it is known that 68% of all data falls within one standard deviation of the mean, and 95% within two standard deviations. Although these percentages do not hold for uniform distributions, standard deviation bounds still serve as a measure of uncertainty. Indeed, Refs. [7, 72] use standard deviation bounds for non-normally distributed data.

Moreover, by defining a critical deflection, the Monte Carlo method can also estimate the probability of failure for a given standoff (or scaled) distance. This probability is simply calculated by dividing the number of trials that exceed the critical deflection by the total number of trials for a particular standoff (or scaled) distance. For more details on the

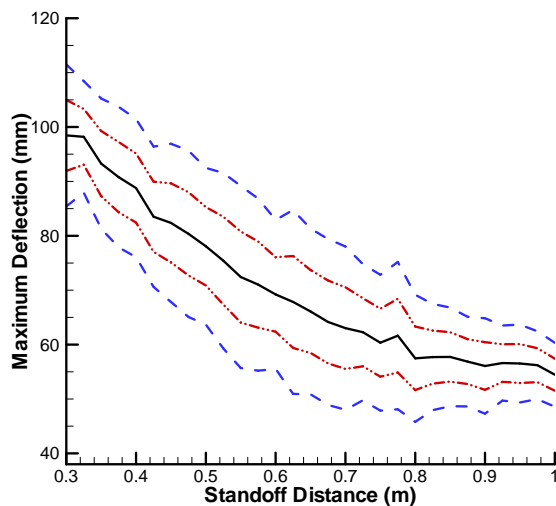


Figure 5.9: Maximum deflection for an LD-3 panel (LP) subjected to an SC blast: —, mean; · — ·,  $1\sigma$  bound; - - -,  $2\sigma$  bound.

Monte Carlo method and other topics related to probability and statistics, see, for example, the text of Benaroya and Han [78].

### 5.3.2 Results of Random Trials

The results for the LC/LP case of Fig. 5.5 are of particular consequence as the data set of Refs. [2, 4] predicts failure due to a nonuniform load for  $R < 0.75$  m, while that of Kinney and Graham [3] predicts no failure. This large variation in maximum deflection at the same standoff distance makes it necessary to assess the uncertainty in these calculated results. Using the Monte Carlo method, Figs. 5.9-5.11 are produced, where deflections correspond to an average of the nonuniform distributions of Refs. [2-4]. Comparing the results in Figs. 5.9 and 5.10 with the respective deterministic output in Figs. 5.4 and 5.5, it is clear that the mean deflection is weighted heavily towards the higher deflections of Refs. [2, 4]. Indeed, the upper two standard deviation ( $2\sigma$ ) bounds in Figs. 5.9 and 5.10 seem to match well with the maximum deterministic values of Refs. [2, 4].

A similar trend is seen when comparing the smaller panel (SP) case of Fig. 5.11 to its deterministic analog in Fig. 5.6. Meanwhile, a figure for the LC/SP case is not shown since

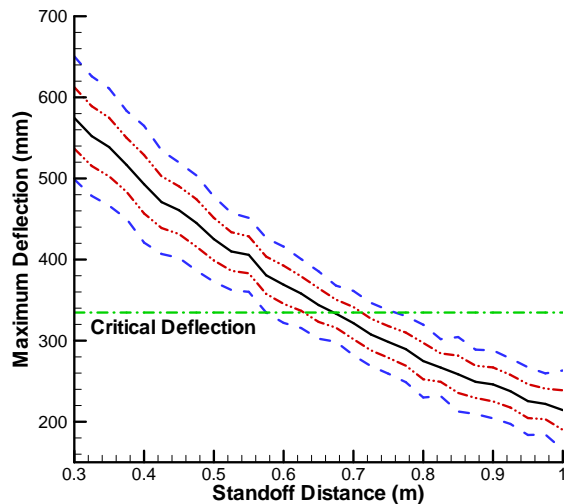


Figure 5.10: Maximum deflection for an LD-3 panel (LP) subjected to an LC blast: —, mean; · — ·, 1  $\sigma$  bound; - - -, 2  $\sigma$  bound.

failure is predicted for the entire standoff range. From Fig. 5.8, pressure is deterministic, while impulse is only slightly random. This means that only duration and the decay constant are significantly different between the models. The aforementioned results for the LP and SC/SP cases lead one to believe that the slightly higher impulse of Refs. [2, 4] in Fig. 4.7 has a much greater effect on maximum deflection than the longer duration time of Ref. [3] at close standoffs (i.e.,  $Z \leq 0.3$ ). This trend continues when the duration time of Ref. [3] becomes much smaller than that of Refs. [2, 4] for  $Z \geq 0.4$ .

### 5.3.3 Probability of Failure

Probability of failure results are only interesting for the cases shown in Figs. 5.10 and 5.11 as here, the critical deflection is crossed within the given standoff range. In the previous section, the curves for the LC/SP case were dismissed since failure is predicted for all standoffs  $0.3 \leq R \leq 1$  m. Likewise, the SC/LP case is ignored here as no failures are predicted within the same  $R$  range. It should be noted that the critical deflection lines in Figs. 5.3-5.6, 5.10 and 5.11 at 335 mm for LP cases and 58.4 mm for SP cases are all based on the assumed sinusoidal elastic shape. As mentioned in Section 3.2.3,

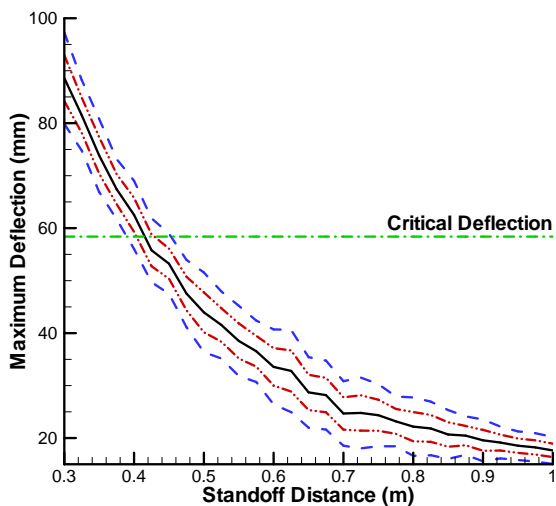


Figure 5.11: Maximum deflection for a fuselage panel (SP) subjected to an SC blast: —, mean; · — ·,  $1 \sigma$  bound; - - -,  $2 \sigma$  bound.

failure can also be related to the assumed plastic deformation pattern. As per Table 3.1, this failure criterion gives critical deflections roughly 9% higher than by the elastic shape. Both conservative ( $W_{re}$ ) and unconservative ( $W_{rp}$ ) rupture deflections are considered here in estimating probability of failure to a given load.

From its definition in Section 5.3.1, probability of failure is determined for the aforementioned cases and plotted in Fig. 5.12. For the LC/LP case, there are no failures for  $R \geq 0.9$  m per the elastic rupture model, all failures for  $R \leq 0.7$  m, and about a 61% chance of failure at a standoff of 0.8 m. For the unconservative model, these failure curves are roughly translated 0.15 m to the left. These probabilities, based on the applied parameter uncertainties, give a much more realistic measure of material behavior than the simple deterministic models used in Section 5.2.

Meanwhile, for the SC/SP case, there appears to be a 0% chance of elastic rupture for  $R > 0.45$  m, a 100% chance for  $R \leq 0.38$  m, and about an 80% chance at  $R = 0.4$  m. In contrast, a prevailing curve shift of 0.05 m for the fuselage panels means that there is nearly 0% probability of failure at  $R = 0.38$  m per the plastic rupture prediction. As neither rupture predictor gives a wide range between the limiting probabilities of 0 and 1,

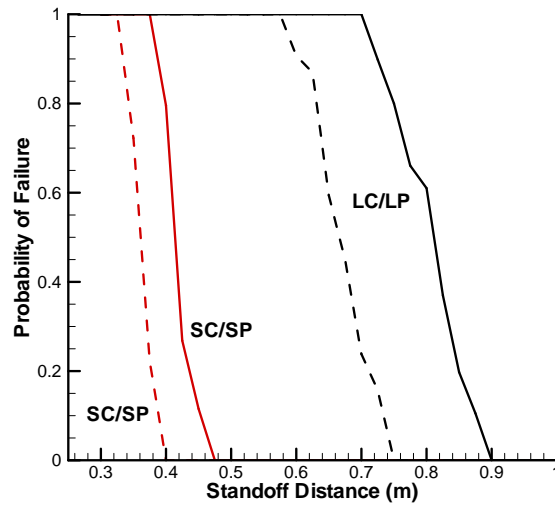


Figure 5.12: Probability of failure curves for SC/SP and LC/LP cases: —, per assumed elastic shape; ---, per assumed plastic shape.

the design should be such that a 0.75 charge cannot be placed within 0.45 m of the fuselage. Curves similar to those in Fig.5.12 can be generated by the designer for the particular charge size and standoff distance of interest.

## Chapter 6

### Improvements to Structural Model

As stated in Section 3.4, the average discrepancy between the current, clamped structural model and finite element results per ANSYS [76] is 10.7% for entirely uniform loads. However, when this model was extended for nonuniform loads in Chapter 5, average errors for both plate sizes reached upwards of 20% depending on the charge size.

This chapter offers some suggestions for improving the results furnished by the current structural model. First, the elastic phase model is examined. The exponent attached to the assumed clamped, elastic deflection shape is reevaluated, while the effects of adding terms to the equation governing this shape are explained. In addition, the roof shaped, plastic phase model is replaced by a more realistic box shaped pattern. Ways in which a nonuniform load can alter these elastic and plastic deflection shapes, as well as the phase transition between them, are also discussed. Other topics touched upon include structural damping and extending the current method of analysis to thin shells.

#### 6.1 Elastic Phase Structural Model

##### 6.1.1 Adding Terms to Fourier Series Expansion

The assumed elastic deflection shape defined in Eq. 3.4 for a simply supported plate is only a first-term approximation of the actual deformation profile. More generally, the transverse deflection can be represented by a Fourier series, namely

$$w = \sum_{m=1}^{\infty} \sum_{n=1}^{\infty} w_{mn} \cos \frac{m\pi x}{a} \cos \frac{n\pi y}{b}, \quad (6.1)$$

which captures higher order deflection modes. Clearly, each term of this infinite series satisfies the simply supported boundary conditions given in Section 3.1.2.<sup>1</sup>

Equation 3.12 for a clamped plate can similarly be written as an infinite series. The purpose of such expansions is to obtain a more realistic deformation shape, which better matches experimental and/or finite element results. However, with increased accuracy, the simplicity of the proposed first-order method is lost. The ideal solution will be a balance between accuracy and simplicity.

Recall from Section 3.1 that the assumed deflection shapes are inserted into Eq. 3.1, which yields expressions for  $\nabla^4 F$ . As derived in Ref. [6], the Airy stress functions themselves are obtained by matching similar cosine terms from this  $\nabla^4 F$  expression and satisfying the immovably constrained boundary conditions of zero displacement and shear stress in the plane of the plate (see Eqs. 3.7a-b). Once each  $F$  is determined, the respective equations of motion are generated by evaluating Eq. 3.2 and applying the Galerkin method. This procedure works fairly well with the one term deflection shapes of Eqs. 3.4 and 3.12. However, if multiple terms are retained from Eq. 6.1 or its clamped analog, a more systematic method is needed to generate the correct stress function.

Upon inspection, both expressions for the Airy stress function provided in Section 3.1, namely Eqs. 3.8 and 3.13, have the general form

$$F = Ax^2 + By^2 + \sum_{m=0}^N \sum_{n=0}^N g_{mn} \cos \frac{m\pi x}{a} \cos \frac{n\pi y}{b}, \quad (6.2)$$

where  $N = 2$  and  $g_{00} = g_{m1} = g_{1n} = g_{22} = 0$  for a simply supported plate, while  $N = 4$  and  $g_{00} = g_{m1} = g_{1n} = g_{m3} = g_{3n} = g_{44} = 0$  for a clamped plate. Per Levy [103], as more terms are retained for the simply supported deflection in Eq. 6.1,  $N$  in Eq. 6.2 increases towards infinity. Also from Ref. [103], constants  $A$  and  $B$  have a physical interpretation. They represent half the in-plane membrane pressures along the plate edges, commonly denoted as  $\bar{p}_y$  and  $\bar{p}_x$ , respectively.

Furthermore, Levy [103] provides expressions for coefficients  $g_{mn}$ . Unfortunately, these expressions are rather unwieldy. Here, these coefficients are obtained by applying the

---

<sup>1</sup>Equation 6.1 is usually given in Navier form (i.e., as a series of sine terms), which is applicable if the coordinate system of Fig. 3.1 is shifted so that the origin rests in the plate's lower left-hand corner.

method of Wang and El-Sheikh [104], who attempted to match  $\cos x$  and  $\cos y$  terms on both sides of Eq. 3.1 after inserting Eqs. 6.1 and 6.2, letting  $N \rightarrow \infty$ . Proceeding, Eq. 3.1 becomes

$$\begin{aligned} & \pi^4 \sum_{m=0}^{\infty} \sum_{n=0}^{\infty} \left( \frac{m^2}{a^2} + \frac{n^2}{b^2} \right)^2 g_{mn} \cos \frac{m\pi x}{a} \cos \frac{n\pi y}{b} \\ = & E \left[ \left( \frac{\pi^2}{ab} \sum_{r=1}^{\infty} \sum_{s=1}^{\infty} r s w_{rs} \cos \frac{r\pi x}{a} \cos \frac{s\pi y}{b} \right)^2 - \left( \frac{\pi^2}{a^2} \sum_{r=1}^{\infty} \sum_{s=1}^{\infty} r^2 w_{rs} \sin \frac{r\pi x}{a} \sin \frac{s\pi y}{b} \right) \right. \\ & \left. \times \left( \frac{\pi^2}{b^2} \sum_{p=1}^{\infty} \sum_{q=1}^{\infty} q^2 w_{pq} \sin \frac{p\pi x}{a} \sin \frac{q\pi y}{b} \right) \right]. \end{aligned} \quad (6.3)$$

Expanding the right side of Eq. 6.3 and eliminating all summation signs, which are implied by the indices,

$$\begin{aligned} & \left( \frac{m^2}{a^2} + \frac{n^2}{b^2} \right)^2 g_{mn} \cos \frac{m\pi x}{a} \cos \frac{n\pi y}{b} \\ = & \frac{E}{a^2 b^2} \left( r s p q w_{rs} w_{pq} \cos \frac{r\pi x}{a} \cos \frac{s\pi y}{b} \cos \frac{p\pi x}{a} \cos \frac{q\pi y}{b} \right. \\ & \left. - r^2 q^2 w_{rs} w_{pq} \sin \frac{r\pi x}{a} \sin \frac{s\pi y}{b} \sin \frac{p\pi x}{a} \sin \frac{q\pi y}{b} \right). \end{aligned} \quad (6.4)$$

This equation differs from the analogous Equation 10 of Wang and El-Sheikh [104], who expanded Eq. 6.3 with numerous extraneous terms. Using trigonometric identities, Eq. 6.4 is rewritten as

$$\begin{aligned} & \left( \frac{m^2}{a^2} + \frac{n^2}{b^2} \right)^2 g_{mn} \cos \frac{m\pi x}{a} \cos \frac{n\pi y}{b} \\ = & \frac{E w_{rs} w_{pq}}{4a^2 b^2} \left\{ r s p q \left[ \cos \frac{(r-p)\pi x}{a} + \cos \frac{(r+p)\pi x}{a} \right] \right. \\ & \times \left[ \cos \frac{(s-q)\pi y}{b} + \cos \frac{(s+q)\pi y}{b} \right] - r^2 q^2 \left[ \cos \frac{(r-p)\pi x}{a} - \cos \frac{(r+p)\pi x}{a} \right] \\ & \left. \times \left[ \cos \frac{(s-q)\pi y}{b} - \cos \frac{(s+q)\pi y}{b} \right] \right\}. \end{aligned} \quad (6.5)$$

Rearranging Eq. 6.5,

$$\begin{aligned} & \left( \frac{m^2}{a^2} + \frac{n^2}{b^2} \right)^2 g_{mn} \cos \frac{m\pi x}{a} \cos \frac{n\pi y}{b} \\ = & \frac{E w_{rs} w_{pq}}{4a^2 b^2} \left\{ (r s p q - r^2 q^2) \left[ \cos \frac{(r-p)\pi x}{a} \cos \frac{(s-q)\pi y}{b} + \cos \frac{(r+p)\pi x}{a} \cos \frac{(s+q)\pi y}{b} \right] \right. \\ & \left. + (r s p q + r^2 q^2) \left[ \cos \frac{(r-p)\pi x}{a} \cos \frac{(s+q)\pi y}{b} + \cos \frac{(r+p)\pi x}{a} \cos \frac{(s-q)\pi y}{b} \right] \right\}. \end{aligned} \quad (6.6)$$

Therefore, coefficients  $g_{mn}$  are of the form

$$g_{mn} = \frac{E}{4(m^2b/a + n^2a/b)^2} \sum b_{rspq} w_{rs} w_{pq}, \quad (6.7)$$

where  $b_{rspq}$  are coefficients that equate the  $\cos x \cos y$  terms on both sides of Eq. 6.6. As such,  $b_{rspq} = rspq - r^2q^2$  when  $r - p = \pm m$  and  $s - q = \pm n$  or when  $r + p = m$  and  $s + q = n$ . Furthermore,  $b_{rspq} = rspq + r^2q^2$  when  $r - p = \pm m$  and  $s + q = n$  or when  $r + p = m$  and  $s - q = \pm n$ . Otherwise,  $b_{rspq} = 0$ . It should be noted that these restrictions vary slightly from those presented by both Timoshenko and Woinowsky-Krieger [57] and Wang and El-Sheikh [104].

In general, as more terms are retained in Eq. 6.1 for the assumed deflection solution, there are more  $w_{rs}w_{pq}$  combinations with a non-zero coefficient  $b_{rspq}$ . As such, there are more  $g_{mn}$  values that would need to be calculated to satisfy Eq. 6.2 for the Airy stress function. For example, retaining only one term, namely  $w_{11}$ ,  $r = s = p = q = 1$ . Clearly, as  $rspq - r^2q^2 = 0$  and  $rspq + r^2q^2 = 2$ , only the second  $b_{rspq}$  cases need to be considered. The conditions  $r - p = \pm m$  and  $s + q = n$  are both true only when  $(m, n) = (0, 2)$ . Similarly,  $r + p = m$  and  $s - q = \pm n$  imply that  $(m, n) = (2, 0)$ . Therefore, the only non-zero terms in Eq. 6.2 are  $g_{02} \cos(2\pi y/b)$  and  $g_{20} \cos(2\pi x/a)$ , where, from Eq. 6.7,  $g_{02} = Ew_{11}^2 b^2/32a^2$  and  $g_{20} = Ew_{11}^2 a^2/32b^2$ . These values match those previously calculated in Eq. 3.8. In contrast, assuming  $w = w_{11} \cos(\pi x/a) \cos(\pi y/b) + w_{33} \cos(3\pi x/a) \cos(3\pi y/b)$  yields non-zero values for  $g_{02}$ ,  $g_{20}$ ,  $g_{06}$ ,  $g_{60}$ ,  $g_{24}$  and  $g_{42}$ .

### 6.1.2 Changing Exponent of Assumed Clamped Deflection Shape

In the previous section, a systematic method is presented for obtaining the Airy stress function corresponding to a multi-termed deflection shape of a simply supported plate. A similar method can be used for a multi-termed clamped solution. However, due to the squared cosine terms in Eq. 3.12, Eqs. 6.3-6.7 will all become more complicated. Even still, the addition of each term in the assumed deflection shape adds another equation of motion which needs to be solved (i.e., one equation for each mode amplitude  $w_{mn}$ ). The fact that these equations are coupled significantly adds to the level of difficulty of numerically solving them. Furthermore, this coupling reduces, to a certain extent, the engineer's ability

to gauge the physical response mechanism. Recall that this ability is a key advantage of using simplified analytical models in the first place.

As such, another approach is suggested here. Equation 3.12 is rewritten in the form

$$w = W(t) \cos^n \frac{\pi x}{a} \cos^n \frac{\pi y}{b}, \quad (6.8)$$

where central deflection  $W(t)$  replaces  $hf(t)$ , and the constant  $n$  replaces the exponent of 2. As mentioned in Section 3.1.3, choosing  $n = 2$  is rather arbitrary as any  $n > 1$  satisfies the clamped boundary conditions. In fact, it appears from Fig. 6.1, which is based entirely on results from the finite element software ANSYS [76], that choosing  $n = 2$  is highly in error. This figure plots the instantaneous exponent of Eq. 6.8 as measured at four points along the centerline of a 100 mm square, Al 2024-T3 plate subjected to a uniform pressure. In calculating this exponent  $n_{inst}$ , it must satisfy

$$w(x, t) = W(t) \cos^{n_{inst}} \frac{\pi x}{a}. \quad (6.9)$$

For early plate response in Fig. 6.1,  $|n_{inst}| < 1$  for distances less than 20 mm away from the plate center. This clearly differs from the mathematical prediction of a clamped boundary. Meanwhile, for distances greater than 20 mm from the plate center, the exponent varies between  $-2 < n_{inst} < 2$ . From Eq. 6.9, a negative exponent indicates that at a specific time instant, the deflection is not greatest at the plate center. It appears then that the assumed cosine squared deflection shape is inaccurate for  $t < 0.02$  ms, particularly near the plate edges.

As time increases to about  $t = 0.05$  ms, the deflections near the edges better match the assumed shape. However, intermediate points within 20 mm of the plate center exhibit a substantial deviation from Eq. 6.8, with  $n_{inst} = -2$  at  $x = 10$  mm. After roughly 0.07 ms, all exponent values tend to stabilize, oscillating between  $0.5 < n_{inst} < 2$ . It appears then that the assumed cosine squared deflection shape is also inaccurate across the plate for the steady state solution. A value of  $n_{inst} = 1.5$  better captures the global response behavior for  $t > 0.07$  ms.

As such, it is desired to generate an additional set of elastic, clamped plate equations, namely an equation of motion and yield condition, based on an exponent of 1.5 in Eq. 6.8.

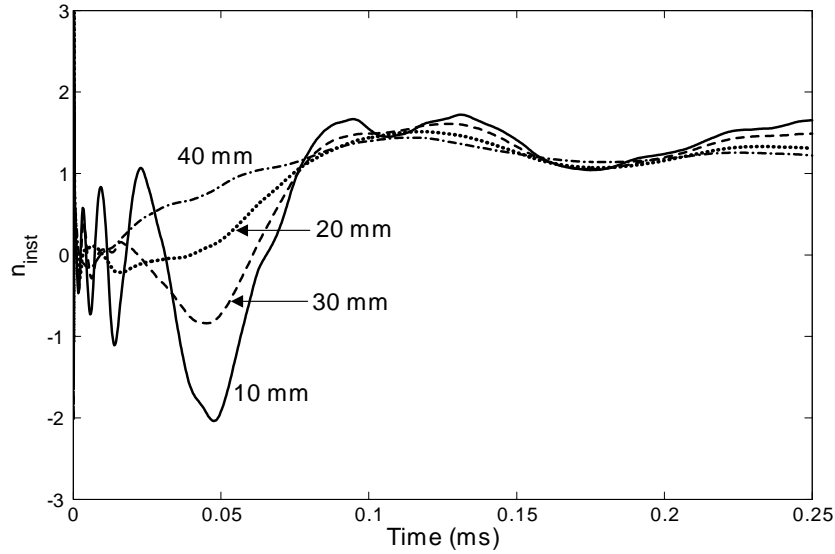


Figure 6.1: Finite element results for instantaneous exponent of Eq. 6.8 for a  $100 \times 100 \times 2.5$  mm Al 2024-T3 plate subjected to a uniform blast with  $Z = 1$ . Numbers indicate distance away from the plate center along the centerline.

Using the procedure of Section 3.1, which was outlined again in the previous section, the new assumed deflection shape is inserted into Eq. 3.1, which produces an expression for  $\nabla^4 F$ . Using trigonometric identities such as  $\cos^2 x = (1 + \cos 2x)/2$  and  $\cos 2x \cos x = (\cos 3x + \cos x)/2$ , this expression reduces to

$$\nabla^4 F = -\frac{9}{8}EW(t)^2 \frac{\pi^4}{a^2 b^2} \left( \cos \frac{\pi x}{a} \cos \frac{\pi y}{b} + \frac{3}{2} \cos \frac{3\pi x}{a} \cos \frac{\pi y}{b} + \frac{3}{2} \cos \frac{\pi x}{a} \cos \frac{3\pi y}{b} \right), \quad (6.10)$$

which implies that the Airy stress function is of the general form

$$F = C_1 x^2 + C_2 y^2 + C_3 \cos \frac{\pi x}{a} \cos \frac{\pi y}{b} + C_4 \cos \frac{3\pi x}{a} \cos \frac{\pi y}{b} + C_5 \cos \frac{\pi x}{a} \cos \frac{3\pi y}{b}. \quad (6.11)$$

Constants  $C_3$ - $C_5$  in Eq. 6.11 (or identically constants  $g_{mn}$  in Eq. 6.2) are obtained by matching similar cosine terms from Eq. 6.10. Note that Eq. 6.7 cannot be used since only a single mode shape is taken. With the various  $g_{mn}$  attained, the constants  $A$  and  $B$  in Eq. 6.2 (or  $C_1$  and  $C_2$  in Eq. 6.11) are calculated by satisfying the immovably constrained boundary conditions (i.e., by making Eqs. 3.7a-b equal to zero). However, it is found that there does not exist a set of constants  $A$ ,  $B$  and  $g_{mn}$  that satisfies all of the above requirements. As a result, an appropriate Airy stress function, and, therefore, an elastic

equation of motion and yield condition, cannot be determined. Hence, in order to improve the current, clamped plate response model, changes must be made to the pertinent plastic phase equations.

## 6.2 Plastic Phase Structural Model

In Chapters 3 and 5, Jones' roof shaped, rigid plastic plate model [63] was used to estimate the large deflection, plastic response of various representative aircraft structures subjected to an explosive loading. However, from Fig. 6.2, it appears that this model does not accurately represent the actual structural response of large panels. While a definite sinusoidal bowing is seen in this figure, which is captured in the elastic part of the current model, the four interior plastic hinges do not join at a fifth central hinge as in Jones' model [63]. Instead of a roof shape, the deformed panels take on more of a box shape. In this section, theoretical plate models based on this deflection shape are discussed.

### 6.2.1 Plate Displacements and Angular Velocities for Box Shaped Pattern

Figure 6.3 shows the geometry of a box shaped deformation pattern. This pattern differs from that in Fig. 3.2 by the presence of the flat, rectangular region III, formed by four additional, symmetric interior hinges. Note the change in dimensional nomenclature from Chapter 3 as  $2L$  replaces length  $a$  and  $2B$  replaces width  $b$ . The time-varying parameter  $B^*$  measures the vertical distance from either of the new  $x$ -spanning hinges to the closest lengthwise boundary. Meanwhile, from geometry,  $B^* \tan \phi$  gives the corresponding distance from either of the new vertical hinges to the nearest widthwise border. Clearly, when  $B^* = B = b/2$ , the four new interior hinges collapse into a single, central horizontal hinge, hence reducing the box shape to the previously discussed roof shaped pattern.

Similar assumptions to those stated in Section 3.2 are made here in extending the energy dissipation equations of Jones [63] for use with the box shape.<sup>2</sup> Using the upper right quarter of Fig. 6.3a as a reference, the plate deflections in the three regions are respectively

---

<sup>2</sup>Further details of the derivation of this model can be found in Ref. [6].



Figure 6.2: LD-3 luggage container deformed due to internal explosive loading [99].

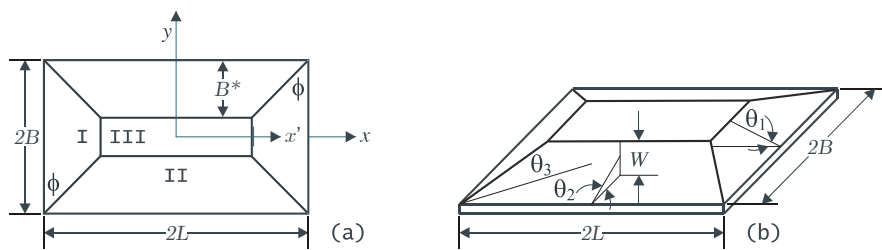


Figure 6.3: Box shaped deformation pattern: (a) plan view, (b) isometric view.

given by

$$w_I = W \left( 1 - \frac{x'}{B^* \tan \phi} \right), \quad w_{II} = W \left( 1 - \frac{y}{B^*} \right) \quad \text{and} \quad w_{III} = W. \quad (6.10a-c)$$

Differentiating Eqs. 6.10a-c gives the respective regional velocities. Per geometry and the discussion of Section 3.2, these velocities allow the angular velocities, namely

$$\dot{\theta}_1 \approx \frac{\dot{W}}{B^* \tan \phi}, \quad \dot{\theta}_2 \approx \frac{\dot{W}}{B^*} \quad \text{and} \quad \dot{\theta}_3 \approx \frac{\dot{W}}{B^* \sin \phi}, \quad (6.11a-c)$$

to be calculated.

### 6.2.2 Energy Relationships for Box Shaped Pattern

For convenience, the conservation of energy expression from Jones [62], previously given as Eq. 3.23, is restated as

$$\int (p - \mu \ddot{w}) \dot{w} dA = \sum_{m=1}^r \int (M + Nw) \dot{\theta}_m dl_m. \quad (6.14)$$

Here, it is once again assumed that in-plane displacements, velocities and accelerations are negligible. Also, only moderately large deflections (i.e.,  $W < B/3$ ) apply to ensure that  $Nw\dot{\theta}_m$  approximates the energy dissipation due to in-plane stretching.

The two terms on the left-hand side of Eq. 6.14 are now evaluated separately. Making use of Fig. 6.4 and assuming a uniform load, the external work rate is given by

$$\begin{aligned} \dot{E}_{ext} &= \int p \dot{w} dA = 4p \left\{ \int_0^{B^* \tan \phi} \dot{w}_I \left[ \frac{x'}{\tan \phi} + (B - B^*) \right] dx' \right. \\ &\quad + \int_0^{B^*} \dot{w}_{II} [y \tan \phi + (L - B^* \tan \phi)] dy \\ &\quad \left. + \dot{w}_{III} (B - B^*) (L - B^* \tan \phi) \right\}. \end{aligned} \quad (6.15)$$

The  $x'$  integral yields the work done on region I, the  $y$  integral that on region II, and the final term that on region III. As none of the terms are integrated over time,  $B^*$  acts as a constant. Therefore, the combined dissipation of the three regions is given by

$$\dot{E}_{ext} = 2p\dot{W} \left[ L(2B - B^*) - B^* \tan \phi \left( B - \frac{2}{3}B^* \right) \right], \quad (6.16)$$

after simplifying per Eqs. 6.10a-c. In developing Eqs. 6.15 and 6.16, a uniform distribution is assumed. For nonuniform loads, an equivalent uniform distribution can be defined for

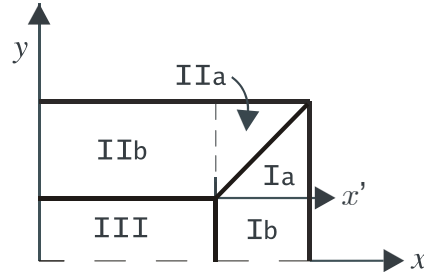


Figure 6.4: Upper right-hand quadrant of box shaped deformation pattern.

the plastic mode shape of Eqs. 6.10a-c as was done in Section 5.1.3 for the elastic deflection shape of a clamped plate.

Similarly, the inertial work rate is found from

$$\begin{aligned}
 \dot{E}_{inert} &= \int \mu \ddot{w} \dot{w} dA = 4\mu \left[ \int_0^{B^* \tan \phi} \left( \int_0^{x' \cot \phi} \ddot{w}_I \dot{w}_I dy + \int_0^{B-B^*} \ddot{w}_I \dot{w}_I dy \right) dx' \right. \\
 &\quad + \int_0^{B^*} \left( \int_0^{y \tan \phi} \ddot{w}_{II} \dot{w}_{II} dx' + \int_0^{(L-B^* \tan \phi)} \ddot{w}_{II} \dot{w}_{II} dx \right) dy \\
 &\quad \left. + \ddot{w}_{III} \dot{w}_{III} (B - B^*) (L - B^* \tan \phi) \right], \tag{6.17}
 \end{aligned}$$

where the first line contains the respective work contributions of regions Ia and Ib, the second line those of regions IIa and IIb, and the third line that of region III. Assuming only moderately large deflections, the accelerations in Eq. 6.17 can be approximated by merely twice differentiating the  $W$  terms in the deflection expressions of Eqs. 6.10a-c. Using these approximate accelerations, Eq. 6.17 reduces to

$$\dot{E}_{inert} = \frac{4}{3} \mu \ddot{W} \dot{W} \left[ L(3B - 2B^*) - B^* \tan \phi \left( 2B - \frac{3}{2} B^* \right) \right]. \tag{6.18}$$

Subtracting Eqs. 6.16 and 6.18 gives the left-hand side of Eq. 6.14. This expression is the box shaped analog of Eq. 3.24 for the roof shaped pattern.

Meanwhile, the right-hand side of Eq. 6.14, and thereby each boundary case's equation of motion, is determined as outlined in Section 3.2.2. However, the dissipation rates along the now eight interior hinges are calculated for a simply supported plate, plus along the four exterior hinges for a clamped plate. Balancing these dissipation rates with the work

rates of Eqs. 6.16 and 6.18, the following governing equations are found:

$$\begin{aligned} & \frac{\mu B^{*2}}{3M_0} \left[ \frac{2}{\beta^*} \left( \frac{3}{\gamma^*} - 2 \right) - \left( \frac{4}{\gamma^*} - 3 \right) \right] \ddot{W} + 4 \left[ \frac{2}{\beta^*} - 1 + \left( \frac{2}{\gamma^*} - 1 \right) \right] \frac{W}{h} + \frac{2}{3} \frac{h}{W} \\ = & \frac{pB^{*2}}{3M_0} \left[ \frac{3}{\beta^*} \left( \frac{2}{\gamma^*} - 1 \right) - \left( \frac{3}{\gamma^*} - 2 \right) \right]. \end{aligned} \quad (6.19)$$

for a simply supported plate, and

$$\begin{aligned} & \frac{\mu B^{*2}}{12M_0} \left[ \frac{2}{\beta^*} \left( \frac{3}{\gamma^*} - 2 \right) - \left( \frac{4}{\gamma^*} - 3 \right) \right] \ddot{W} + \left[ \frac{2}{\beta^*} - 1 + \left( \frac{2}{\gamma^*} - 1 \right) \right] \frac{W}{h} + \frac{2}{3} \frac{h}{W} \\ = & \frac{pB^{*2}}{12M_0} \left[ \frac{3}{\beta^*} \left( \frac{2}{\gamma^*} - 1 \right) - \left( \frac{3}{\gamma^*} - 2 \right) \right]. \end{aligned} \quad (6.20)$$

for a clamped plate, where  $\beta^* = B^*/L$ ,  $\gamma^* = B^*/B$  and  $\phi \approx 45^\circ$ . Just like Eqs. 3.28 and 3.29 for the roof shaped deformation pattern, Eqs. 6.19 and 6.20 are applicable only for deflections exceeding boundary condition dependent critical values ( $W = h/2$  for a simply supported plate,  $W = h$  for a clamped plate). In the present application, this point is moot in that these critical values are always reached during the elastic phase.

It is clear by comparing Eqs. 3.28 and 3.29 with Eqs. 6.19 and 6.20 that the presence of a central deflection region further complicates the respective equations of motion. Indeed, whereas the former set of equations contains only one unknown ( $W$ ), the latter set has two unknowns ( $W$ ,  $B^*$ ). Therefore, at least one additional equation involving  $W$  or  $B^*$  must be defined in order to solve for all unknowns at a given time. In Ref. [6], it is suggested that the moment balance equations of Yu and Chen [64] be used for this purpose.

### 6.2.3 Additional Equations of Motion for Boxed Shaped Pattern

Yu and Chen [64] provide their own equations of motion for the box shaped profile. Instead of using an energy balance to derive these equations, they base theirs on a simple force and moment balance. Doing so allows them to calculate an initial value for the  $B^*$  equivalent  $\delta a$ , and track the parameter, amongst others, using a Runge-Kutta timestepping procedure.<sup>3</sup>

---

<sup>3</sup>Yu and Chen [64] use  $b$  and  $a$  to respectively represent length and width in their plate analysis. This is opposite to the designations used in Fig. 3.1. So as to not create too much confusion, the nomenclature from Fig. 6.3 (i.e.,  $2L$  for length and  $2B$  for width) is used throughout the remainder of Section 6.2. Yu and Chen's designations [64], however, are utilized in Appendix C.

For large deflections of a plate uniformly loaded by a pressure  $P(t)$ ,<sup>4</sup> Yu and Chen [64] provide four non-dimensional equations of motion related to the box shaped pattern, the first two of which are obtained by a moment balance. As thoroughly derived in Ref. [6], dimensional equivalents of these two equations are given by

$$\mu B^3 \tan^3 \phi (4 - 3\gamma^*) \ddot{\theta}_1 = 2P(t)B^2 \tan^2 \phi (3 - 2\gamma^*) - 12M_0\lambda f_1 \quad (6.21)$$

and

$$\mu B^{*3} (4 - 3\gamma) \ddot{\theta}_2 = 2P(t)B^{*2} (3 - 2\gamma) - 12M_0\lambda f_2, \quad (6.22)$$

where  $\mu$  is the mass per unit plate area,  $\ddot{\theta}_{1,2}$  are the respective angular accelerations of regions I and II,  $\gamma = B/L$  and  $M_0 = \sigma_y h^2/4$ . Meanwhile, boundary parameter  $\lambda$  is defined as equaling 1 for simple supports and 2 for clamped supports. In addition, Yu and Chen [64] refer to  $f_{1,2}$  as modifying factors, which are themselves modified in Ref. [6]. These modifying factors are defined in Appendix C.

The various terms in Eqs. 6.21 and 6.22 arise from a moment balance, defined by

$$\sum M_y = I_y \ddot{\theta}, \quad (6.23)$$

where the left-hand side accounts for all moments acting about the  $y$ -axis (as located in Fig. 6.5), and  $I_y$  is the mass moment of inertia of a given rigid body about the same axis. As such, the left-hand sides of Eqs. 6.21 and 6.22 represent  $I_y \ddot{\theta}$  for either region I or II.<sup>5</sup> Furthermore, the first terms on the right-hand sides of these equations represent the moment caused by the external pressure (see Fig. 6.5a). The remaining term in each equation is the moment caused by the membrane forces and bending moments depicted, respectively, in Figs. 6.5b-c. Currently, the shear forces  $Q_{13}$  and  $Q_{23}$  shown in Fig. 6.5b are ignored due to the plate having a very small thickness.

Moreover, Yu and Chen's [64] third equation of motion arises from a force balance. By Newton's second law of motion, region III accelerates as a function of all forces acting on it. Moreover, by geometry, this region's motion must be transverse to the  $x$ - $y$  plane in Fig.

---

<sup>4</sup>As in Section 6.2.2,  $P(t)$  can also represent an equivalent uniform load.

<sup>5</sup>As shown in Ref. [6], the left-hand sides of these equations actually give the true mass moment multiplied by  $\cos^3 \theta_{1,2}$ .

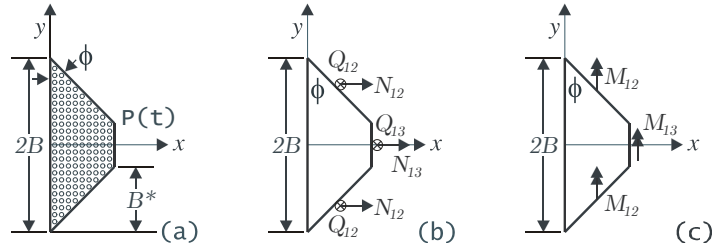


Figure 6.5: Moment-causing loads acting on region I of box shaped deformation pattern: (a) transverse pressure loading, (b) shear and membrane forces, (c) moments.

6.3. Therefore,  $\sum F_z = m\ddot{w}_{III}$ . Per Fig. 6.5b, the only forces that act in the  $z$ -direction on region III are the uniform pressure force and the restraining shear forces  $Q_{13}$  and  $Q_{23}$  along the region's edges. If the shear forces are again ignored, the force balance becomes

$$\mu\ddot{w}_{III} = P(t). \quad (6.24)$$

The acceleration in Eq. 6.24 can be found from continuity, as the displacements, velocities and accelerations of regions I and II must match those of region III where they adjoin. By defining velocity  $\dot{w}_{III}$  in terms of angular velocity, Eq. 6.24 can be rewritten as

$$\mu B \frac{d}{dt}(\dot{\theta}_1 \tan \phi) = P(t). \quad (6.25)$$

Equation 6.25, meanwhile, can be reexpressed in terms of loading impulse by simply integrating both sides of this equation with respect to time. The resulting alternate third equation of motion of Ref. [64] is then

$$\mu B \tan \phi \dot{\theta}_1 = \int_0^t P(t) dt \equiv I(t). \quad (6.26)$$

Finally, the fourth of Yu and Chen's [64] equations of motion is found via continuity. This continuity equation can be expressed as

$$B \tan \phi \dot{\theta}_1 = B^* \dot{\theta}_2. \quad (6.27)$$

If projection angle  $\phi = 45^\circ$ , as was previously assumed,  $B^* = B$ . In this case, per Eq. 6.27,  $\dot{\theta}_1 = \dot{\theta}_2$ , which can, in turn, be used to simplify Eqs. 6.21 and 6.22. As shown in Appendix C, all of these equations can be combined to obtain an initial value of  $B^*$ .

As stated in Ref. [6], there are some problems with the equations of motion developed by Yu and Chen [64]. First, Eq. 6.24 ignores shearing forces around the edges of region III. As such, there are no forces in the current model acting to restrain plate motion due to the external loading. By Eq. 6.24, region III has a positive acceleration until the loading ends, at which time its velocity remains constant. Equation 6.26 shows that this velocity remains positive with a positive impulse. This condition is not accurate as Biggs [5], amongst others, has shown that this maximum deflection for a decreasing pressure loading occurs before the loading is finished. Indeed, this is seen in all of the computational results of this dissertation. In these cases, a further increase in total impulse has no effect on maximum deflection, contrary to Yu and Chen's model [64]. Physically, there needs to be some sort of restraining force else deflections will increase indefinitely. This force can be taken as the net reaction due to the membrane stretching forces in regions I and II. These membrane forces do not appear in the moment balance equations as they act parallel to the given regions, so that their lines of action run through the axis of rotation.

#### 6.2.4 Smoothing Transition at Yielding

The structural model introduced in Chapter 3 consists of a sinusoidal and roof shaped deformation pattern, respectively, for the elastic and plastic phases. The transition between these two shapes is made compatible at yielding by setting the final, central deflection and velocity of the elastic phase equal to the corresponding initial values of the plastic phase. Mathematically, this method seems logical. Physically, however, a plate cannot instantaneously change from one such deflection mode to another which is completely dissimilar.

This fact is made clear in Figs. 6.6 and 6.7, which show the transient deformation profiles due to a uniform load for various cases per a finite element analysis. In all of these cases, there is a gradual change in overall shape from zero to peak central deflection. Although the model presented in Chapter 3 accurately predicts maximum deflection, the assumed elastic mode shape of Eq. 3.12 exaggerates the difference in this peak over the rest of the plate at early times. Meanwhile, the assumed plastic profile with a central hinge line does appear in at least one time instant for all cases in Figs. 6.6 and 6.7, but not instantaneously. Moreover, the current assumed shape predicts that this horizontal line stretches only 25 mm

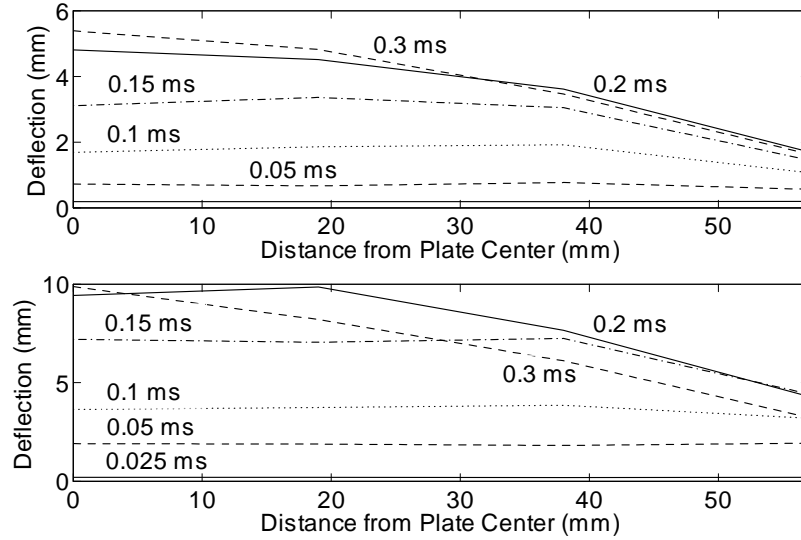


Figure 6.6: Transient deformation profiles of a clamped, high strength aluminum  $150 \times 100$  mm plate due to a uniform load for  $Z = 1$  when (a)  $h = 2.5$  mm, and (b)  $h = 1$  mm.

from the plate center throughout plastic deformation, which is contrary, for example, to the 0.15 ms case in Fig. 6.7b. Furthermore, notice that the central deflection is not necessarily the highest deflection at a given time instant. This is shown in the 0.2 ms case in Fig.6.6b and the 0.05 ms case in Fig.6.7b. These particular trials exhibit the greatest deformations with a lower thickness and more intensive pressure loading being used, respectively. The study of global transient deformation shapes has been limited in the literature, with one example being the work of Zhu [105].

Therefore, major problems with the current method's elastic-plastic treatment are the failure to capture a transient deflection shape and the abrupt change from a curved deflection shape to one with rigid sections and a potential central hinge line. In order to relieve this sharp transition, it is proposed that, for a nonuniform load, the elastic shape be used only over a central region. This approach is consistent with the phenomenon of dishing, where for close-in explosions outer parts of the plate do not deflect immediately (e.g., see Ref. [79]). This localized effect becomes more important as plate area increases and standoff distance decreases. As a result, the initial boundary of interest changes from the plate edges to the hinge lines defining the central deflection region (see Fig. 6.3). The location of these hinge

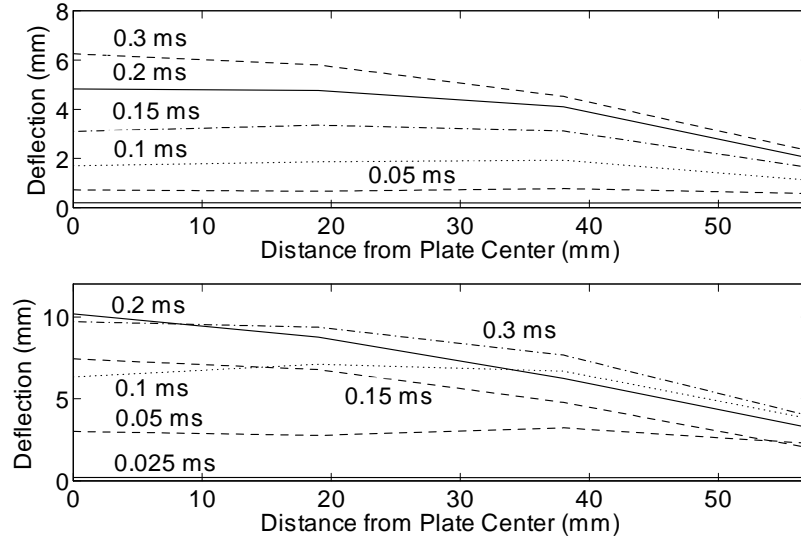


Figure 6.7: Transient deformation profiles of a clamped aluminum  $150 \times 100 \times 2.5$  mm plate due to a uniform load for (a)  $\sigma_0 = 345$  MPa,  $Z = 1$ , and (b)  $\sigma_0 = 970$  MPa,  $Z = 0.6$ .

lines can be determined as per Eqs. C.7 and C.8 for a rigid plastic box shape. Thus, the proposed method is truly elastic-plastic in the sense that the elastic phase contains elements of the plastic phase.

There will then be zero deflection at the edges of the central deflection region. As these edges are not clamped, the assumed simply supported deflection shape of Eq. 3.4 can be used. This effectively treats the central region as a smaller, simply supported plate. This treatment is analogous to that of Zhenqiu [106], who studied the various deformation shapes of stiffened plates subjected to a uniform blast.

Once yielding occurs for this smaller interior plate, the box shaped pattern is fully incorporated. The deflection and velocity at the hinge lines are again made compatible. But since these lines have been present since the start of deformation, there is no longer any abrupt phase transition like in Chapter 3. This method then succeeds in smoothing the transition between the elastic and plastic phases. Moreover, it also captures the general nature of the experimentally obtained shape in Fig. 6.2.

### 6.2.5 Permanent Deformation via Damping

The current structural model predicts permanent deformation via Eq. 3.31, an approximation that subtracts a percentage of the elastic deflection from the maximum total plate deflection. Although this method produces permanent deflections comparable to those of experiment (see Section 3.5), mathematically, it is rather crude. This is seen in Section 3.4.3, where a calibration is sometimes required to better match the current model's predictions with finite element results. Ideally, the equations of motion themselves should give an approximate deflection-time history, with a steady state permanent deflection achieved after some finite time. However, all necessary damping terms drop out of the elastic and plastic phase equations of Sections 3.1 and 3.2.

The damping mechanism for a particular problem can be determined in various ways. Limited experiments can be performed, but this more or less relies on a calibration. Moreover, requiring expensive experiments for initial design defeats the primary purpose of using a simplified structural model. Morison [107] suggests another way, namely attaining proper damping terms by equating virtual work during deformation. This method, however, requires the reestablishment of all the governing equations provided in this dissertation. Regardless of method, adding the ability to retain damping terms, and therefore, to predict permanent plate deformation in a less empirical manner, is an area of future improvement to the current model.

## 6.3 Extension of Current Model to Shells

This dissertation has, up until this point, dealt entirely with the blast loading of thin, flat plates. As previously stated, thin plates can represent various aircraft structures, such as a small section of the fuselage. In modeling a larger section, however, the prevailing curvature of the fuselage makes the use of thin, curved plates or shells more appropriate.

As such, this section establishes a methodology for analyzing the response of thin, cylindrical shells,<sup>6</sup> where both elastic and plastic deformations are significant. This section mirrors Sections 3.1 and 3.2, regarding the similar response of thin plates. Indeed, the

---

<sup>6</sup>For general background and further details on the theory of thin, elastic shells, see Refs. [57, 108, 109].

elastic treatment of Singh and Singh [65] for a hinged shell is presented here and appropriately modified. The corresponding yield condition, which is not explicitly given in Ref. [65], is also derived. Finally, methods that can account for plastic deflections are briefly discussed.

### 6.3.1 Elastic Phase Shell Model

As given by Amabili and Padoussis [110] in their review of shell dynamics, the two governing equations for dynamic response of an elastic shell using the  $w$ - $F$  formulation are

$$\nabla^4 F = Eh \left\{ -\frac{1}{R} \frac{\partial^2 w}{\partial x^2} + \left( \frac{\partial^2 w}{\partial x \partial y} \right)^2 - \frac{\partial^2 w}{\partial x^2} \frac{\partial^2 w}{\partial y^2} \right\} \quad (6.28)$$

and

$$\frac{Eh^3}{12(1-\nu^2)} \nabla^4 w + \rho h \ddot{w} = p(x, y, t) + \frac{1}{R} \frac{\partial^2 F}{\partial x^2} + \frac{\partial^2 F}{\partial y^2} \frac{\partial^2 w}{\partial x^2} + \frac{\partial^2 F}{\partial x^2} \frac{\partial^2 w}{\partial y^2} - 2 \frac{\partial^2 F}{\partial x \partial y} \frac{\partial^2 w}{\partial x \partial y}. \quad (6.29)$$

As in Eqs. 3.1 and 3.2,  $E$  is the elastic modulus,  $\nu$  Poisson's ratio,  $\rho$  the mass density,  $p$  the acting pressure, and the operator  $\nabla^4 \equiv \frac{\partial^4}{\partial x^4} + 2 \frac{\partial^4}{\partial x^2 \partial y^2} + \frac{\partial^4}{\partial y^4}$ . Meanwhile, from Fig. 6.8,  $h$  and  $R$  are the respective shell thickness and radius. The relationships between the Airy stress function  $F$  and in-plane membrane stresses given in Eqs. 3.3a-c still apply.

Assuming a sinusoidal, elastic deflection shape, the transverse deflection of the shell in Fig. 6.8 may be expressed as

$$w = A(t) \sin \frac{m\pi x}{L} \sin \frac{ny}{R} + B(t) \sin^2 \left( \frac{m\pi x}{L} \right). \quad (6.30)$$

Clearly, each term in Eq. 6.30 satisfies the simply supported boundary conditions at  $x = 0$  and  $x = L$ . The former term in this equation is analogous to Eq. 3.4 for a simply supported plate. Meanwhile, the latter term is added to better match experimental deflection results [111]. Summations in both  $m$  and  $n$  are implied.

Using a procedure similar to those stated in Sections 3.1 and 6.1, Singh and Singh [65] found the following expression for the Airy stress function:

$$F(x, y, t) = Eh \times \left[ \frac{A(t)^2}{32} \left( \frac{\alpha_m}{\beta_n} \right)^2 \cos 2\beta_n y + \frac{\alpha_m^2 \beta_n^2 n^2 A(t)^3}{4R (9\alpha_m^2 + \beta_n^2)^2} \sin 3\alpha_m x \sin \beta_n y + \frac{\alpha_m^2 A(t) (4 - \beta_n^2 n^2 A(t)^2)}{4R (\alpha_m^2 + \beta_n^2)^2} \sin \alpha_m x \sin \beta_n y \right], \quad (6.31)$$

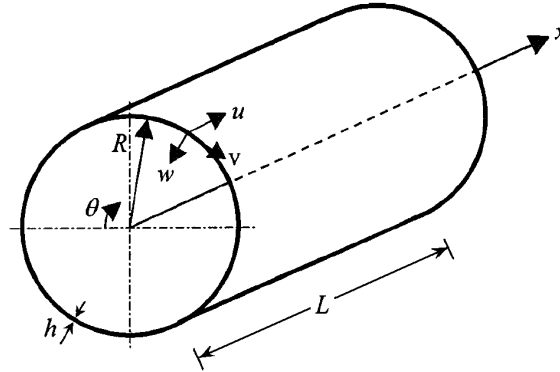


Figure 6.8: Shell geometry and coordinate system [110].

where  $\alpha_m = m\pi/L$  and  $\beta_n = n/R$ . However, Singh and Singh [65] fail to note an important step in their derivation, which is the only change in the aforementioned procedure. Instead of setting  $u = v = 0$  at the boundaries, a periodic condition must hold in that

$$v(x, y) = v(x, y + 2\pi R) \quad (6.32)$$

as  $y$  acts tangentially to the cross-section. Alternatively, Eq. 6.32 may be written as

$$\int_0^{2\pi R} \frac{\partial v}{\partial y} dy = 0, \quad (6.33)$$

where this integral is defined as in Eq. 3.7b, with an additional  $w/R$  term, which accounts for the non-zero curvature, subtracted within the braces. It turns out that Eq. 6.33 holds only if

$$B(t) = A(t)^2 n^2 / 4R,$$

where  $B(t)$  is the central deflection associated with the second mode shape in Eq. 6.30. As a result, there are no  $B(t)$  terms in Eq. 6.31, as they have been replaced by higher order  $A(t)$  terms. It can further be noted that Eq. 6.32 is misprinted in Ref. [111] with  $v(x)$  substituted for  $v(x, y)$ .

Now substituting Eqs. 6.30 and 6.31 into Eq. 6.29 and carrying out a Galerkin integration of the resulting residue, the large deflection equation of motion for a hinged, elastic

shell is determined as

$$\begin{aligned} \rho h \ddot{A}(t) + Eh \left[ \frac{h^2(\alpha_m^4 + \beta_n^4)}{12(1-\nu^2)} + \frac{\alpha_m^4}{R^2(\alpha_m^2 + \beta_n^2)^2} \right] A(t) + \frac{Eh\alpha_m^4}{16} \left[ 1 - \frac{8\beta_n^2 n^2}{R^2(\alpha_m^2 + \beta_n^2)^2} \right] A^3(t) \\ \frac{Eh\alpha_m^4 \beta_n^4 n^4}{16R^2} \left[ \frac{1}{(9\alpha_m^2 + \beta_n^2)^2} + \frac{1}{(\alpha_m^2 + \beta_n^2)^2} \right] A^5(t) = q_0(t), \end{aligned} \quad (6.34)$$

where it is assumed that pressure is of the form  $p(x, y, t) = q_0(t) \sin \alpha_m x \sin \beta_n y$ . Without this assumption, which is reminiscent of Eq. 4.3, one can substitute the expression  $2\pi/RL \times \int_0^{2\pi R} \int_0^L p(x, y, t) \sin \alpha_m x \sin \beta_n y dx dy$  in place of  $q_0(t)$  in Eq. 6.34.

Whereas the elastic equation of motion for a plate is a cubic function of displacement, a more complicated, fifth-order expression applies for a shell. Clearly, a linear stiffness does not effectively model either geometry. It should be noted that Singh and Singh [65] incorrectly provide Eq. 6.34 with the expression  $(\alpha_m^2 + \beta_n^2)$  in place of  $(\alpha_m^4 + \beta_n^4)$  in the coefficient for  $A(t)$ . Furthermore, the cosine terms in Eq. 3.10 for the Galerkin integral are replaced here by the proper shell mode  $\sin \alpha_m x \sin \beta_n y$ , while the bounds of integration are changed accordingly to  $x = \{0, L\}$  and  $y = \{0, 2\pi R\}$ . A similar equation of motion can be derived for a clamped shell given an appropriate choice of the transverse deflection shape.

### 6.3.2 Yield Condition of Hinged Shell

As is the case with plates, Eq. 6.34 is only valid up until a yield condition is satisfied. For shells, it is assumed that the von Mises yield condition of Eq. 3.15 again applies. Recall that this criterion is defined as

$$Y_c \equiv \frac{M_x^2 + M_y^2 - M_x M_y + 3M_{xy}^2}{M_0^2} + \frac{N_x^2 + N_y^2 + N_x N_y + 3N_{xy}^2}{N_0^2} - 1 = 0, \quad (6.35)$$

where  $M_k$  and  $N_k$  represent the elastic bending moments per unit length and membrane forces per unit length, respectively, in either the  $x$ ,  $y$  or  $xy$  direction. Meanwhile,  $M_0$  is the plastic bending moment per unit length, and  $N_0$  the plastic membrane force per unit length. These quantities are mathematically defined as in Eqs. 3.5a-b, 3.16a-b and 3.16f. Due to how the deflection and Airy stress function are defined in this section, the membrane forces per unit length  $N_x$ ,  $N_y$  and  $N_{xy}$ , meanwhile, are given respectively by Eqs. 3.16c-e with the thickness  $h$  removed. It can easily be seen that this change preserves proper units

in the subsequent derivations. For convenience, the Von Mises yield condition, which is satisfied when  $Y_c$  first takes on a non-negative value, is rewritten as

$$Y_c \equiv Y_m + Y_n - 1 = 0.$$

After appropriate substitution of the assumed first-order (i.e.,  $m = n = 1$ ) deflection and Airy stress functions of Eqs. 6.30 and 6.31, the first term of Eq. 6.35 becomes

$$\begin{aligned} Y_m(x, y, t) = & \frac{16E^2h^2}{\sigma_0^2(1-\nu^2)^2} \left\{ [(\alpha^4 + \beta^4)(\nu^2 + \nu + 1) + \alpha^2\beta^2(\nu^2 + 4\nu + 1)] A^2(t) \right. \\ & - \frac{\alpha^2}{R} [\alpha^2(\nu^2 + \nu + 1) + \beta^2(2\nu + 1)] A^3(t) \\ & \left. + \frac{\alpha^4}{R^2}(\nu^2 + \nu + 1)A^4(t) \right\}. \end{aligned} \quad (6.36)$$

Equation 6.36 comes about by evaluating the derived expressions at the maximum shell deflection. From Eq. 6.30, this deflection occurs when  $x = L/2$  and  $y = \pi R/2$ . Similarly, substituting Eq. 6.31 into Eqs. 3.16c-f (including  $h$  only in the expression for  $N_0$ ), the second term of Eq. 6.35 becomes

$$Y_n(x, y, t) = \frac{E^2\alpha^4}{\sigma_0^2} [C_2A^2(t) + C_3A^3(t) + C_4A^4(t) + C_5A^5(t) + C_6A^6(t)], \quad (6.37)$$

where the various  $C_n$  represent functions of  $\alpha$ ,  $\beta$  and  $R$ . For example,

$$C_2 = \frac{\alpha^4 - \alpha^2\beta^2 + \beta^4}{R^2(\alpha^2 + \beta^2)^4} \text{ and } C_3 = \frac{2\beta^2 - \alpha^2}{8R(\alpha^2 + \beta^2)^2}.$$

Therefore, by Eqs. 6.35, 6.36 and 6.37, the yield condition of a hinged shell has the general form

$$Y_c = \frac{E^2\alpha^4}{\sigma_0^2} [D_2A^2(t) + D_3A^3(t) + D_4A^4(t) + C_5A^5(t) + C_6A^6(t)] - 1 = 0, \quad (6.38)$$

where the various  $C_n$  have the same values as in Eq. 6.37. Meanwhile, the various  $D_n$  combine the corresponding coefficients of the bending and membrane terms in Eqs. 6.36 and 6.37. As such, the  $D_n$  are functions of not only  $\alpha$ ,  $\beta$  and  $R$ , but also of  $\nu$  and  $h$ . Comparing Eq. 6.38 with its simply supported plate analog Eq. 3.19, it is clear that the yield condition of the shell is much more complicated as Eq. 3.19 contains only second and fourth-order polynomials of maximum deflection.

As Singh and Singh [65] do not provide the yield condition for a hinged shell, Eq. 6.38 and its various coefficients are newly derived in this dissertation. A similar procedure can be used in deriving the yield condition of a clamped shell once the assumed deflection shape and Airy stress function are determined.

### 6.3.3 Plastic Phase Shell Model

Analogous to the plate model of Chapter 3, the elastic equation of motion for a hinged shell (i.e., Eq. 6.34) is used up until the yield condition of Eq. 6.38 is first satisfied. Afterwards, a plastic shell model must be incorporated to continue tracking the maximum shell deformation. Jones [63] offers a few potential options. One method is similar to his roof shaped model for a rigid plastic plate. Here, the velocity field acts linearly throughout the length of the shell, peaking midway between consecutive reinforcement rings. In the current application, these rings can model the frames which run along a fuselage's circumference. Furthermore, Jones [63] presents another method that applies to short cylindrical shells and consists of a transient velocity field. The shape of this velocity field is similar to that of the box shaped deflection pattern described in Section 6.2.

Another plastic shell model is that of Hoo Fatt and Wierzbicki [96,97], which converts the typical two-dimensional, shell boundary value problem into an equivalent SDOF problem. Their method, which extends the elastic treatment of Calladine [112], essentially models the shell response like a plastic string on a nonlinear plastic foundation. Equivalent values of pressure, ring resistance and tensile force are determined based on various assumptions. These equivalent parameters allow the simplified equation of motion for a plastic shell to be solved. Many example applications are presented in Refs. [96,97], including mass impact and the impulsive loading of both stiffened and unstiffened shells. Meanwhile, assumed pressure functions include an exponential decay and a Gaussian distribution. Such applications are clearly in-line with the current study on explosive pressure loadings.

## Chapter 7

### Conclusions and Future Work

#### 7.1 Conclusions

The dissertation validates the elastic-plastic model of the current author [6], which is a simple and efficient estimator of maximum plate deflection when both elastic and plastic effects are significant and loading is uniformly distributed. The results from the current model match reasonably well with those from the finite element package ANSYS [76] for clamped edges, where the average error is 10.7% over all trials. For simple supports, this error increases to 13.5%. However, with these design-level accurate results comes an exponential reduction in processing time.

In particular, for smaller area plates, reasonable estimates are obtained when deformation is dominated by either elastic or plastic effects. Furthermore, plates with a high aspect ratio tend to result in even closer approximations when neither elastic nor plastic effects dominate response. Unlike for the simply supported trials, where a high yield strength is crucial, clamped trials show a much improved accuracy when plate thickness is increased. These trends are displayed in Fig. 3.8.

In addition, Eq. 3.31 allows one to predict the permanent deflection of a plate subjected to a uniform blast pressure. Such predictions compare favorably with experimental results of both aluminum and steel square plates. However, the current method appears to be inappropriate for oblong steel plates subject to a highly intensive load as the plastic part of the current model becomes inaccurate. Still, there is potentially a wide range of applicable problems for this preliminary design method.

Moreover, Chapters 4 and 5 of this dissertation examine two specific needs in the design

of blast resistant structures. First, a simplified analytical model is used to predict the maximum deflection of both small and large representative panels subjected to a nonuniform pressure. Furthermore, a normalized impulse criterion is suggested (see Eq. 4.8) to assess when the model can be further simplified by assuming a uniform loading. It is proposed, based on the comparison of finite element deflection results, that a uniform loading is justified when  $i^* > 0.9$ . Secondly, uncertainty in compiled blast parameter data is addressed. The Monte Carlo method, as applied to the present problem, gives the designer a means to estimate both the level of uncertainty and the probability of structural failure under the given assumptions. More parameter uncertainty can be added as required to account for unknowns relating to, for example, plate boundary condition, peak pressure measurement (taken as deterministic here) and the overall nonuniform blast model.

Furthermore, Chapter 6 suggests some improvements to the current structural model. These suggestions include modifying the assumed elastic deformation shape by using a higher-order Fourier series expansion or changing the associated exponent of Eq. 3.12. Moreover, the plastic equations of motion are changed to correspond to a box shaped deformation pattern. The derivation of the resulting governing equations via energy rate balance is unique to the current author. Procedures to smooth the transition between the elastic and plastic phases, as well as to include material damping are outlined. In addition, the supplied plate equations are extended for use with cylindrical shells. This results in newly derived expressions for the shell's yield condition, which has the general form of Eq. 6.38.

## 7.2 Future Work

A large area of future work is to implement the changes outlined in Chapter 6 for various components of the current loading and structural models. These changes include modifying the elastic model to better match the transient shapes of finite element and experimental results, and validating the newly derived equations pertaining both to the box shaped deformation pattern and thin, cylindrical shells subject to blast loading. Introducing damping into the relevant governing equations can also help to more clearly predict

permanent structural deformations. Furthermore, a future structural model could incorporate more complexities, such as material strain rate sensitivity and the presence of stiffeners or other nonideal boundaries.

Moreover, the loading model should also be adjusted to include a larger variety of uncertainties. In this dissertation, duration time is used as the primary random variable. As shown throughout this work, however, pressures and impulses also greatly fluctuate within published results. Finally, the specialized topics briefed in Chapter 4 can also be examined more thoroughly. A future model should evaluate the loaded structure's response sensitivity to such issues as negative phasing and pressure relief. Ideally, all of these issues can be incorporated without a heavy trade-off in processing time.

## Appendix A

### Sample Matlab Program

This Matlab<sup>®</sup> program calculates the maximum deflection for a clamped plate per the combined elastic-plastic model of Chapter 3, making use of an effective uniform pressure. Options include selection of geometry and blast parameter data set. An option to implement a Monte Carlo scheme to calculate mean deflection, standard deviation and probability of failure per the data of both Kinney and Graham [3] and ConWep [4] also exists.

```
%Import ConWep and Kinney and Graham data from text files.
data=dlmread('Zdata.txt'); data2=dlmread('Zdata2.txt');
dataKG=dlmread('ZdataKG.txt'); dlength=length(data);
for i=1:dlength;
    Z(i,1)=data(i,1); Ps(i,1)=data(i,2); Pr(i,1)=data(i,3); ta(i,1)=data(i,4);
    Ts(i,1)=data(i,5); is(i,1)=data(i,6); ir(i,1)=data(i,7);
    bsi(i,1)=data2(i,2); br(i,1)=data2(i,3);
    PsKG(i,1)=dataKG(i,2); taKG(i,1)=dataKG(i,3); TsKG(i,1)=dataKG(i,4);
    isKG(i,1)=dataKG(i,7); alphaKG(i,1)=dataKG(i,8);
end
%Material Properties for Aluminum Test Plates
mat=input('Enter material number (1 for small plate, 2 for large plate):');
source=input('Enter source number (1 for ConWep, 2 for Kinney & Graham,...
    3 for random):');
RP=input('Rigid plastic analysis? (1 for yes, 0 for no):');
Box=input('Box shape considered? (1 for yes, 0 for no):');
Wc=6; R0=0.3:0.025:1;
```

```

Wclength=length(Wc); R0length=length(R0);
ncase=Wclength*R0length; Wcase=zeros(1,ncase); Rcase=zeros(1,ncase);
tol=0.1; %Default for nonrandom analysis.
stdev=zeros(ncase,1); numit=zeros(ncase,1);
tol=input('Enter tolerance for Monte Carlo simulation in mm:');
tol=tol/1000; %tol converted from millimeters to meters.
vari=zeros(ncase,1); nfail=zeros(ncase,1); nfail2=zeros(ncase,1);
if mat==1;
    rho=2780; mu=0.33; Em=73.1e9; Sy=345e6;
    a_list=0.508; b_list=0.2032; h_list=0.0016;
    dim1=a_list/2; %Quarter plate dimensions in m.
    dim2=b_list/2; area4=dim1*dim2; ndivx=20; ndivy=8; fcrit=0.05838;
elseif mat==2;
    rho=2780; mu=0.33; Em=72e9; Sy=380e6;
    a_list=1.48; b_list=1.48; h_list=0.004;
    dim1=a_list/2; dim2=b_list/2;
    area4=dim1*dim2; ndivx=20; ndivy=20; fcrit=0.3347;
end
%Define Plate Grid
phi=45*pi/180; %Hinge angle for symmetric loading.
nel=ndivx*ndivy; ncase=0;
for i=1:Wclength;
    for j=1:R0length;
        ncase=ncase+1;
        Wcase(1,ncase)=Wc(1,i); Rcase(1,ncase)=R0(1,j);
    end
end
Zcase=Rcase./Wcase.^(1/3);
delx=dim1/ndivx; dely=dim2/ndivy;

```

```

[x,y]=meshgrid(0:delx:dim1,0:dely:dim2); %Establish nodal locations.
k=0;
for i=1:ndivy+1;
    for j=1:ndivx+1;
        k=k+1;
        xy(k,1)=x(i,j); xy(k,2)=y(i,j);
        r1(1,k)=sqrt(x(i,j)^2+y(i,j)^2);
    end
end
npoints=k;
%Timestepping, Matrix Declarations & Loading Function
tstep=input('Enter timestep in microsec:');
tstep=tstep/1e6; %tstep converted from microsecs to seconds.
tend=input('Enter end time in millisec:'); tend=tend/1e3;
tel=zeros(ncase,1); wel=zeros(ncase,1); Vel=zeros(ncase,1);
tm=zeros(ncase,1); wm=zeros(ncase,1); EP=zeros(ncase,1);
t=0:tstep:tend+tstep; %Time in seconds with range per input.
tcount=length(t);
W1=zeros(ncase,tcount);
%Main Program
global p1 t1 I1; %Make variables global for function af.m.
for i=1:ncase; % i indicates dimensional case.
    a=a_list; b=b_list; rab=a/b; h=h_list; hcrit=h;
    pc=12*Sy*h^2/b^2;
    polycount=0; %polycount=0 indicates hinge lines have not yet formed.
    %Initialize Coefficients for Runge-Kutta & Yield Condition Equations
    D=0; D2=0; D3=0; D4=0;
    C1=0; C2=0; C3=0; C4=0; C5=0; C6=0;
    Ln=0; Ln1=0; Ln2=0; Lns=0; Lm=0;

```

```

Zxy=zeros(1,npoints); theta=zeros(1,npoints); Prr=zeros(1,npoints);
tar=zeros(1,npoints); Tsr=zeros(1,npoints); irr=zeros(1,npoints);
Psr=zeros(1,npoints); brr=zeros(1,npoints); bsr=zeros(1,npoints);
Zxy=sqrt(Rcase(1,i)^2+r1.^2)/Wcase(1,i)^(1/3); theta=atan(r1/Rcase(1,i));
%Determine applicable loading parameters.
Prr=interp1(Z,Pr,Zxy)*1e5; Psr=interp1(Z,Ps,Zxy)*1e5;
tarC=interp1(Z,ta,Zxy)*Wcase(1,i)^(1/3)/1e3;
TsrC=interp1(Z,Ts,Zxy)*Wcase(1,i)^(1/3)/1e3;
irr=interp1(Z,ir,Zxy)*Wcase(1,i)^(1/3)*1e2;
isr=interp1(Z,is,Zxy)*Wcase(1,i)^(1/3)*1e2;
tarK=interp1(Z,taKG,Zxy)*Wcase(1,i)^(1/3)/1e3;
TsrK=interp1(Z,TsKG,Zxy)*Wcase(1,i)^(1/3)/1e3;
isrK=interp1(Z,isKG,Zxy)*Wcase(1,i)^(1/3)*1e2;
%Begin while loop for Monte Carlo method.
error=1; iter=0; tmit=0; wmit=0; wmlast=0;
while error>tol;
    wcurr=0; wlast=0; wmax=0; ycurr=0; ylast=0; tmax=0;
    K1=0; K1p=0; K2=0; K2p=0; K3=0; K3p=0; K4=0; K4p=0; Yc=0; elcase=0;
    iter=iter+1;
    tarand=rand; Tsrand=rand; irand=rand; tamc=tarC*tarand+tarK*(1-tarand);
    Tsrmc=TsrC*Tsrand+TsrK*(1-Tsrand); tar=tamc; Tsr=Tsrmc;
    irmc=irr.*(irand+isrK./isr*(1-irand));
    %Determine pressure-time histories across the plate.
    %Scale starting and ending times.
    tarmin=min(tar); tstart=tar-tarmin; tend=tstart+Tsr; tendmax=max(tend);
    tstartmax=max(tstart); Psxt=zeros(tcount,npoints); Prxt=zeros(tcount,npoints);
    Ptau=zeros(tcount,npoints); p=zeros(tcount,1); brr=zeros(1,npoints);
    for j=1:npoints;
        p1=Prr(1,j); t1=Tsr(1,j); I1=irmc(1,j); brr(1,j)=fzero(@af,1);

```

```

end
for k=1:tcount;
    for j=1:npoints;
        if t(1,k)>=tstart(1,j) & t(1,k)<=tend(1,j);
            tsh=t(1,k)-tstart(1,j); ang=theta(1,j);
            Ptau(k,j)=Prr(1,j)*(1-tsh/Tsr(1,j))*exp(-brr(1,j)*tsh/Tsr(1,j))*cos(ang)^2;
        end
    end
end
nodem=1;
%Generate equivalent uniform pressure per assumed elastic deformation shape.
for m=1:nel;
    if rem(nodem,ndivx+1)==0; nodem=nodem+1; end
    x1=xy(nodem,1); x2=xy(nodem+1,1);
    y1=xy(nodem,2); y2=xy(nodem+ndivx+1,2);
    pelavg=(Ptau(k,nodem)+Ptau(k,nodem+1)+Ptau(k,nodem+ndivx+1)...
        +Ptau(k,nodem+ndivx+2))/4;
    pix=pi*x2/a+1/2*sin(2*pi*x2/a)-pi*x1/a-1/2*sin(2*pi*x1/a);
    piy=pi*y2/a+1/2*sin(2*pi*y2/a)-pi*y1/a-1/2*sin(2*pi*y1/a);
    p(k,1)=p(k,1)+4/pi^2*pelavg*pix*piy;
    nodem=nodem+1;
end
end
punif(:,i)=Prxt(:,1)/1e5; puneq(:,i)=p(:,1)/1e5;
impUF=cumsum(punif)*tstep*1e3; impEU=cumsum(puneq)*tstep*1e3;
%Elastic Coefficients and Yield Condition
D=(Em/Sy/(1-mu^2))^2*(h*pi/a/b)^4;
D2=4*Em*h^2*pi^4/27/rho/a^4/(1-mu^2)*(3+2*rab^2+3*rab^4);
D3=Em*pi^4/rho/a^4*((1+2*mu*rab^2+rab^4)/8/(1-mu^2)+17/144...
    +rab^4/9*(17/16+2/(1+rab^2)^2+0.5/(1+4*rab^2)^2+0.5/(4+rab^2)^2));

```

```

D4=16/9/rho/h;
Ln1=3/(1-mu^2)*(1/a^2+mu/b^2)+5/a^2+a^2*(8/(a^2+b^2)^2...
+16/(4*a^2+b^2)^2+4/(a^2+4*b^2)^2);
Ln2=3/(1-mu^2)*(mu/a^2+1/b^2)+5/b^2+b^2*(8/(a^2+b^2)^2...
+4/(4*a^2+b^2)^2+16/(a^2+4*b^2)^2);
Lns=Ln1^2+Ln2^2+Ln1*Ln2;
Lm=(a^4+b^4)*(mu^2-mu+1)-(a*b)^2*(mu^2-4*mu+1);
for k=1:tcount-1;
    Yc=D*(Lns*wcurr^4/h^4*(a*b)^4*(1-mu^2)^2/1024+4*Lm*wcurr^2/h^2/9)-1;
    if Yc<=0 & RP==0; %Elastic Shape Applicable
        K1=tstep*ycurr;
        K1p=tstep*(D4*p(k,1)-D2*wcurr-D3*wcurr^3);
        K2=tstep*(ycurr+K1p/2);
        K2p=tstep*(D4*p(k,1)-D2*(wcurr+K1/2)-D3*(wcurr+K1/2)^3);
        K3=tstep*(ycurr+K2p/2);
        K3p=tstep*(D4*p(k,1)-D2*(wcurr+K2/2)-D3*(wcurr+K2/2)^3);
        K4=tstep*(ycurr+K3p);
        K4p=tstep*(D4*p(k,1)-D2*(wcurr+K3)-D3*(wcurr+K3)^3);
    else %Plastic Analysis Required
        if elcase==0;
            tel(i,1)=t(1,k); wel(i,1)=wcurr; Vel(i,1)=ycurr; elcase=1;
        end
        C1=rho*b^2/6/Sy/h*(2*rab-tan(phi));
        C2=4/3/h^2*(3*rab-2*tan(phi)+1/tan(phi));
        C3=b^2/6/Sy/h^2*(3*rab-tan(phi));
        C4=rab+1/tan(phi);
        C5=4/h*(2*rab-tan(phi)+1/tan(phi));
        C6=h/3*(tan(phi)+1/tan(phi));
        if abs(wcurr)<hcrit;

```

```

K1=tstep*ycurr;
K1p=tstep/C1*(C3*p(k,1)-C2/2*wcurr^2-2*C4);
K2=tstep*(ycurr+K1p/2);
K2p=tstep/C1*(C3*p(k,1)-C2/2*(wcurr+K1/2)^2-2*C4);
K3=tstep*(ycurr+K2p/2);
K3p=tstep/C1*(C3*p(k,1)-C2/2*(wcurr+K2/2)^2-2*C4);
K4=tstep*(ycurr+K3p);
K4p=tstep/C1*(C3*p(k,1)-C2/2*(wcurr+K3)^2-2*C4);
else
K1=tstep*ycurr;
K1p=tstep/C1*(C3*p(k,1)-C5/2*wcurr-2*C6/wcurr);
K2=tstep*(ycurr+K1p/2);
K2p=tstep/C1*(C3*p(k,1)-C5/2*(wcurr+K1/2)-2*C6/(wcurr+K1/2));
K3=tstep*(ycurr+K2p/2);
K3p=tstep/C1*(C3*p(k,1)-C5/2*(wcurr+K2/2)-2*C6/(wcurr+K2/2));
K4=tstep*(ycurr+K3p);
K4p=tstep/C1*(C3*p(k,1)-C5/2*(wcurr+K3)-2*C6/(wcurr+K3));
end
end
wlast=wcurr; ylast=ycurr; wcurr=wlast+(K1+2*(K2+K3)+K4)/6;
if wcurr>wmax;
wmax=wcurr; tmax=t(1,k);
end
ycurr=ylast+(K1p+2*(K2p+K3p)+K4p)/6;
W1(i,k)=wcurr; V1(1,k)=ycurr; %Corrected 4/3/06.
end
tmit(iter,1)=tmax; wmit(iter,1)=wmax;
tm(i,1)=sum(tmit)/iter; wm(i,1)=sum(wmit)/iter;
error=abs(wm(i,1)-wmlast); wmlast=wm(i,1);

```

```

    %Ensure that at least ten iterations are run per Monte Carlo trial.
    if iter<=10; error=tol+1; end
end %of while loop for tolerance.
numit(i,1)=iter
for n=1:iter;
    vari(i,1)=vari(i,1)+(wmit(n,1)-wm(i,1))^2;
    if wmit(n,1)>fcrit;
        nfail(i,1)=nfail(i,1)+1;
    elseif wmit(n,1)>fcrit/1.2;
        nfail2(i,1)=nfail2(i,1)+1;
    end
end
end
stdev(i,1)=sqrt(vari(i,1)/(iter-1));
end %of i loop for cases.
t=t'*1000; W1=W1*1000; tel=tel*1000; wel=wel*1000; tm=tm*1000;
wm=wm*1000; %Convert seconds to msecs, meters to mm.
stdev=stdev*1000; nfail2=nfail+nfail2;
%Output Table
OPTable=zeros(ncase,11);
OPTable(:,1)=Wcase(1,:); OPTable(:,2)=Rcase(1,:); OPTable(:,3)=Zcase(1,:);
OPTable(:,4)=wel(:,1); OPTable(:,5)=tel(:,1); OPTable(:,6)=wm(:,1);
OPTable(:,7)=stdev(:,1); OPTable(:,8)=tm(:,1); OPTable(:,9)=numit(:,1);
OPTable(:,10)=nfail(:,1); OPTable(:,11)=nfail2(:,1); OPTable
pf=nfail./numit; pf2=nfail2./numit;

```

## Appendix B

### Sample ANSYS Program

This ANSYS<sup>®</sup> program calculates the maximum deflection for a clamped, aluminum plate per finite element analysis. A nonuniform loading function is assumed. Trials are run for various combinations of charge size and standoff distance.

```

/BATCH,LIST
*DEL,ALL          ! Clear all parameters.
! Define Parameter Arrays in Metric Units
*DIM,length,ARRAY,2
length(1)=0.508,1.48
*DIM,width,ARRAY,2
width(1)=0.2032,1.48
*DIM,height,ARRAY,2
height(1)=0.0016,0.004
*DIM,ystress,ARRAY,2
ystress(1)=345e6,380e6
*DIM,youngsm,ARRAY,2
youngsm(1)=73.1e9,72e9
*DIM,szar,ARRAY,2
szar(1)=0.0127,0.037    ! Size of mesh spacing.
poisson=0.33    ! Assume aluminum plate.
rho=2780
! Define Blast Parameters
*DIM,ZPr, TABLE,113,1,1,Z,Pr

```

```

*TREAD,ZPr,ZPr,txt
*DIM,Zta, TABLE,113,1,1,Z,ta
*TREAD,Zta,Zta,txt
*DIM,ZTs, TABLE,113,1,1,Z,Ts
*TREAD,ZTs,ZTs,txt
*DIM,Zir, TABLE,113,1,1,Z,ir
*TREAD,Zir,Zir,txt
*DIM,Zbr, TABLE,113,1,1,Z,alpha
*TREAD,Zbr,Zbr,txt
! Looping Parameters
*DIM,Wc,ARRAY,2
Wc(1)=0.75,6
*DIM,R0,ARRAY,12,2
R0(1,1)=1,0.5,0.3,3,5,0.4,0.75,2,1.25,1.5,1.75,0.3
R0(1,2)=1,0.5,0.3,3,5,0.4,0.75,2,1.25,1.5,1.75,0.3
ilength=2
*DIM,xnode,ARRAY,5,2
xnode(1,1)=1,10,18,26,34
xnode(1,2)=1,10,18,26,34
numnd=1262
! Main Program Begins
*DO,iWc,1,2
*DO,iR0,1,8
! Steps 1-3: Element Type, Thickness & Material Properties
/FILNAME,AvSS7c,0
/TITLE,Aviation Security Symposium
/CONFIG,NRES,5000
/PREP7      ! Enter the preprocessor.
ET,1,SHELL93

```

```

R,1,height(ilength)
MP,DENS,1,rho
MP,EX,1,youngsm(ilength)
MP,PRXY,1,poisson
TB,BISO,1,1,2,
TBTEMP,0
TBDATA,,ystress(ilength),tanmod,
! Steps 4-5: Create and Mesh Areas
RECTNG,0,length(ilength)/2,0,width(ilength)/2,    ! Axisymmetric quarter plate.
AESIZE,ALL,szar(ilength)    ! Specifies mesh spacing for plate.
AMESH,ALL
NWRITE,coord1,txt,,0    ! Write nodal coordinates to a file.
FINISH    ! Finish preprocessor.
! Calculate Z Values at Every Node
*DIM,NXY,ARRAY,numnd,3
*VREAD,NXY(1,1),coord1,txt,,JIK,3,numnd
(F8.0,G20.13,G20.13)
*DIM,Rnode,ARRAY,numnd
*DIM,Znode,ARRAY,numnd
*DIM,Prnode,ARRAY,numnd
*DIM,tanode,ARRAY,numnd
*DIM,Tsnode,ARRAY,numnd
*DIM,tend,ARRAY,numnd
*DIM,brnode,ARRAY,numnd
tamin=Zta(R0(iR0)/Wc(iWC)**(1/3))/1000
*DO,inode,1,numnd
Rnode(inode)=(R0(iR0)**2+NXY(inode,2)**2+NXY(inode,3)**2)**0.5
Znode(inode)=Rnode(inode)/Wc(iWC)**(1/3)
Prnode(inode)=ZPr(Znode(inode))*1e5*(R0(iR0)/Rnode(inode))**2

```

```

tanode(inode)=(Zta(Znode(inode))/1000-tamin)*Wc(iWC)**(1/3)
Tsnode(inode)=ZTs(Znode(inode))/1000*Wc(iWC)**(1/3)
tend(inode)=tanode(inode)+Tsnode(inode)
brnode(inode)=Zbr(Znode(inode))
*ENDDO

! Steps 6-7: Transient Analysis & Output Controls
/SOLU      ! Enter solution phase.
ANTYPE,4   ! Transient analysis.
TRNOPT,FULL ! Full solution method.
LUMPDM,0   ! No lumped mass approximation.
NLGEOM,1   ! Include large deflection effects.
OUTRES,ALL,ALL,    ! Output data for every timestep.

! Steps 8-9: Apply Boundary Conditions & Initial Loading
DL,2,,ALL,0      ! Constrain outer clamped edges.
DL,3,,ALL,0
DL,1,,SYMM      ! Apply symmetry conditions.
DL,4,,SYMM

! Steps 10-11: Timesteps and Load Step Files
NCNV,2      ! If run fails to converge, program continues.
*DIM,nodepres,ARRAY,numnd
LSnum=1
*DO,tcurr,0.1e-6,1e-6,0.1e-6
*DO,inode,1,numnd
*IF,tcurr,GE,tanode(inode),AND,tcurr,LE,tend(inode),THEN
tsh=tcurr-tanode(inode)
tdur=Tsnode(inode)
nodepres(inode)=Prnode(inode)*(1-tsh/tdur)*exp(-brnode(inode)*tsh/tdur)
*ELSE
nodepres(inode)=0

```

```

*ENDIF
*ENDDO
TIME,tcurr
KBC,0    ! Loading ramped.
SFFUN,PRES,nodepres(1)
SFE,all,1,PRES,1,0
LSWRITE,LSnum,
LSnum=LSnum+1
*ENDDO
*DO,tcurr,1.2e-6,0.1e-3,0.2e-6
*DO,inode,1,numnd
*IF,tcurr,GE,tanode(inode),AND,tcurr,LE,tend(inode),THEN
tsh=tcurr-tanode(inode)
tdur=Tsnode(inode)
nodepres(inode)=Prnode(inode)*(1-tsh/tdur)*exp(-brnode(inode)*tsh/tdur)
*ELSE
nodepres(inode)=0
*ENDIF
*ENDDO
TIME,tcurr
SFFUN,PRES,nodepres(1)
SFE,all,1,PRES,1,0
LSWRITE,LSnum,
LSnum=LSnum+1
*ENDDO
tolDW=1
delt4=0.2e-6
*DOWHILE,tolDW
delt4=delt4*1.02

```

```

tcurr=tcurr+delt4
*DO,inode,1,numnd
*IF,tcurr,GE,tanode(inode),AND,tcurr,LE,tend(inode),THEN
tsh=tcurr-tanode(inode)
tdur=Tsnode(inode)
nodepres(inode)=Prnode(inode)*(1-tsh/tdur)*exp(-brnode(inode)*tsh/tdur)
*ELSE
nodepres(inode)=0
*ENDIF
*ENDDO
TIME,tcurr
SFFUN,PRES,nodepres(1)
SFE,all,1,PRES,1,0
LSWRITE,LSnum,
LSnum=LSnum+1
tolDW=5e-3-tcurr
*ENDDO
LSnum=LSnum-1
LSSOLVE,1,LSnum,1,    ! Solve using loadstep files.
FINISH    ! Finish solution phase.
! Enter Postprocessor
/POST26
FILE,AvSS7c,'rst',','
NSOL,2,1,U,Z
STORE,MERGE    ! Store UZ at plate center.
*GET,SIZE,VARI,,NSETS    ! Get size of displacement array.
*DEL,UZ1
*DIM,UZ1,ARRAY,SIZE    ! Dimension array UZ1.
NSOL,3,xnode(2,ilength),U,Z

```

```

STORE,MERGE
*DEL,UZ2
*DIM,UZ2,ARRAY,SIZE
NSOL,4,xnode(3,ilength),U,Z
STORE,MERGE
*DEL,UZ3
*DIM,UZ3,ARRAY,SIZE
NSOL,5,xnode(4,ilength),U,Z
STORE,MERGE
*DEL,UZ4
*DIM,UZ4,ARRAY,SIZE
NSOL,6,xnode(5,ilength),U,Z
STORE,MERGE
*DEL,UZ5
*DIM,UZ5,ARRAY,SIZE
*DEL,TS
*DIM,TS,ARRAY,SIZE    ! Dimension time array TS.
VGET,TS(1),1    ! Store data in arrays.
VGET,UZ1(1),2
VGET,UZ2(1),3
VGET,UZ3(1),4
VGET,UZ4(1),5
VGET,UZ5(1),6
dispx='AV2'
sp='_'
lt=length(ilength)*100    !
*CFOPEN,%dispx%%sp%%iWc%%iR0%%sp%%lt%X,dat    ! Open data file.
*VWRITE,TS(1),UZ1(1),UZ2(1),UZ3(1),UZ4(1),UZ5(1)
(1x,E13.6,3X,E13.6,1X,E13.6,1X,E13.6,1X,E13.6,1X,E13.6)

```

```
*CFCLOSE  
FINISH    ! Finish postprocessor phase.  
PARSAV,ALL  
/CLEAR,NOSTART  
PARRES,NEW,AvSS7c,parm  
*ENDDO  
*ENDDO
```

## Appendix C

### Details of Box Shaped Deformation Pattern

#### C.1 Definition of Modifying Factors

In Section 6.2.3, it was noted that Yu and Chen [64] use a nomenclature that could potentially be confusing when compared with that previously defined in Chapter 3. Figure C.1 shows how other parameters used throughout this dissertation differ in Yu and Chen's analysis [64]. For consistency with their approach, Appendix C exclusively uses the parameter definitions in Fig. C.1. Note that the origin of the coordinate system shifts from the center to the lower left corner of the plate and that now,  $b \geq a$ . Comparing with the geometry from Fig. 6.3,  $\delta a = B^*$  and  $\xi b = B \tan \phi$ .

Equations 6.21 and 6.22 utilize modifying factors  $f_1$  and  $f_2$ . Using the generalized form of Yu and Chen's moment equations [64], these modifying factors are defined here as

$$\begin{aligned} f_1 &= 1 - 2\delta + 2\xi \frac{b}{a} + 4\eta^2 \left( 1 - 2\delta + \frac{2}{3}\xi \frac{b}{a} \right), \text{ for } \eta < \frac{1}{2}, \\ f_1 &= 4\eta \left( 1 - 2\delta + \xi \frac{b}{a} \right) + \frac{\xi}{3\eta} \frac{b}{a}, \text{ for } \eta \geq \frac{1}{2}; \end{aligned} \quad (\text{C.1})$$

$$\begin{aligned} f_2 &= 1 - 2\xi + 2\delta \frac{a}{b} + 4\eta^2 \left( 1 - 2\xi + \frac{2}{3}\delta \frac{a}{b} \right), \text{ for } \eta < \frac{1}{2}, \\ f_2 &= 4\eta \left( 1 - 2\xi + \delta \frac{a}{b} \right) + \frac{\delta}{3\eta} \frac{a}{b}, \text{ for } \eta \geq \frac{1}{2}, \end{aligned} \quad (\text{C.2})$$

for a simply supported plate, and

$$\begin{aligned} f_1 &= 1 - \delta + \xi \frac{b}{a} + \frac{\eta^2}{2} \left( 3 - 6\delta + 2\xi \frac{b}{a} \right), \text{ for } \eta < 1, \\ f_1 &= \frac{1}{2} + 2\eta \left( 1 - 2\delta + \xi \frac{b}{a} \right), \text{ for } \eta \geq 1; \end{aligned} \quad (\text{C.3})$$

$$\begin{aligned} f_2 &= 1 - \xi + \delta \frac{a}{b} + \frac{\eta^2}{2} \left( 3 - 6\xi + 2\delta \frac{a}{b} \right), \text{ for } \eta < 1, \\ f_2 &= \frac{1}{2} + 2\eta \left( 1 - 2\xi + \delta \frac{a}{b} \right), \text{ for } \eta \geq 1, \end{aligned} \quad (\text{C.4})$$

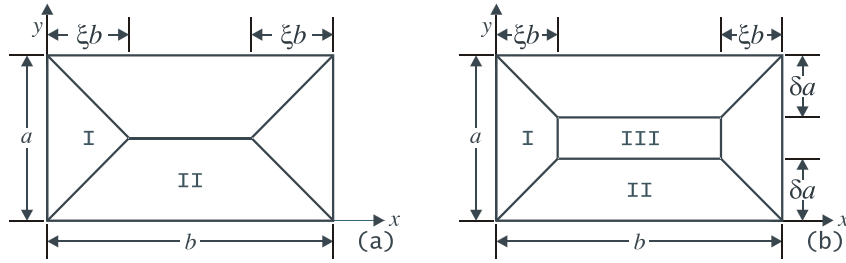


Figure C.1: Plastic deformation patterns with notation of Yu and Chen [64]: (a) roof shape, (b) box shape.

for a clamped plate, where  $\eta \equiv W/h$ , the ratio of maximum central deflection to plate thickness. The reason why  $f_1$  and  $f_2$  are related the way they are is because  $f_2$  accounts for the bending and membrane forces in region II. The geometry of region II is simply a rotated version of that of region I, with all  $\delta$  and  $\xi$ , and  $a$  and  $b$  terms inverted. A detailed derivation of these parameters, which are slightly modified from those provided by Yu and Chen [64], can be found in Ref. [6].

## C.2 Calculation of Initial Values for $\delta$ and $\xi$

The techniques of Yu and Chen [64] can be used to accurately determine initial values of the box shape geometric parameters,  $\delta$  and  $\xi$  (and therefore,  $B^*$ ). Combining Eqs. 6.21, 6.22, 6.26 and 6.27 with the parameter definitions of Fig. C.1,

$$\xi \dot{I}(t)(2 - 3\delta) + (1 - \delta)\xi^2 P(t) = 6M_0\alpha f_1/b^2 \quad (\text{C.5})$$

and

$$\delta \dot{I}(t)(2 - 3\xi) + (1 - \xi)\delta^2 P(t) = 6M_0\alpha f_2/a^2, \quad (\text{C.6})$$

where  $\alpha$  is analogous to the  $\lambda$  used in the first two of these equations. At  $t = 0$ , the impulse is zero, thereby eliminating the first term in both Eqs. C.5 and C.6. Meanwhile, the pressure  $P(t)$  takes on its initial value, which is a known quantity. Plastic moment per unit length  $M_0$  is also known. That leaves two equations with four unknowns, namely  $\delta$ ,  $\xi$ ,  $f_1$  and  $f_2$ . If the initial values of the two modifying factors are known, then one can solve for initial values  $\delta_0$  and  $\xi_0$ .

Assuming  $\phi \approx 45^\circ$  so that  $\delta a \approx \xi b$ , all of the modifying factors, regardless of boundary condition, equal unity when  $\eta = 0$ . Hence,  $f_1$  and  $f_2$  drop out of the aforementioned equations. Separating the variables in the resulting expressions,  $\xi_0$  is given by one of the physically valid roots of

$$\xi_0^5 + \left( \frac{1.5\alpha\sigma_y h^2}{P(0)a^2} - 1 \right) \xi_0^4 - \frac{3\alpha\sigma_y h^2}{P(0)b^2} \xi_0^3 + \frac{3\alpha\sigma_y h^2}{P(0)b^2} \xi_0^2 + \frac{2.25\alpha^2 \sigma_y^2 h^4}{P^2(0)b^4} \xi_0 - \frac{2.25\alpha^2 \sigma_y^2 h^4}{P^2(0)b^4} = 0, \quad (\text{C.7})$$

where  $\sigma_y$  is the dynamic yield stress of the plate material, and  $\alpha = 1$  for simple supports,  $\alpha = 2$  for clamped supports. Meanwhile,  $\delta_0$  is found by inserting the roots of Eq. C.7 into

$$\delta_0 = 1 - \frac{1.5\alpha\sigma_y h^2}{P(0)\xi_0^2 b^2}. \quad (\text{C.8})$$

Mathematically, there are five ordered pairs  $(\xi_0, \delta_0)$  that satisfy Eqs. C.7 and C.8. Geometrically though, it is clear from Fig. C.1b that  $0 \leq \xi_0, \delta_0 \leq 1/2$ . Usually, only one of the ordered pairs meets this additional constraint. Using the energy rate balance method of Sections 6.2.1 and 6.2.2,  $\delta_0 a$  gives the starting value of  $B^*$ , while  $\xi_0 b$  the initial value of  $B \tan \phi$ . Equations C.7 and C.8, which must be solved at the beginning of any analysis assuming a box shaped deformation, are not provided in Ref. [64], but rather are derived by the current author.

## References

- [1] W. E. Baker. *Explosions in Air*. University of Texas Press, Austin, TX, 1973.
- [2] W. E. Baker, P. A. Cox, P. S. Westine, J. J. Kulesz, and R. A. Strehlow. *Explosions Hazards and Evaluation*. Elsevier Science Publishers B.V., Amsterdam, The Netherlands, 1983.
- [3] G. F. Kinney and K. J. Graham. *Explosive Shocks in Air*. Springer-Verlag, New York, NY, second edition, 1985.
- [4] ConWep. *Conventional Weapons Effects Program*. Version 2.1.0.8. U. S. Army, Vicksburg, MS, 2005.
- [5] J. M. Biggs. *Introduction to Structural Dynamics*. McGraw-Hill, Inc., New York, NY, 1964.
- [6] J. R. Florek. *Study of Simplified Models for the Large Deflection of Thin, Rectangular Plates Subjected to Blast Loading*. M.S. Thesis, Rutgers University, New Brunswick, NJ, 2005.
- [7] D. Bogosian, J. Ferritto, and Y. Shi. Measuring uncertainty and conservatism in simplified blast models. In *Proceedings of the 30th Explosives Safety Seminar*, Atlanta, GA, 2002.
- [8] R. L. Veldman, J. Ari-Gur, C. Clum, A. DeYoung, and J. Folkert. Effects of prepressurization on blast response of clamped aluminum plates. *International Journal of Impact Engineering*, 32:1678–1695, 2006.
- [9] M. C. Simmons and G. K. Schleyer. Pulse pressure loading of aircraft structural panels. *Thin-Walled Structures*, 44:496–506, 2006.
- [10] G. S. Landon and G. K. Schleyer. Inelastic deformation and failure of clamped aluminum plates under pulse pressure loading. *International Journal of Impact Engineering*, 28:1107–1127, 2003.
- [11] G. K. Schleyer, S. S. Hsu, M. D. White, and R. S. Birch. Pulse pressure loading of clamped mild steel plates. *International Journal of Impact Engineering*, 28:223–247, 2003.
- [12] G. K. Schleyer, S. S. Hsu, and M. D. White. Scaling of pulse loaded mild steel plates with different edge restraints. *International Journal of Mechanical Sciences*, 46:1267–1287, 2004.
- [13] G. K. Schleyer. Simplified analysis of square plates under explosion loading. In N. Jones and C. A. Brebbia, editors, *Structures Under Shock and Impact VIII*, pages 83–94. WIT Press, Billerica, MA, 2004.

- [14] G. I. Taylor. The propagation and decay of blast waves. In G. K. Batchelor, editor, *The Scientific Papers of Sir Geoffrey Ingram Taylor Volume III: Aerodynamics and the Mechanics of Projectiles and Explosions*, pages 221–235. Cambridge University Press, Cambridge, UK, 1963.
- [15] G. I. Taylor. The formation of a blast wave from a very intense explosion. I. Theoretical discussion. In G. K. Batchelor, editor, *The Scientific Papers of Sir Geoffrey Ingram Taylor Volume III: Aerodynamics and the Mechanics of Projectiles and Explosions*, pages 493–509. Cambridge University Press, Cambridge, UK, 1963.
- [16] J. von Neumann. The point source solution. In G. K. Batchelor, editor, *John von Neumann Collected Works Volume VI: Theory of Games, Astrophysics, Hydrodynamics and Meteorology*, pages 219–237. Pergamon Press Ltd., Oxford, UK, 1963.
- [17] H. L. Brode. Numerical solutions of spherical blast waves. *Journal of Applied Physics*, 26:766–775, 1955.
- [18] H. L. Brode. Blast wave from a spherical charge. *The Physics of Fluids*, 2:217–229, 1959.
- [19] P. D. Smith and J. G. Hetherington. *Blast and Ballistic Loading of Structures*. Butterworth-Heinemann Ltd., Oxford, UK, 1994.
- [20] F. B. A. Beshara. Modelling of blast loading on aboveground structures—I. General phenomenology and external blast. *Computers & Structures*, 51:585–596, 1994.
- [21] F. B. A. Beshara. Modelling of blast loading on aboveground structures—II. Internal blast and ground shock. *Computers & Structures*, 51:597–606, 1994.
- [22] P. S. Bulson. *Explosive Loading of Engineering Structures*. E & FN Spon, London, UK, 1997.
- [23] J. W. Tedesco, W. G. McDougal, and C. A. Ross. *Structural Dynamics: Theory and Applications*. Addison-Wesley Longman, Inc., Menlo Park, CA, 1999.
- [24] J. R. Florek and H. Benaroya. Pulse-pressure loading effects on aviation and general engineering structures—review. *Journal of Sound and Vibration*, 284:421–453, 2005.
- [25] F. Zhu and G. Lu. A review of blast and impact of metallic and sandwich structures. *Electronic Journal of Structural Engineering*, Special Issue: Loading on Structures:92–101, 2007.
- [26] F. G. Friedlander. The diffraction of sound pulses. I. Diffraction by a semi-infinite plane. *Proceedings of the Royal Society of London. Series A, Mathematical and Physical Sciences*, 186(1006):322–344, 1946.
- [27] B. Hopkinson. British Ordnance Board Minutes 13565, 1915.
- [28] C. Cranz. *Lehrbuch der Ballistik*. Springer-Verlag, Berlin, Germany, 1926.
- [29] W. E. Baker, P. S. Westine, and F. T. Dodge. *Similarity Methods in Engineering Dynamics: Theory and Practice of Scale Modeling*. Elsevier Science Publishers B.V., Amsterdam, The Netherlands, second revised edition, 1991.

- [30] C. N. Kingery and G. Bulmash. *Airblast parameters from TNT spherical air burst and hemispherical surface burst*. ARBRL-TR-02555, Aberdeen Proving Ground, MD, 1984.
- [31] TM 5-855-1. *Fundamentals of Protective Design for Conventional Weapons*. U. S. Army, 1986.
- [32] H. J. Goodman. *Compiled free-air blast data on bare spherical pentolite*. BRL Report No. 1092, Aberdeen Proving Ground, MD, 1960.
- [33] C. N. Kingery. *Air blast parameters versus distance for hemispherical TNT surface bursts*. BRL Report No. 1344, Aberdeen Proving Ground, MD, 1966.
- [34] E. D. Esparza. Blast measurements and equivalency for spherical charges at small scaled distances. *International Journal of Impact Engineering*, 4:23–40, 1986.
- [35] M. J. Tang and Q. A. Baker. Non-ideal blast waves. In *International Workshop on Modeling of Non-Ideal Explosives*, Socorro, NM, 1999.
- [36] Q. A. Baker. Private communication. 2007.
- [37] J. A. Gatto. Private communication. 2006.
- [38] DOE/TIC-11268. *A manual for the prediction of blast and fragment loadings on structures*. U. S. Department of Energy, 1992.
- [39] A. F. D'Souza. *Design of Control Systems*. Prentice-Hall, Inc., Englewood Cliffs, NJ, 1988.
- [40] M. A. Akerman, M. D. Kass, and B. T. Clough. Characterization of explosive devices in luggage: initial results of the ART-IIC test series. In *Proceedings of the 64th Shock and Vibration Symposium*, Fort Walton Beach, FL, 1994.
- [41] A. C. Jacinto, R. D. Ambrosini, and R. F. Danesi. Experimental and computational analysis of plates under air blast loading. *International Journal of Impact Engineering*, 25:927–947, 2001.
- [42] K. D. Koper, T. C. Wallace, R. E. Reinke, and J. A. Leverette. Empirical scaling laws for truck bomb explosions based on seismic and acoustic data. *Bulletin of the Seismological Society of America*, 92:527–542, 2002.
- [43] J. Wei and L. R. Dharani. Fracture mechanics of laminated glass subjected to blast loading. *Theoretical and Applied Fracture Mechanics*, 44:157–167, 2005.
- [44] J. Henrych. *The Dynamics of Explosion and Its Use*. Elsevier Scientific Publishing Company, Amsterdam, The Netherlands, 1979.
- [45] E. B. Philip. *Blast Pressure Time-Distance Data for Charges of TNT and GP Bombs*. UK Home Office Report REN 168, 1942.
- [46] M. Held. Blast waves in free air. *Propellants, Explosives, Pyrotechnics*, 8:1–7, 1983.
- [47] J. Collins. *Analytical blast model formulation with computer code*. ARL-TR-2009, Aberdeen Proving Ground, MD, 1999.

- [48] N. Kambouchev, L. Noels, and R. Radovitzky. Nonlinear compressibility effects in fluid-structure interaction and their implications on the air-blast loading of structures. *Journal of Applied Physics*, 100(063519), 2006.
- [49] C. N. Kingery and B. F. Pannill. *Parametric analysis of the regular reflection of air blast*. BRL Report No. 1249, Aberdeen Proving Ground, MD, 1964.
- [50] B. Luccioni, D. Ambrosini, and R. Danesi. Blast load assessment using hydrocodes. *Engineering Structures*, 28:1736–1744, 2006.
- [51] A. D. Gupta, F. H. Gregory, R. L. Bitting, and S. Bhattacharya. Dynamic analysis of an explosively loaded hinged rectangular plate. *Computers & Structures*, 26:339–344, 1987.
- [52] I. Guven, E. Celik, and E. Madenci. Transient response of composite sandwich panels subjected to blast wave pressure. In *Proceedings of the 47th AIAA/ASME/ASCE/AHS/ASC Structures, Structural Dynamics, and Materials Conference*, Newport, RI, 2006.
- [53] L. A. Louca and M. A. Wadee. Simplified non-linear analysis of plates subjected to hydrocarbon explosions. *Journal of Strain Analysis*, 37:301–311, 2002.
- [54] T.-L. Teng, C.-C. Liang, and C.-C. Liao. Transient dynamic large-deflection analysis of panel structure under blast loading. *JSME International Journal, Series A*, 39:591–597, 1996.
- [55] G. N. Nurick and J. B. Martin. Deformation of thin plates subjected to impulsive loading—a review, part I: Theoretical considerations. *International Journal of Impact Engineering*, 8:159–170, 1989.
- [56] J. R. Florek and H. Benaroya. Simplified elastic-plastic modeling of thin, rectangular plates subjected to blast loading. *International Journal of Non-Linear Mechanics*, submitted for publication, 2007.
- [57] S. Timoshenko and S. Woinowsky-Krieger. *Theory of Plates and Shells*. McGraw-Hill, Inc., New York, NY, second edition, 1959.
- [58] J. Lee. Comparison of the two formulations of w-u-v and w-F in nonlinear plate analysis. *ASME Journal of Applied Mechanics*, 69:547–552, 2002.
- [59] J. Lee. Energy-conserving galerkin representation of clamped plates under a moderately large deflection. *Journal of Sound and Vibration*, 275:649–664, 2004.
- [60] H. F. Bauer. Nonlinear response of elastic plates to pulse excitations. *ASME Journal of Applied Mechanics*, 35:47–52, 1968.
- [61] H.-Y. Lai, C.-K. Chen, and Y.-L. Yeh. Double-mode modeling of chaotic and bifurcation dynamics for a simply supported rectangular plate in large deflection. *International Journal of Non-Linear Mechanics*, 37:331–343, 2002.
- [62] N. Jones. A theoretical study of the dynamic plastic behavior of beams and plates with finite-deflections. *International Journal of Solids and Structures*, 7:1007–1029, 1971.

- [63] N. Jones. *Structural Impact*. Cambridge University Press, Cambridge, UK, 1989.
- [64] T. X. Yu and F. L. Chen. The large deflection dynamic plastic response of rectangular plates. *International Journal of Impact Engineering*, 12:603–616, 1992.
- [65] S. K. Singh and V. P. Singh. Mathematical modelling of damage to aircraft skin panels subjected to blast loading. *Defence Science Journal*, 41:305–316, 1991.
- [66] W. Johnson and P. B. Mellor. *Engineering Plasticity*. Ellis Horwood Ltd., Chichester, UK, 1983.
- [67] H. E. Elgamel. Closed-form expressions for the relationships between stress, diaphragm deflection, and resistance change with pressure in silicon piezoresistive pressure sensors. *Sensors and Actuators A*, 50:17–22, 1995.
- [68] C. Massonnet. General theory of elasto-plastic membrane-plates. In J. Heyman and F. A. Leckie, editors, *Engineering Plasticity: Papers for a Conference Held in Cambridge March 1968*, pages 443–471, Cambridge, UK, 1968. Cambridge University Press.
- [69] N. Jones, T. O. Uran, and S. A. Tekin. The dynamic plastic behavior of fully clamped rectangular plates. *International Journal of Solids and Structures*, 6:1499–1512, 1970.
- [70] D. Z. Yankelevsky. Elasto-plastic blast response of rectangular plates. *International Journal of Impact Engineering*, 3:107–119, 1985.
- [71] G. N. Nurick, H. T. Pearce, and J. B. Martin. The deformation of thin plates subjected to impulsive loading. In L. Bevilacqua, R. Feijoo, and R. Valid, editors, *Inelastic Behaviour of Plates and Shells*, pages 597–616, Berlin, Germany, 1986. Springer-Verlag.
- [72] M. D. Olson, G. N. Nurick, and J. R. Fagnan. Deformation and rupture of blast loaded square plates—predictions and experiments. *International Journal of Impact Engineering*, 13:279–291, 1993.
- [73] Y. Jaluria. *Computer Methods for Engineering*. Taylor and Francis, Washington, DC, 1996.
- [74] MATLAB®. Version 7.0.4 Service Pack 2. The Mathworks, Inc., 2005.
- [75] <http://www.matweb.com>.
- [76] ANSYS® Academic Research. Release 9.0A1, 2004.
- [77] <http://www3.sympatico.ca/peterbudgell/modelingissues.html>.
- [78] H. Benaroya and S. M. Han. *Probability Models in Engineering and Science*. CRC Press, Boca Raton, FL, 2005.
- [79] T. Wierzbicki and G. N. Nurick. Large deformation of thin plates under localised impulsive loading. *International Journal of Impact Engineering*, 18:899–918, 1996.
- [80] Y.-W. Lee and T. Wierzbicki. Fracture prediction of thin plates under localized impulsive loading. Part I: dishing. *International Journal of Impact Engineering*, 31:1253–1276, 2005.

- [81] A. Neuberger, S. Peles, and D. Rittel. Scaling the response of circular plates subjected to large and close-range spherical explosions. part I: Air-blast loading. *International Journal of Impact Engineering*, 34:859–873, 2007.
- [82] TM 5-1300/NAVFAC P-397/AFR 88-22. *Structures to resist the effects of accidental explosions*. U. S. Army, Navy and Air Force, 1990.
- [83] PDC-TR 6-01. *Methodology Manual for the Single-Degree-of-Freedom Blast Effects Design Spreadsheets (SBEDS)*. U. S. Army Corps of Engineers, 2006.
- [84] J. M. Coggin. *Response of isotropic and laminated plates to close proximity blast loads*. M.S. Thesis, Virginia Tech, Blacksburg, VA, 2000.
- [85] H. S. Turkmen and Z. Mecitoglu. Nonlinear structural response of laminated composite plates subjected to blast loading. *AIAA Journal*, 37:1639–1647, 1999.
- [86] D. D. Rickman and D. W. Murrell. Development of an improved methodology for predicting airblast pressure relief on a directly loaded wall. *ASME Journal of Pressure Vessel Technology*, 129:195–204, 2007.
- [87] C. J. Gantes and N. G. Pnevmatikos. Elastic-plastic response spectra for exponential blast loading. *International Journal of Impact Engineering*, 30:323–343, 2004.
- [88] L. R. Dharani and J. Wei. Dynamic response of laminated glass under blast loading: effect of negative phase. In N. Jones and C. A. Brebbia, editors, *Structures Under Shock and Impact VIII*, pages 181–190. WIT Press, Southampton, UK, 2004.
- [89] W. K. E. Huntington-Thresher and I. G. Cullis. TNT blast scaling for small charges. In *Proceedings of the 19th International Symposium of Ballistics*, pages 647–654, Interlaken, Switzerland, 2001.
- [90] M. Held. TNT-Equivalent. *Propellants, Explosives, Pyrotechnics*, 8:158–167, 1983.
- [91] M. M. Ismail and S. G. Murray. Study of the blast wave parameters from small scale explosions. *Propellants, Explosives, Pyrotechnics*, 18:11–17, 1993.
- [92] P. W. Cooper and S. R. Kurowski. *Introduction to the Technology of Explosives*. Wiley-VCH, Inc., New York, NY, 1996.
- [93] R. G. Sachs. *The dependence of blast on ambient pressure and temperature*. BRL Report No. 466, Aberdeen Proving Ground, MD, 1944.
- [94] <http://www.boeing.com/commercial/cabinair/index.html>.
- [95] J. M. K. Chock and R. K. Kapania. Review of two methods for calculating explosive air blast. *Shock and Vibration Digest*, 33:91–102, 2001.
- [96] M. S. Hoo Fatt and T. Wierzbicki. Damage of plastic cylinders under localized pressure loading. *International Journal of Mechanical Sciences*, 33:999–1016, 1991.
- [97] M. S. Hoo Fatt and T. Wierzbicki. Damage assessment of cylinders due to impact and explosive loading. *International Journal of Impact Engineering*, 13:215–241, 1993.

- [98] J. R. Florek and H. Benaroya. The response of aircraft structures subjected to an explosive loading of generalized distribution. In *Proceedings of the 4th International Aviation Security Technology Symposium*, Washington, DC, 2006.
- [99] <http://www.mistralgroup.com/images/security/after.jpg>.
- [100] R. B. Schubak, M. D. Olson, and D. L. Anderson. Rigid-plastic modelling of blast-loaded stiffened plates-Part I: One-way stiffened plates. *International Journal of Mechanical Sciences*, 35:289–306, 1993.
- [101] R. B. Schubak, M. D. Olson, and D. L. Anderson. Rigid-plastic modelling of blast-loaded stiffened plates-Part II: Partial end fixity, rate effects and two-way stiffened plates. *International Journal of Mechanical Sciences*, 35:307–324, 1993.
- [102] J. A. Gatto and S. Krznaric. Pressure loading on a luggage container due to an internal explosion. In Y. S. Shin and J. A. Zukas, editors, *Structures Under Extreme Loading Conditions-1996*, pages 29–35. ASME, New York, NY, 1996.
- [103] S. Levy. Square plate with clamped edges under normal pressure producing large deflections. *NASA Technical Note*, 847, 1942.
- [104] D. Wang and A. I. El-Sheikh. Large-deflection mathematical analysis of rectangular plates. *Journal of Engineering Mechanics*, 131:809–821, 2005.
- [105] L. Zhu. Transient deformation modes of square plates subjected to explosive loading. *International Journal of Solids and Structures*, 33:301–314, 1996.
- [106] H. Zhenqiu. Large deflection dynamic plastic response of clamped square plates with stiffeners. *Acta Mechanica Solida Sinica*, 8:24–31, 1995.
- [107] C. M. Morison. Dynamic response of walls and slabs by single-degree-of-freedom analysis—a critical review and revision. *International Journal of Impact Engineering*, 32:1214–1247, 2006.
- [108] V. V. Novozhilov. *The Theory of Thin Shells*. P. Noordhoff, Ltd., Groningen, The Netherlands, 1959.
- [109] C. R. Calladine. *Theory of Shell Structures*. Cambridge University Press, Cambridge, UK, 1983.
- [110] M. Amabili and M. Padoussis. Review of studies on geometrically nonlinear vibrations and dynamics of circular cylindrical shells and panels, with and without fluid-structure interaction. *Applied Mechanics Review*, 56:349–381, 2003.
- [111] M. Dikmen. *Theory of Thin Elastic Shells*. Pitman Books Limited, London, UK, 1982.
- [112] C. R. Calladine. Thin-walled elastic shells analyzed by a Rayleigh method. *International Journal of Mechanical Sciences*, 13:515–530, 1977.

## Vita

### Jason R. Florek

- 1993-97** Piscataway High School, Piscataway, New Jersey
- 1997-2000** B.S. in Mechanical and Aerospace Engineering, Rutgers University, New Brunswick, New Jersey
- 2002-05** M.S. in Mechanical and Aerospace Engineering, Rutgers University, New Brunswick, New Jersey
- 2005-07** Ph.D. in Mechanical and Aerospace Engineering, Rutgers University, New Brunswick, New Jersey
- 2000-02** Junior Engineer/Draftsman, The Knoller Companies, South Plainfield, New Jersey
- 2005-07** Summer Instructor, Rutgers University, New Brunswick, New Jersey
- 2007-** Project Consultant, Baker Engineering and Risk Consultants, Inc., San Antonio, Texas
- 2003** J. R. Florek, "The Effect of Pulse Loading on Elastic-Plastic Structures," presented at the 2003 FAA Mini-Symposium, William J. Hughes Technical Center, Pomona, NJ, May 23, 2003.
- 2003** J. R. Florek, "Pulse-Pressure Loading Effects on Aviation Structures," featured at the Speakers Series, William J. Hughes Technical Center, Pomona, NJ, Nov. 26, 2003.
- 2005** J. R. Florek, "Reduced Order Modeling of Thin, Rectangular Plates Subjected to Blast Loading," presented at the 2005 FAA Mini-Symposium, William J. Hughes Technical Center, Pomona, NJ, April 29, 2005.
- 2005** J. R. Florek and H. Benaroya, "Pulse-Pressure Loading Effects on Aviation and General Engineering Structures—Review," *Journal of Sound and Vibration* **284**:421-453, 2005.
- 2006** J. R. Florek and H. Benaroya, "A Large Deflection Model for Thin, Rectangular Plates Subjected to Blast Loading," presented at the 47th AIAA/ASME/ASCE/AHS/ASC Structures, Structural Dynamics, and Materials Conference, Newport, RI, May 1, 2006.

- 2006** J. R. Florek and H. Benaroya, "The Response of Aircraft Structures Subjected to an Explosive Loading of Generalized Distribution," presented at the 4th International Aviation Security Technology Symposium, Washington, DC, November 30, 2006.
- 2007** J. R. Florek, "Study of Simplified Models of Aircraft Structures Subjected to an Explosive Loading," featured at the Center for Impact Physics Seminar Series, U.S. Army Research Laboratory, Aberdeen Proving Ground, MD, Feb. 8, 2007.
- 2007** J. R. Florek, "Extension of Terrestrial Excavation Mechanics to Lunar Soil," presented at the Rutgers Symposium on Lunar Settlements, Rutgers University, Piscataway, NJ, June 5, 2007.
- 2007** J. R. Florek and H. Benaroya, "Simplified Elastic-Plastic Modeling of Thin, Rectangular Plates Subjected to Blast Loading," *International Journal of Non-Linear Mechanics*, submitted for publication, 2007.